AN EGSNRC MONTE CARLO INVESTIGATION OF BACKSCATTERED ELECTRONS FROM INTERNAL SHIELDING IN CLINICAL ELECTRON BEAMS

BY

ROWEN JURJEN DE VRIES,

14 June, 2014

A THESIS

SUBMITTED TO THE DEPARTMENT OF PHYSICS & ASTRONOMY OF

CANTERBURY UNIVERSITY

IN PARTIAL FULFILLMENT OF THE REQUIREMENTS

FOR THE DEGREE OF

MASTER OF SCIENCE IN MEDICAL PHYSICS

Master of Science in Medical Physics (2014) University of Canterbury

(Physics & Astronomy) Christchurch, Canterbury, New Zealand

TITLE:	An EGSnrc Monte Carlo Investigation of Backscattered Electrons from Internal Shielding in Clinical Electron Beams
AUTHOR:	Rowen Jurjen de Vries B.Sc., (Physics and Mathematics) University of Canterbury Christchurch, New Zealand
SUPERVISOR:	Dr. Steven Marsh
NUMBER OF PAGES:	xv, 153

Abstract

The ability to accurately predict dose from electron backscatter created by internal lead shielding utilized during various superficial electron beam treatments, such as lip carcinoma, is required to avoid the possibility of an overdose. Methods for predicting this dose include the use of empirical equations or physically measuring the electron backscatter factor (EBF) and upstream electron backscatter intensity (EBI). The EBF and upstream EBI are defined as the ratio of dose at, or upstream, from the shielding interface with and without the shielding present respectively. The accuracy of these equations for the local treatment machines was recognized as an area that required verification; in addition the ability of XiO's electron Monte Carlo (eMC) treatment planning algorithm to handle lead interfaces was examined. A Monte Carlo simulation using the EGSnrc package of a Siemens Artiste Linac was developed for 6, 9, 12, and 15 MeV electron energies and was verified against physical measurements to within an accuracy of 2 % and 2 mm. Electron backscatter dose distributions were predicated using the MC model, Gafchromic film, and XiO eMC, which when compared showed that XiO's eMC could not accurately calculate dose at the lead interface. Several MC simulations of lead interfaces at different depths, corresponding to energies of 0.2-14 MeV at the interfaces, were used to validate the accuracy of the equations, with the results concluding that the equation could not accurately predict EBF and EBI values, especially at low energies. From this data, an equation was derived to allow estimation of the EBF and upstream EBI, which agreed to within 1.3 % for the EBF values and can predict the upstream EBI to a clinically acceptable level for all energies.

Contents

List of Figures

List of Tables

Chapter 1

Introduction

1.1 Superficial Lip Carcinoma

Cancer is a leading cause of death in many countries around the world including New Zealand. In 2009 cancer accounted for 28.9 % of all deaths nationwide(1), however the occurrence rate of skin cancer is somewhat unknown in New Zealand. The recording of non-melanoma skin cancers such as squamous cell carcinoma (SCC) and basal cell carcinoma (BCS) has been discontinued since 1958 due to resource constraints(1). The lip is an uncommon and often overlooked site for non-melanoma skin cancers. Up to 90 % of non-melanoma lip cancers are attributed to cumulative ultra-violet (UV) light exposure(2), therefore a significantly higher number of lip carcinomas occur on the lower more exposed lip.

As lip carcinomas manifests at an early stage they are one of the most curable non-melanoma skin cancers of the head and neck. A range of therapy options are available, although radiotherapy and surgery remain the two main therapy options

for lip carcinomas. Currently, radiotherapy is preferred over surgery as it offers similar local control rates while retaining lip functionality(3). In addition, surgery involves a higher risk of recurrence due to incomplete or inadequate excision of the lesion.

Other treatments include brachytherapy, cryotherapy and less commonly laser-therapy. Low dose rate interstitial brachytherapy using 192-Ir wires has been shown to have a similar local success rate as surgery, often without any functional or cosmetic defects. Interstitial brachytherapy is, however, more difficult and costly than surgery(4). Laser treatment of lip carcinoma is also an option but has been a controversial modality in literature. A retrospective investigation of laser-therapy treating stage 1 squamous cell carcinoma of the lip, using yttrium aluminum garnet (Nd:YAG) or carbon dioxide (CO_2) lasers, has shown comparable success to other modalities, though, there are only a limited number of studies presenting successful treatments using laser-therapy(3).

The choice of surgery or radiotherapy for treatment depends on the extent of the carcinoma. Surgery is recommend for smaller lesions as it increases the likelihood of complete excision and thus reducing the risk of recurrence(5). Larger lesions are usually treated with radiotherapy due to a lack of consensus in adequate surgical margins, as well as offering a greater functional outcome of the lip(5). Many radiotherapy treatments of the lip are delivered using superficial or orthovoltage energy photon beams however, electron beam treatments can offer distinct advantages over other radiation beams(6).

Electron beams have been used clinically since the early 1950s and have become a common treatment modality in modern radiotherapy(7; 8). The use of electron beams may be desirable in several clinical situations, such as the lip, due to their

specific depth-dose curves.

1.2 The Aim of Radiation Treatment

The goal of radiotherapy is to irradiate a tumor with an adequately lethal dose while maintaining the dose to surrounding healthy tissue as low as reasonably achievable (ALARA). This ensures that the probability of causing detrimental or irreversible stochastic complications to the surrounding healthy tissue is minimised.

If any amount of ionising radiation is absorbed into biological matter there is a possibility of damage occurring. Damage resulting in mitotic death is largely due to interactions with critical targets within cells, the most vulnerable being deoxyribonucleic acid (DNA).

Radiation damage can occur through either direct or indirect actions, which are graphically shown in Figure 1.1. The direct actions of radiation occur in the form of ionisation or excitation of the atoms within critical targets. Indirect actions involve ionisation or excitation of atoms and molecules, most commonly water, which surrounds critical targets. These interactions lead to the formation of free radicals, such as H_2O^+ and OH^-, which can diffuse throughout the cell and interact with cell components, such as proteins, membranes, enzymes and other critical targets such as DNA. In this case, the damage is due to physical breaks in one or two of the sugar phosphate backbones of DNA or breaks within the base pairs of the DNA molecule(9).

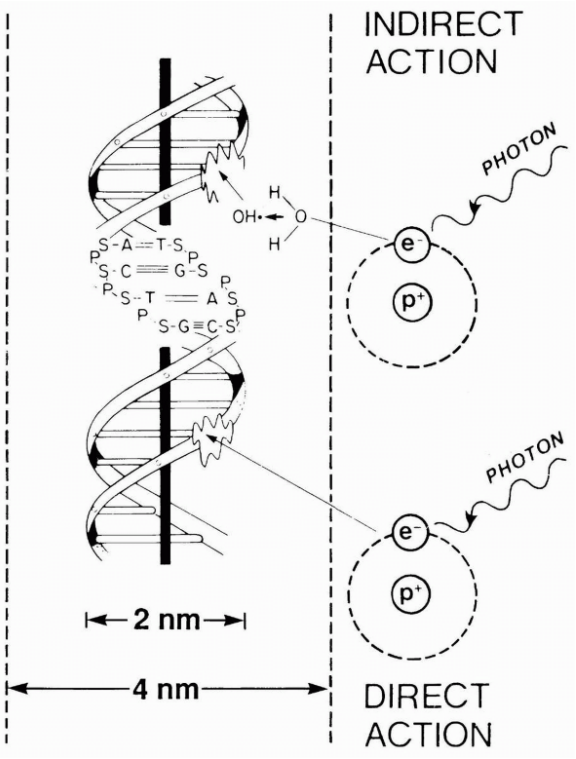

Figure 1.1: Diagram showing direct and indirect interaction of ionising radiation with a DNA molecule. Direct interaction involves directly ionising or exciting the DNA molecule, while indirect interaction involves ionising and exciting surrounding molecules and forming free radicals that interact with the DNA molecule. Reproduced from Hall(9).

Mathematical models are used to estimate the dose required to incite total mitotic death of a tumour, as well as the likelihood of complications to healthy tissue. These models are generated from years of local dose response studies(10). The relationships between dose delivered to a tumour and the probability of a successful eradication of tumour is known as the Tumour Control Probability (TCP). The relationship between dose delivered to healthy tissue and the probability of complications occurring is known as the Normal Tissue Complication Probability (NTCP).

The mathematical basis of the TCP[1] equation is derived by first considering an ideal situation wherein a tumour is considered controlled when all cells have been sterilised(10). This can be modeled using the following Poisson probability distribution.

$$P(N, x) = \exp^{-N} N^x / x!. \tag{1.1}$$

Equation 1.1 calculates the probability (P), of x positive results occurring when the mean number of events is N. The number of surviving cells can be calculated by using the Poisson distribution and the commonly accepted linear-quadratic model of cell killing by radiation(9), shown in Equation 1.2.

$$SF = \exp^{-\alpha D - \beta D^2}, \tag{1.2}$$

where SF is the surviving fraction of a population of cells, D is the dose delivered uniformly over the tumour and α and β are characteristic of cell survival curves. α represents the initial linear response of tissue to dose, and β represents the late quadratic response of tissue to dose.

Replacing the surviving fraction with the average number of initial and final cells, $SF = N_{final}/N_{initial}$, and accounting for n fractions of dose d, and the total dose of D results in;

[1]This description of the TCP equation is only a theoretical approach. The mathematical model is quite simple, but when several other factors are considered, this model describes a fairly complete process of tumour eradication using radiation(10). The factors not considered in this model include such things as non-uniform dose distributions, variation in tumour volumes, clonogenic cell density and hypoxic regions inside tumours, to name a few(9). Even when all the extra factors are considered the absolute value predicted from the model must be used with caution, as there is a lack of data in other areas such as intra-fractional does fluctuation and the appropriateness of combining data with inter-patient heterogeneities(10).

$$N_{final} = N_{initial} \times \exp^{-\alpha D(1+\frac{\beta}{\alpha}\times dn)} . \tag{1.3}$$

The mean number of events, N, in Equation 1.1 corresponds to the mean number of cells, which is $N = N_{final}$. From the initial assumption, a treatment is successful when the final number of cells is zero. This corresponds to a positive result being $x = 0$ in Equation 1.1. Combining these points yields the TCP Equation 1.4.

$$TCP = \exp^{-N_{initial}\exp^{-\alpha D(1+\frac{\beta}{\alpha}\times dn)}} . \tag{1.4}$$

The NTCP can be derived in a similar manner to the TCP. Both can be plotted on the same graph as shown in Figure 1.2. Both the NTCP and TCP curves are characteristically sigmoidal in shape and the difference between these two curves is known as the therapeutic index. A higher therapeutic index results in a higher chance of a complication free treatment of the disease.

The therapeutic index is also plotted in Figure 1.2, with the peak representing the highest chance of a non-complicated cure. The steepness of the therapeutic index curve illustrates that a small deviation in dose can have a considerable influence on treatment outcome. An increase in dose can result in a significant increase in the probability of tumour control as well as future complications, while a decrease in dose can results in a decrease in tumour control probability as well as future complications. Therefore, just like many aspects of radiotherapy, there exists a tradeoff between tumour control and complication probabilities.

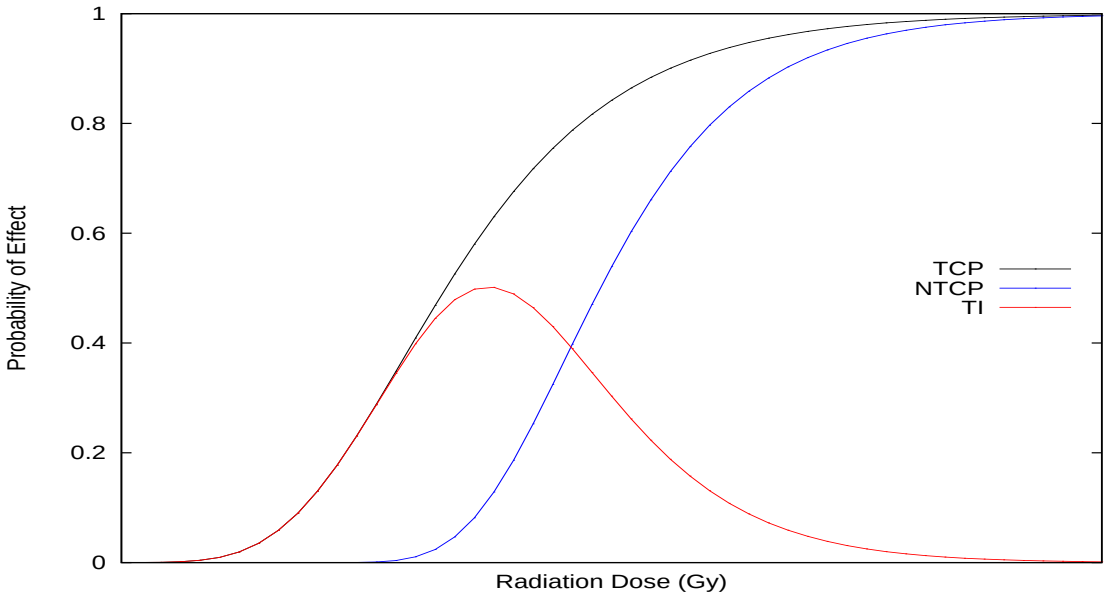

Figure 1.2: Theoretical examples of probability curves for the tumour control probability and the normal tissue complication probability. The difference between the tumour control probability (TCP) and normal tissue complication probability (NTCP) is known as the therapeutic index (TI) and is a measure of the probability of a successful treatment.

Several different techniques can be employed to manipulate the therapeutic ratio such as treatment fractionation or the use of radio-sensitisers(9). All the techniques either alter the dose response of the tumour or tissue, or allow a higher dose to be delivered to the tumour while maintaining or decreasing the dose to healthy tissue. One such technique in this current investigation is the use of internal shielding in lip treatments to protect the deeper healthy tissue, decreasing the chance of normal tissue complication. Although this study draws motivation from lip treatments utilising internal shielding, other superficial sites may also use shielding. Treatment sites such as the eyelids, ears, buccal mucosa, and the nose can also benefit from shielding(6).

1.3 Treatment Planning System Limitations

From the previous discussion it is obvious that an ideal radiotherapy treatment will deliver the bulk of the dose to the lesion while applying the principle of ALARA to the surrounding tissue, thus maximising the therapeutic index for the treatment. Furthermore, the sensitive nature of these probability curves to dose highlights the need for accuracy in dose delivery. Clinical studies have suggested that deviations between planned and delivered dose of 7-10 percent are clinically detectable(11). To estimate the dose delivered to patients, individual treatment plans are created using treatment planning software (TPS). Usually a TPS system will contain several different mathematical models and algorithms for different radiation devices and techniques to estimate the dose within patients.

Arguably, much of the recent progress made in the field of radiation therapy has been in the field of treatment planning. TPS software has rapidly improved through improved analytical and Monte Carlo algorithms, as well as the increasing computer resources now available(10). This has ultimately improved the outcome of individual treatments. Although such sophisticated technology has great clinical benefits, it is important to acknowledge that there is an inherent risk if implemented incorrectly(11). The International Commission on Radiological Protection (ICRP) has compiled a report of 92 different accidental exposures in radiotherapy around the world.

In one recent accident 12 patients have since died, 5 of which have been directly related to treatment planning errors. These major contributing factors related to treatment planning were identified and are as followed:

- Inadequate understanding of treatment planning systems and their limitations
- Inadequate commissioning of treatment planning systems
- Inadequate independent calculations and checks of treatment plans

Electron beams are generally more difficult to model than photons due to the complex nature of electron interactions with tissue. Most commercial treatment planning systems use traditional algorithms, such as the Hogstrom algorithm which in certain circumstances cannot provide the level of accuracy required for radiotherapy treatments(12). This has resulted in many of the commercial treatment planning systems moving to Monte Carlo type algorithms.

Monte Carlo treatment planning algorithms are the most accurate dose calculating algorithm available for electron beams to date(13). True Monte Carlo algorithms allow electron beams to be modeled from first principles however their implementation into commercial treatment planning systems requires the algorithms to be greatly optimised. This ensures that they are able to produce patient treatment plans in a timely manner. This need for greater optimisation combined with the limitations in acquiring patient data, can result in the currently employed commercial Monte Carlo algorithms to fail under certain circumstances regardless(12).

The limitation in current TPS systems in accurately predicting dose distributions from electron beams has meant that some electron treatment techniques are underutilised. More advanced electron treatments may also be avoided completely such as electron arc treatments, skin collimation, and treatments utilising internal shielding. The limitations may also be responsible for the slow introduction of new electron techniques such as modulated electron beam therapy(10).

TPS Algorithms commonly fail due to their inability to correctly handle interfaces and inhomogeneities(12). Several tissue interfaces naturally exist within patients, such as tissue-bone and tissue-air interfaces. When shielding is utilised calculations involving artificially introduced interfaces also exist, such as a tissue-lead interface.

Lead is the most common shielding material used for internal shielding due to its high atomic number and malleability(14). Commercial Monte Carlo algorithms are known to fail when high atomic material is involved. Arguably, since a patient does not contain high atomic material in high concentrations under normal circumstances, this is not considered a limitation for commercial Monte Carlo algorithms. Introduction of high atomic material produces a dose enhancement at the interfaces as well as in the upstream direction. This dose enhancement is caused by electrons backscattering from the interface. The prediction of this up stream dose enhancement is one area where the commercial Monte Carlo algorithms fail.

1.4 Backscattering of Electrons

Theory

The theoretical explanation of the process of electrons backscattering from a material has been studied for the last 100 years. The majority of the explanations come from high energy applications of electrons(15). Interest in the topic originates from physicists interested in the fundamentals of the phenomenon, as well as the development of devices such as beta ray thickness devices and electron interferometers(16). In the last 40 years there has been an ever increasing interest in electron backscatter related to applications in radiation therapy. This is partly

due to the widely available electron Monte Carlo algorithms. These algorithms allow insights into the phenomenon for dosimetry purposes.

As an electron passes through a material it experiences elastic Coulomb scattering whereby interactions with the nuclei of the surrounding atoms causes the electron to change direction. The Coulombic force causing this scatter is expressed by Equation 1.5.

$$\mathbf{F} = k_e \frac{q_1 q_2 \hat{\boldsymbol{r}}_{\mathbf{21}}}{r_{21}^2}. \tag{1.5}$$

where r_{21} is the radius between the two charges q_1 and q_2 and k_e is Coulomb's constant.

Equation 1.5 means the closer the electron is to the scattering center of the nucleus, the larger the force and hence the larger the scattering angle. After each Coulomb scattering event the electron is on average scattered by 5 degrees, however in rare cases the electron can scatter up to 180 degrees(17; 18). Electrons that are scattered in the upstream direction are predominately created by multiple scattering events within the material rather than a single scattering event. These "reflected electrons" are known as backscattered electrons. Many of these Coulomb interactions are elastic scatter events, therefore, the backscattered electrons maintain the same energy as the energy of the incident electron.

Because the Coulomb force applied to the electron is directly related to the charge of the nucleus, which is related to the atomic number of the element, a relationship between the ability of a material to scatter electrons and atomic number is expected. The ability of a material to scatter electrons is quantified by the scattering power of the material. The scattering power of a material varies approximately by the square of the atomic number, Z, and inversely with the kinetic energy, E_k, of the electrons,

as shown in Equation 1.6(8).

$$ScatteringPower \approx \frac{Z^2}{E_k}. \tag{1.6}$$

Equation 1.6 indicates that scattering is much greater for heavier atoms than lighter atoms, and that scattering power decreases as the electrons energy increases. The ability of a material to scatter electrons is therefore also related to the proportion of electrons backscattered from the material. Thus the proportion of backscattered electrons should increase with increasing atomic number and decrease with increasing electron energy.

Electron Backscatter Factor

It is inevitable that backscattered electrons will be absorbed into tissue and this impact on the total dose must be considered. The dose enhancement attributed by the backscattered electrons from shielding tissue interfaces can be quantified by the Electron Backscatter Factor (EBF). The EBF is defined as the ratio of dose at the surface of the interface to the dose at the same point without the interface present and is usually defined on the central axis of the electron beam(19), shown in Equation 1.7. This definition makes the EBF a point quantity, which is physically impossible to measure using volumetric devices such as ion chambers. To measure a point quantity as accurately as possible requires the spatial resolution of the dosimeter to be as small as possible, allowing the effective point of measurement to be as close as possible to the surface of the shielding material. As well as being small, the dosimeter must not perturb the electron fluence in the measurement set up as this would have a physical effect on the EBF value and increases the uncertainty in measured values.

$$EBF = \frac{Dose_{Lead}}{Dose_{withoutLead}}. \tag{1.7}$$

Since the backscattered electrons are largely produced through multiple elastic scattering events they can substantially penetrate into the shielding before being backscattered (Figure 1.3). This results in a relationship between the shielding thickness and the EBF value. The EBF should increase with increasing thickness of shielding material until a saturation level is reached, at this point the EBF value should not change further with increasing shielding thickness.

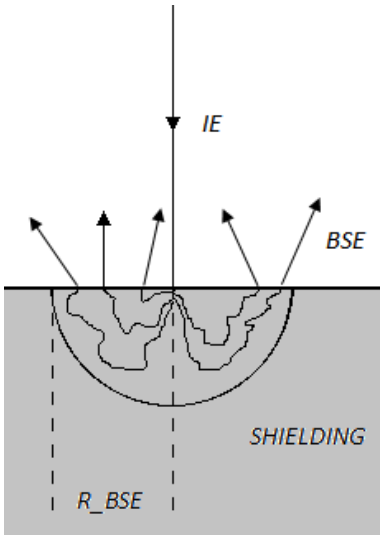

Figure 1.3: Schematic of backscattering region inside a high atomic number shielding material for an electron pencil beam: backscattered electrons, BSE, from initial electrons, IE, in a pencil beam originate from a hemispherical region inside the shielding with radius, R_{BSE}. Reproduced from (17)

The relationship between EBF and shielding thickness can best be exemplified by considering backscattered electrons from a pencil beam, which originate from a hemispherical region inside the shielding material through multiple scattering events, as shown in Figure 1.3(17). As the shielding thickness is increased so is the scattering

region available to the electrons until the shielding's thickness is larger than the radius of the scattering region. The radius of this region in a mono-energetic beam can be approximated as half the average path length of an electron. For lead shielding and the range of electron energies used in radiotherapy, the radius is approximated by $R_{BSE} \approx 0.189 E_m(20)$, where E_m is the energy at the lead surface. This thickness corresponds to the minimum thickness of lead in mm required to obtain maximum backscatter from a mono-energetic electron pencil beam.

Literature Review

Previous studies have confirmed the above theoretical observations about electron backscatter. Firstly, since the scattering power of a material is related to the atomic number, a relationship between atomic number and the EBF should exist. The EBF does indeed increase with increasing atomic number however there is no consensus on the exact type of relationship.

Norman(16) analysed several previous studies to examine the relationship between atomic number and EBF values and concluded that most data obeyed a $log(z+1)$ relationship. This relationship appears to hold over the entire energy range examined in his study.

Klevenhagen(19) comprehensively investigate EBF values from several different materials and depths over a range of electron energies, from 3 to 35 MeV from several different accelerators, using a purpose built ionisation chamber. From this work, a relationship between atomic number and EBF was ascertained and is expressible by $EBF = A - B\exp(-kZ)$ where A, B and k are constants related to the electron beam energy. The proposed $log(z+1)$ relation only held true for a limited energy

range for this work.

Secondly, since the scattering power decreases as the electron's energy increases, the EBF value should decrease with increasing energy. The EBF value for lead has been reported to be between 1.90 to 1.10 in the energy range of 1 to 20 MeV. Results from several different studies are shown in Figure 1.4. The data in Figure 1.4 relates the mean energy of the beam at the lead interface to the EBF value produced. This figure confirms that the EBF value decreases with increasing energy above 3 MeV however there is still debate as to the nature of the relationship below this energy.

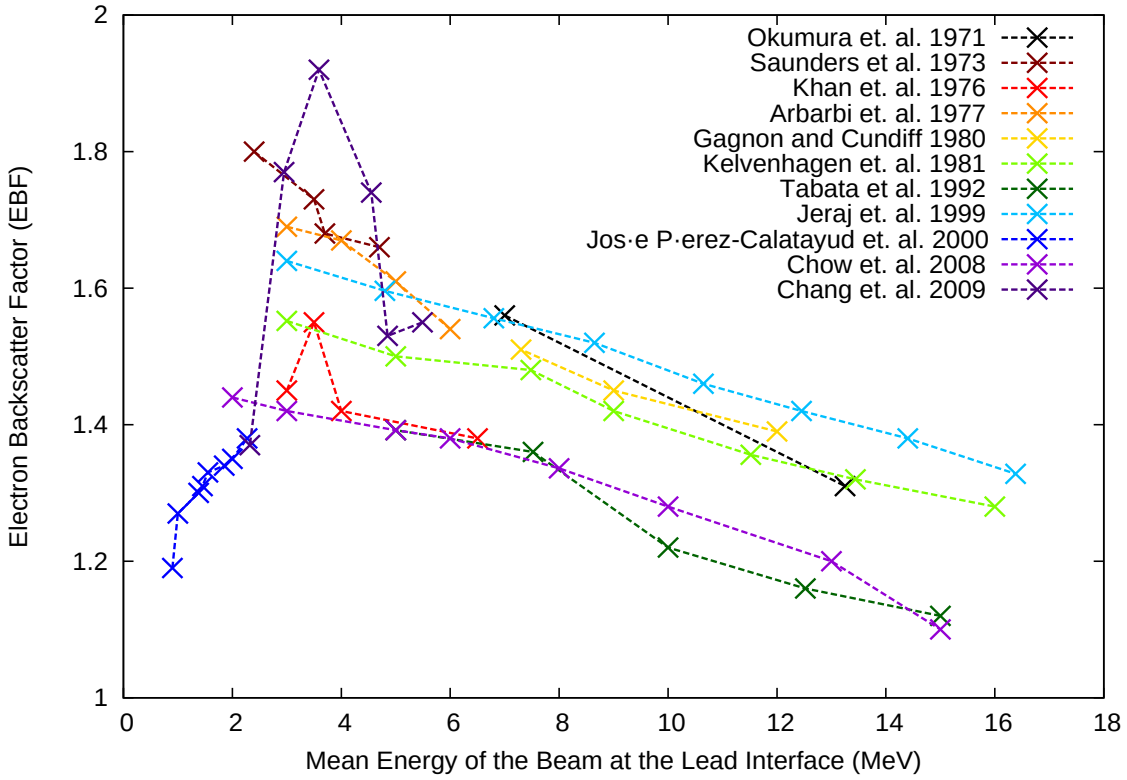

Figure 1.4: Comparison of measured data for the electron backscatter versus the mean electron energy at the lead interface. A clear relationship of decreasing electron backscatter with increasing energy is observable above 3 MeV, however a relationship is not as clear for energies below 3 MeV. Reproduced from several previous studies(14; 19; 21; 22; 23; 24; 25).

The measurements in Figure 1.4 were performed with a range of conventional dosimeters such as film, ion chambers, MOSFETs, and TLDs. Several authors noted difficulty in measuring the EBF value, because of its point quantity definition. Many of the studies indicated errors of between 5 to 20 %(16). This uncertainty in the data could explain the large spread of measured values however several authors attribute this large spread to the different electron spectra produced by different electron beam generating machines. Klevenhagen(19) suggests that the different detectors used to measure the EBF values could also explain the difference in the experimental results.

Klevenhagen(19) proposed that an empirical function relating the EBF value to mean energy at the interface for lead maybe expressed by Equation 1.8.

$$EBF = 1 + 0.735 \exp^{-0.052 E_m}, \tag{1.8}$$

where E_m is the mean energy at the lead interface and can be calculated using Equation 1.9, which estimates the mean energy, E_m at a depth of z mm.

$$E_m = \bar{E}_0 \times \left(1 - \frac{z}{R_p}\right), \tag{1.9}$$

where $\bar{E}_0$ is the mean energy at the surface and R_P is the practical range in mm of the electron beam. The curve fits their experimental data, most of which is plotted in Figure 1.4, to within an accuracy of ± 2.9 % over the entire energy range investigated. This equation is plotted in Figure 1.5. At the time the equation also agreed with the data available in the literature. Since then several new studies at lower energies have been undertaken(14; 23; 24; 25).

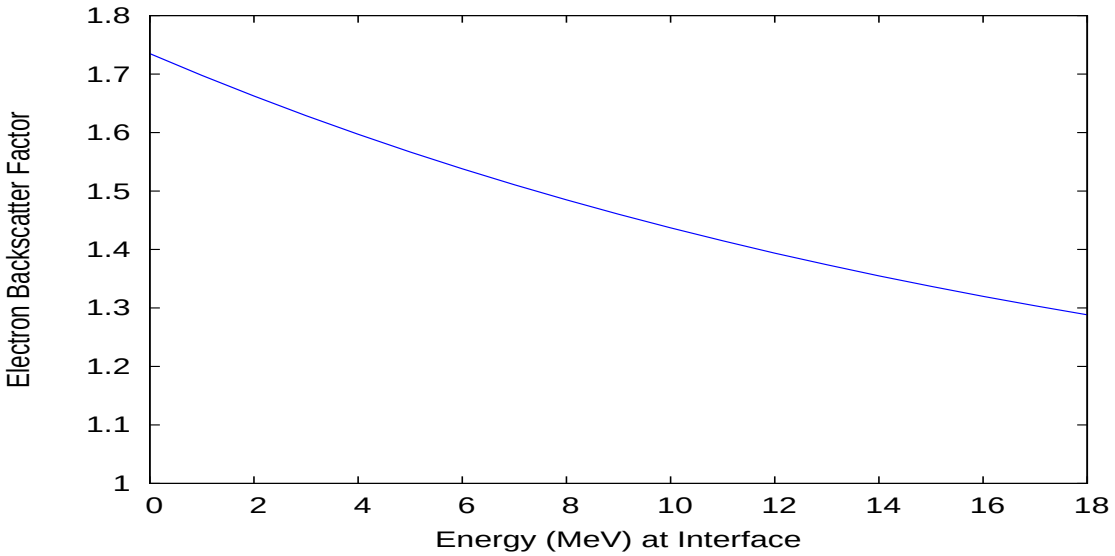

Figure 1.5: Empirical relationship between the electron backscatter factor and electron energy at the lead interface under saturation conditions, obtained from experimental results by Klevenhagen(19).

The empirical equation shown in Figure 1.5 predicts that the EBF will continue to increase, whereas more recent studies have shown that the EBF reaches a maximum in the region of 1-4 MeV at the interface. Joseph(25) proposes that the EBF increases with energy in the region of 0.5 MeV and 1.5 MeV and then remains nearly constant up to 3 MeV, which was the upper limit of his study. Thus the practicability of using Equation 1.8 clinically is questionable.

Finally, a relationship between lead thickness and EBF should exist. Results from Klevenhagen(19) showed a strong dependence of EBF on lead thickness which exhibits a saturation thickness. The saturation thickness depends approximately linearly on lead thickness. The thickness of lead can be estimated using an empirical equation, which is shown in Equation 1.10.

$$t_m = 0.141 \times E_m, \tag{1.10}$$

where t_m is the thickness of lead in mm and E_m is the mean energy at the lead surface. This result is less than the mono-energetic pencil beam approximation of $R_{BSE} \approx 0.189 E_m$.

Although determining the EBF value is clinically important, the dose upstream from the shielding interface must also be ascertained. Studies have shown that backscattered electrons have a range of 1-2 $\mathrm{g/cm^2}$ in polyester. The upstream dose enhancement attributed by the backscattered electrons from shielding tissue interfaces is quantified in this work by the Electron Backscatter Intensity (EBI). The EBI has an identical definition as the EBF except that it can be defined at any depth upstream from the lead interface. The EBI is defined as the ratio of dose at a specified depth involving a lead interface to the dose at the same point without the lead interface present.

Measured values of relative upstream dose enhancement from a lead interface were calculated by Klevenhagen(19) and are shown in Figure 1.6. A proposed relationship between the electron backscatter intensity (EBI)[2]. with upstream depth from the lead interface for electron beam energies between 1 to 25 MeV, from a betatron and linac, for polystyrene was calculated from this work and is expressible by Equation 1.11(19).

$$EBI(t) = EBF \times A \exp^{-kt}, \tag{1.11}$$

[2]The definition of the EBI in Klevenhagen's work is different to the definition in this thesis. The definition in their work is that the EBI is the relative backscatter intensity in relation to the amount of backscatter determined at the lead surface. Hence, to conform their definition to the current definition the equation is multiplied by the EBF value.

where t is the distance in mm in the upstream direction from the lead interface. The value of EBF is calculated from Equation 1.8. k is a constant dependent on the primary electron beam energy and is calculated using Equation 1.12.

$$k = 0.61E_m^{-0.62}. \tag{1.12}$$

The value of the constant A in Equation 1.11 is also dependent on the primary electron beam energy and is estimated from values in Table 1.1.

Beam Energy (MeV)	A	k
1-9	1.0	calculated by Equation 1.12
10-13	0.934	calculated by Equation 1.12
14-25	0.792	0.10

Table 1.1: Table of constants used with Equation 1.11 to determine the upstream intensity of backscattered electrons (EBI) from a lead interface for a given electron energy at the interface. Reproduced from (26).

These empirical equations are useful in estimating dose contributions in the upstream direction.

When lead shielding is used clinically the dose enhancement produced from the lead interface may become the limiting factor in achieving the required dose to the treatment volume. A method to lower the dose enhancement from the shielding can be employed to overcome this. When space permits, a layer of material with a lower atomic number can be placed between the lead shielding and tissue, this is known as an absorber. The absorber creates less scatter than the higher atomic shielding material due to a lower scattering power compared to lead. Furthermore, when the electrons reach the high Z shielding material the average kinetic energy of the electrons will be lower due to the attenuation of the absorbing material. This increases the number of

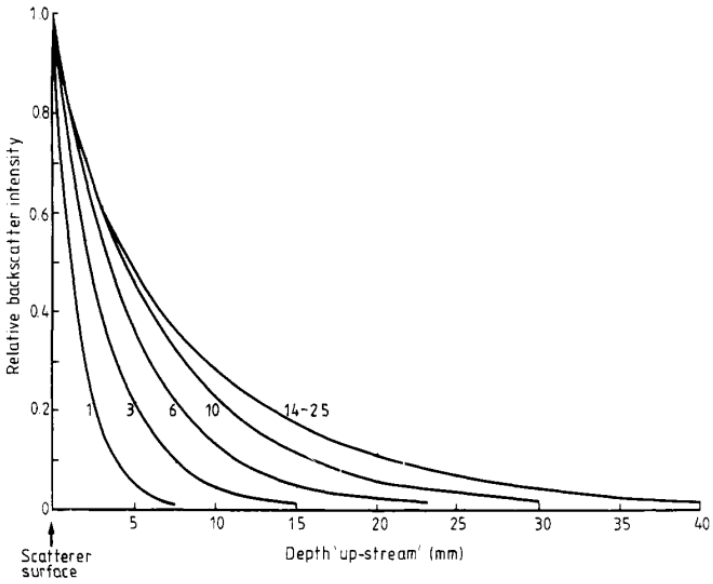

Figure 1.6: Relative Upstream Electron Backscatter Intensity (EBI) in the upstream direction of lead shielding inside polystyrene. Curves for electron backscatter intensity for beams with energies ranging from 1 to 25 MeV are plotted. Graph reproduced from (26).

backscattered electrons, however, as the average energy is lower they penetrate less in the upstream direction as shown in Figure 1.6.

1.5 Internal Shielding Method at Palmerston North Hospital

Currently, lip treatments involving internal shielding are performed at Palmerston North Hospital as follows:

1. The patient has a computer tomography (CT) scan with a wax model of an estimate of the internal shielding to be used in the desired location of the shielding. This is done to avoid metal artifacts in the patient's CT data set. The

metal shielding would create artifacts due to beam hardening, partial volume effects and aliasing. The CT scan is useful to determine the thickness of the lip and the deeper tissue that is to be protected by the shielding.

2. The CT data is then used to plan the treatment. The treatment plan is created using Elekta's CMS XiO (Elekta AB, Stockholm, Sweden) treatment planning system using XiO's electron Monte Carlo algorithm (eMC). This algorithm has been shown by local measurements to have limited ability to calculate dose around high density material. Thus the relative electron density of the wax shielding, which is 1.0, is not modified to the relative electron density of the shielding material.

3. The EBF value at the tissue-lead interface is estimated by a physicist using the method outlined by Klevenhagen(19) and described by Khan(6), based on past experience, or simulated on a phantom. The method described by Khan is as follows:

   (a) The mean energy of the electrons at the tissue-lead interface is estimated using Equation 1.9

   (b) The thickness of shielding required to protect the deeper tissue is then estimated. The minimum lead thickness required for zero transmission of primary electrons is approximated as 0.5 mm per MeV of electrons incident on the lead(6; 27).

   (c) The electron backscatter factor is then either estimated using either Equation 1.8, or taken from Figure 1.5.

If an absorber material is being utilised, the thickness of absorber required to reduce the dose enhancement to a desired level can be estimated from Figure 1.6. The upstream distance to the desired dose level is estimated from this figure. This upstream distance, adjusted by the ratio of the relative density of the absorber material to the unit density of polystyrene, is the thickness of absorber required.

5. The error between XiO's eMC treatment plan and the estimated EBF of the shielding is advised to the Radiation Oncologist. If needed, the monitor units for the treatment are modified to bring the treatment dose closer to the prescribed dose.

Several problems have been recognised with the current system. Firstly, the method relies on Equation 1.8 and 1.11 being able to accurately predict the electron backscatter and upstream electron backscatter intensity for the local treatment machines. Secondly, there is a lack of consistency in determining the shielding design to be used, as it depends on the experience of the physicist who is involved. Usually the lead shielding and aluminum absorber are calculated too thick, however, the thicknesses of shielding and absorber can also be calculated too thin. This results in an overdose before the shielding as well as after the tissue due to backscatter and suboptimal shielding respectively. Finally, even if/when the treatment planning system can accurately calculate dose in the presence of high density material there may still be a need for a second method to check the estimated dose.

1.6 Thesis Outline

This thesis aims to investigate the electron backscatter factor and associated upstream dose enhancement from backscattered electrons created by high atomic number shielding using a Siemens (Siemens Oncology Care, Erlangen, Germany) Artiste Linac. It is hoped that the results will improve the clinical use of internal shielding in electron beams by confirming that the currently used method correctly predicts the EBF value and upstream EBI for the local treatment machines. The ability of XiO's eMC algorithm to model dose enhancement from internal shielding will also be examined. This will determine to what extent the treatment planning system is under-estimating the backscattered dose.

To achieve this a Monte Carlo model of a Siemens Artiste Linac was developed using the EGSnrc package which includes BEAMnrc(28) and DOSXYZnrc Monte Carlo codes from the National Research Council of Canada. This model will be used to make comparisons between XiO's eMC, BEAMnrc model, and physical measurements. Confirmation of the accuracy of the equations currently used clinically will also be performed, with focus on the low energy range. The focus on lower energy electrons is due to the fact that the energy of the electrons at the lead interface are usually in the range of 1 to 3 MeV for 6 or 9 MeV Beams. There is currently no consensus as to the relation of EBF value in this energy region. The equation used in the current method will most likely overestimate the backscatter. Once finished, the model could also be used as a second calculation and check of XiO's eMC or any other treatment planning system for future treatments.

Several of the following chapters included in this thesis will focus on introducing concepts allowing the complete interpretation of the results presented in later

chapters. Chapter 2 introduces electron beams and generators used in radiotherapy, including a description of electron beam generation, focusing on a local machine. This leads into a summary of key components required for a Monte Carlo model. Then key concepts and parameters related to electron beam characterisation are discussed. Chapter 3 will cover the fundamentals of Monte Carlo, including a brief background summary. The simulation package, EGSnrc and treatment planning algorithm, XiO eMC, used in this thesis are also described.

Chapter 4 outlines the methods used to develop and verify the Monte Carlo model. This includes information on initial beam parameters and components included in the model. Verification results for the model are presented, which include comparisons of the parameters discussed in Chapter 2.

Chapter 5 focuses on electron backscatter dose distributions involving lead shielding and compares results from the Monte Carlo simulation to physical measurements and XiO's eMC calculated dose distributions. Chapter 6 investigates the validity of the equations, introduced in section 1.4, currently used to estimate EBF and upstream EBI dose enhancements. Chapter 7 will summarise and draw conclusions from the entire work.

Chapter 2

Electron Beams in Radiotherapy

Electron beams possess a unique depth dose curve which makes them suitable for superficial treatment sites. Commonly available electron beam energies for medical use are in the range of 4 to 25 MeV(10). An electron beam depth-dose curve exhibits a relatively well defined region of acceptable uniform dose from the surface to the depth of dose maximum. Beyond this depth, the dose curve has a steep fall-off which is beneficial in sparing deeper lying normal tissue. The depth of the fall-off can be altered by utilising different energy beams, allowing for the treatment of tumours which extend to a range of different depths. For this reason electron beams are very suitable for use in treating target volumes which are superficially located, allowing underlying tissue beyond that depth to be spared. This is a very unique aspect compared to other commonly used radiation beams, illustrated in Figure 2.1, which compares photon, neutron and particle beam depth dose curves to electron beam depth dose curves.

Electron beams are used for several common superficial treatment sites, to depths

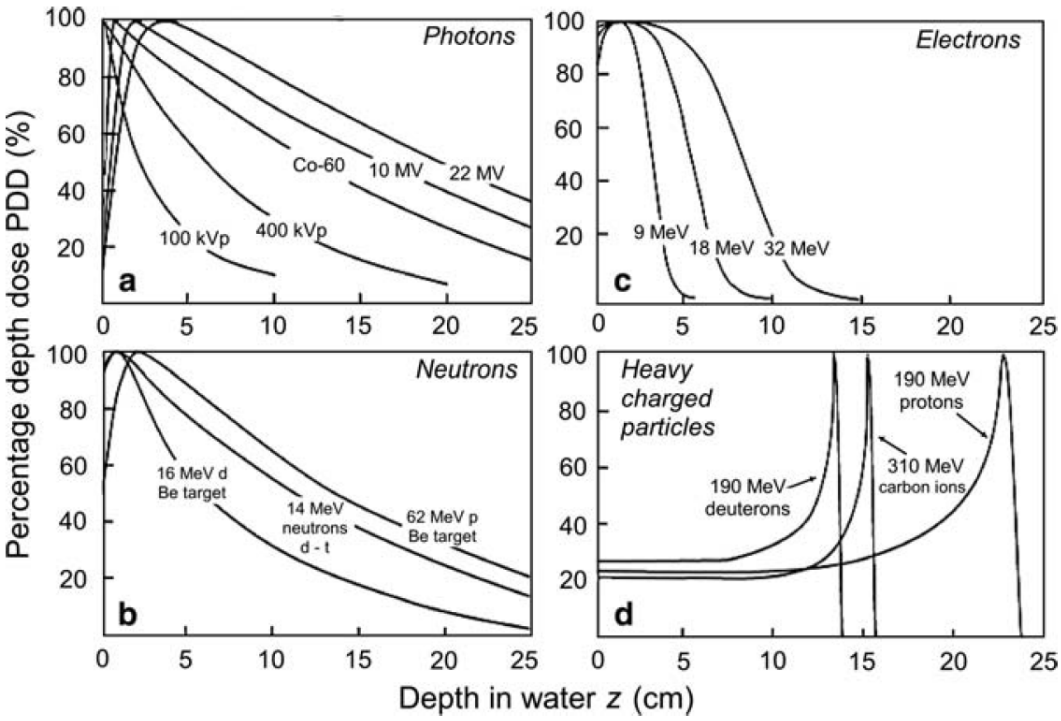

Figure 2.1: Percentage depth dose curves in water for several different ionising radiation beams with various energies used in radiotherapy, illustrating the unique dose fall off of electrons beams. The shallow drop off of dose renders electron beams advantageous in superficial radiation treatments. Reproduced from Podgorsak(29).

of around 5 cm(8). They are most commonly used in treatment sides such as the skin, head and neck, and the lip. They can also be used as a boost treatment to the chest wall in breast cancer treatments(6).

The purpose of this chapter is to familiarise the reader with the general characteristics of clinical electron beams. A short description of electron beam production, focusing on the main beam line components, related to the machine used in this investigation is given. This description emphasises the components which can affect the electron beam characteristics. These components are essential in the development of the MC model. The physical parameters used to describe

electron beams will also be introduced, which will be used for later comparisons and verification between physical measurements and simulation results.

2.1 The Modern Linear Accelerator

Electron beams used in radiotherapy are most commonly generated using linear accelerators (Linacs). Linacs have been developed predominantly to produce high energy photon beams. This is historically due to the tissue sparing ability of high energy photons beams which allows for better treatment of deep tumours. A block diagram of the various components of a modern accelerator is shown in Figure 2.2.

Linacs use radio frequency electromagnetic waves to accelerate electrons though several conductive cavities, located in an accelerating waveguide, to energy's up to tens of MeV. Acceleration of electrons to these energies using standard DC field is unpractical as it would require a potential difference of tens of MV.

There are several different Linac manufactures and each uses slightly different components to perform the critical tasks. The differences between manufactures can affect how a machine operates and performs. Knowledge of the differences is necessary for the development of an accurate MC model. The components discussed here are specific to Siemens Artiste linear accelerators. A complete description of all the components within a modern Linac, and the differences between manufactures, can be found in several radiotherapy textbooks(6; 8; 10) and is not reproduced here.

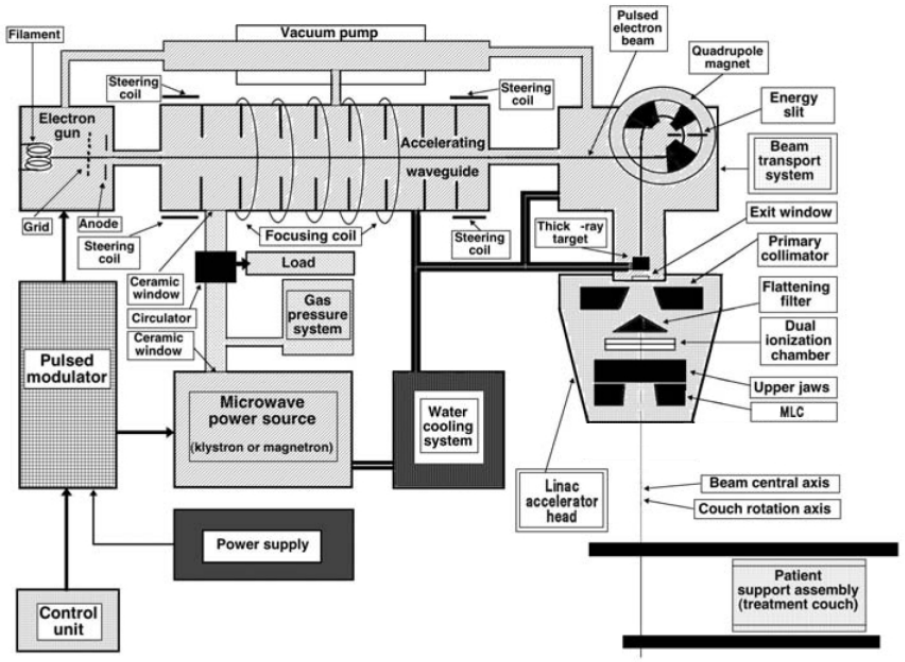

Figure 2.2: Block schematic of a modern Linac showing the various essential components required for operation. Reproduced from Podgorsak(8).

2.2 Siemens Artiste Linear Accelerator

The Siemens Artiste linear accelerator is a duel modality, standing wave linear accelerator which can produce up to six electron energy beams from 5 to 21 MeV and several flattened or un-flattened photon energy beams ranging from 4 to 23 MV, depending on the specification of the purchaser(30). The Siemens Artistes at Palmerston North hospital produces electron beams with energies of 6, 9, 12, and 15 MeV as well as three x-ray beams with energies of 1, 6, and 15 MV. The Artiste's electron beams have a normal operational dose rate of 300 monitor units per minute.

2.2.1 Electron Beam Generation

To create an electron or photon beam, electrons must first be accelerated. The electrons to be accelerated are generated by thermionic emission from a filament, known as the electron gun. They are then injected, in pulses, into the accelerating waveguide. The injection pulses are synchronised to the radio frequency (RF) waves, ensuring they experience a favorable accelerating potential whilst inside the accelerating waveguide. The RF power is produced by a power source consisting of a modulator, klystron, and RF driver. The RF waves accelerate the electrons through the same potential difference multiple times as the electrons traverse several cavities along the accelerating wave guide. The sum of the energy gained by the electrons in all cavities is the total energy of the electrons as they exit the waveguide. The electrons exit the waveguide in the form of a narrow pencil beam. Due to the method of acceleration the pencil beam is expected to have a relatively narrow energy spectrum at this stage.

Bending Magnet System

To produce a high energy beam requires several accelerating cavities, and therefore a lengthy acceleration waveguide. Mounting the waveguide in an orientation directed to the Linac's isocentre is not practical as this would require an increase to the isocentric height of the machine to allow for gantry rotation. A bending system is required to redirect the electrons towards the isocentre. This bending system consists of a pair of electro-magnets. The bending magnets can be thought of as a simple dipole however in reality the system is more complex. The region between this dipole has a uniform magnetic field strength, $\mathbf{B}$, ignoring any fringe fields. Using the Lorentz force law on

a point charge due to an electromagnetic field the force on the electron is,

$$\mathbf{F} = q(\mathbf{E} + \mathbf{v} \times \mathbf{B}) = \frac{d\mathbf{p}}{dt}, \tag{2.1}$$

where q is the charge on the electron, $\mathbf{E}$ and $\mathbf{B}$ are the electric and magnetic field strength respectively, $\mathbf{v}$ is the velocity of the electron, and $\mathbf{p}$ is the momentum.

As there is no electric field in the same orientation as the electron's velocity, $\mathbf{E} = 0$. Substituting $\mathbf{E} = 0$ and the fact that the momentum, $\mathbf{p} = \gamma m\mathbf{v}$, into Equation 2.1 yields Equation 2.2.

$$q(\mathbf{v} \times \mathbf{B}) = \frac{d(\gamma m\mathbf{v})}{dt} = \gamma m\frac{d\mathbf{v}}{dt}. \tag{2.2}$$

The centripetal acceleration for an electron traveling in a circular trajectory in a magnetic field is given by $\mathbf{a} = -\mathbf{v}^2/R$, substituting this into 2.2 yields Equation 2.3.

$$q(\mathbf{v} \times \mathbf{B}) = \gamma m(-\frac{\mathbf{v}^2}{R}). \tag{2.3}$$

The radius of curvature is thus given by;

$$R = \frac{\gamma m\mathbf{v}}{q\mathbf{B}}. \tag{2.4}$$

From Equation 2.4 it can be seen that the radius of curvature of the electron in the bending magnet is dependent on the electron energy and magnetic field strength. As the radius of the bending magnet is fixed, the only electrons to exit the bending magnet system will fall within a defined energy window depending on the magnetic field strength. Electron largely outside this energy window will collide with the wall

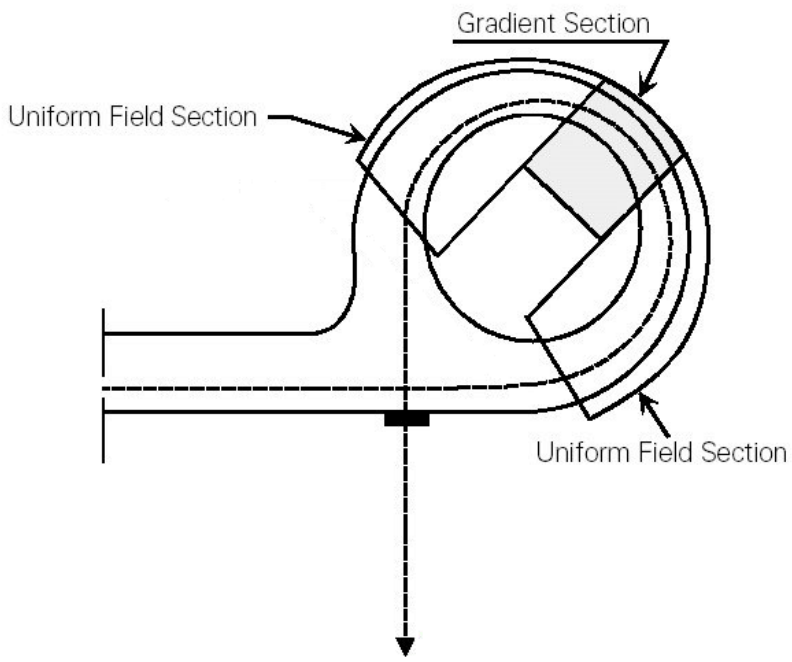

Figure 2.3: Schematic of an achromatic bending magnet system used in the Siemens Artiste linear accelerator. An achromatic bending system uses a combination of uniform and gradient magnetic fields to select the electron beam energy and redirect the beam towards the isocenter. Reproduced from (31)

of the bending system and be dissipated as heat. This energy window can be altered by adjusting the bending magnet current, allowing the bending magnet system to be used as a energy selector.

The Siemens Artiste has a more complex bending magnet system than a simple dipole system however the basic principle is the same. The Artiste uses a 270° achromatic bending magnet system. This bending magnet has both a uniform magnetic field section and a gradient magnetic field section, as shown in Figure 2.3.

An achromatic bending magnet system allows for a larger range of electron energies around the expected energy to reach the exit window, as shown in Figure 2.4. The

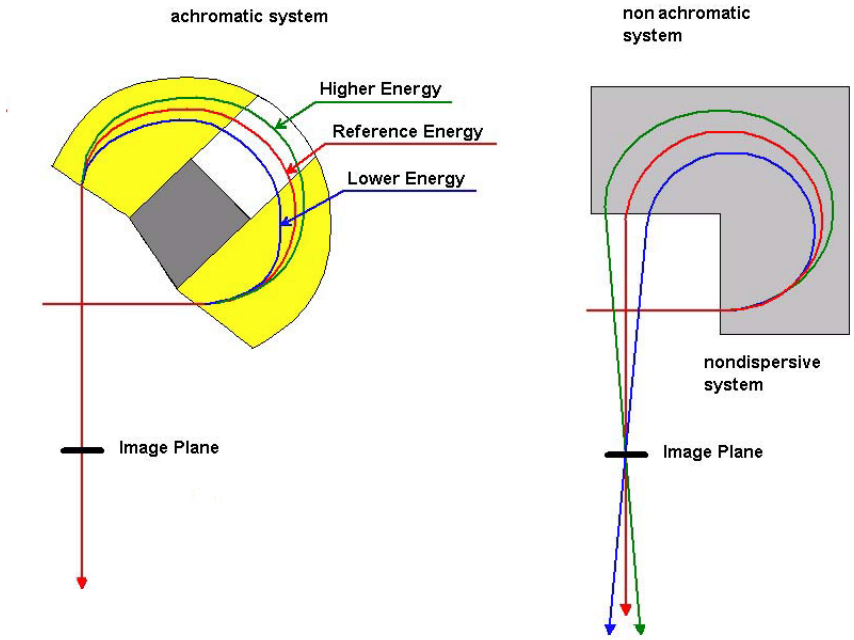

Figure 2.4: Schematic of an achromatic bending magnet system and a non achromatic bending magnet system. The schematic shows the difference between the two in regards to the final direction of electrons which entered the system with different energies. Reproduced from (31)

achromatic bending system also ensures that the electrons that exit the bending system are directed towards the isocenter. Thus, the bending magnet in a Siemens Artiste has 3 functions:

- to act as an energy selector
- to focus the beam
- to direct the beam towards the isocenter

The bending magnet system will not explicitly be modeled; however, it is important to understand the bending magnet system when considering the type of initial beam

to use in an MC model. Since the Artiste machine uses an achromatic bending magnet system it may be expected that the pencil beam exiting the waveguide will possess a larger degree of energy spread than reported for other Linacs using different bending magnet systems.

2.2.2 Treatment Head

Once the electrons have been focused and directed towards the isocenter they emerge from the vacuum envelope by penetrating the vacuum exit window. The exit window consists of two thin metal foils, with a water pocket in-between for cooling. The exit window maintains the vacuum of the waveguide and electron transport system.

The components further down the beam line are collectively known as the Linac head. The Components within the Linac head are responsible for many of the characteristics of the final treatment beam. Beam aspects such as radiation type, field size, symmetry, and flatness are all affected by different components within the treatment head.

Double Scattering Foil System

To obtain a useful electron beam for treatment the electron pencil beam must first be scattered to form a large and homogeneous beam. In a Siemens Artiste this is performed with a double scattering foil system. A primary scattering foil is located on a slide close to the exit window along side the photon targets. This primary foil is changed in both composition and thickness depending on the energy of the electron beam being produced. The second scattering foil is in the form of a tri-leveled pyramid and is the same for all electron energies. The second scattering foil is physically

located on the target side of the electron monitor chamber. The monitor chamber is made up of several thin films of material, some of which are metallic and act as collecting electrodes.

The thickness and dimension of the scattering foil, and to a lesser extent the metallic layers in the monitor chamber and exit window, will have a pronounced effect on the beam spectrum and profile further down the beam line. Specific details of these components are needed to obtain an accurate MC model of the Linac.

Collimating Jaws

To define photon fields the Siemens Artiste machine employs a solid upper Y-jaw, and a 160 Multi-Leaf Collimator (MLC) lower X-jaw. When in electron mode these jaws are retracted well outside the electron beam, presumably, as they may act as significant scattering surfaces, degrading the physical penumbra of the field size and beam quality. They could also potentially increase the photon component of the beam. As the jaws and MLC are retracted well outside the electron beam edge while in electron mode a detailed description is not necessary however they will still be included in the Model.

Electron Beam Collimation

Electrons are highly susceptible to the Coulomb fields that surround them due to their charge and small mass. This causes electrons to scatter quite substantially when compared to photons. To achieve good field definition at the isocentre electron beams require collimation beyond the collimating jaws. This is performed using an electron applicator or cone which defines the treatment field size at the isocenter.

A range of applicator sizes are usually available, allowing flexibility in optimising individual treatment.

The Siemens Artiste applicators consist of several different scrapers made of a range of material. A higher atomic number material is used on the upper scrapers and a lower number atomic material is used on the lower scrapers. This is presumably done to increase the ability of the higher scrapers to attenuate, and to decrease the bremsstrahlung produced in the lower scrapers. The applicator sizes range from a circular 5 cm diameter applicator to square applicators of sizes 10, 15, 20, and 25 cm.

To accommodate more complex field shapes a cutout can be inserted into the end of the electron applicator. Cutouts can be manufactured to practically any field shape desired. They are usually made specifically for individual patients from a low melting point alloy mixture of lead, bismuth, tin and cadmium. This mixture is known as ceroblend or Wood's metal. The design and materials of the applicators and cutouts are important and can affects the dose distribution. The shape will affect both the field size and the penumbra of the field edges. The materials that they are made of can also lead to the formation of a bremsstrahlung edge, especially in higher energy electrons beams.

Several other components are present within the electron beam line, such as the shielding plate and reticule. These components have been included in the model, but a description is deemed unnecessary.

2.3 Physical Characteristics of Electron Beams

It is essential that the dose predicted from the MC Linac simulation agrees with the physical measurements. In assessing the accuracy of the model to physical measurements, a number of parameters relating to electron beams can be used. A brief description of these parameters is therefore included in the next section for reference. A more rigorous explanation of these parameters can be found in the literature and in various textbooks(6; 7; 8; 10; 27)

Percentage Depth Dose

One of the most fundamental means to assess the penetrating power of an electron beam is to use a percentage depth dose (PDD) curve. A PDD curve is a central axis dose distribution, inside a patient or phantom, which is normalised to the depth of dose or dose rate maximum, $d_{max}(10)$. The PDD is defined by Equation 2.6.

$$PDD(z, A, f, E_0) = 100 \times d_z/d_{max}p = 100 \times \dot{d}_z/\dot{d}_{max}, \tag{2.5}$$

where d_z and $\dot{d}_z$ are the dose and dose rate respectively at a point on the central axis at a depth of z. d_{max} and $\dot{d}_{max}$ are the dose and dose rate respectively at a point on the central axis at a depth of dose maximum.

PDD curves for different electron beams with the same stated nominal energy, E_0, may be different. This is due to the differences in the spectrum of each beam. The difference in electron spectrum may be due to differences in the transport system, scattering foils, and applicator design, as well as machine tuning parameters.

Asides from the irregularities between treatment machines, the PDD curve

depends on several other parameters such as source to surface distance (SSD), field size A, angle of incidence, and surface irregularities. The relationship between these parameters is of no concern in the current investigation. More information on how these parameters affect the PDD curves can be found in several radiation physics textbooks(8; 10).

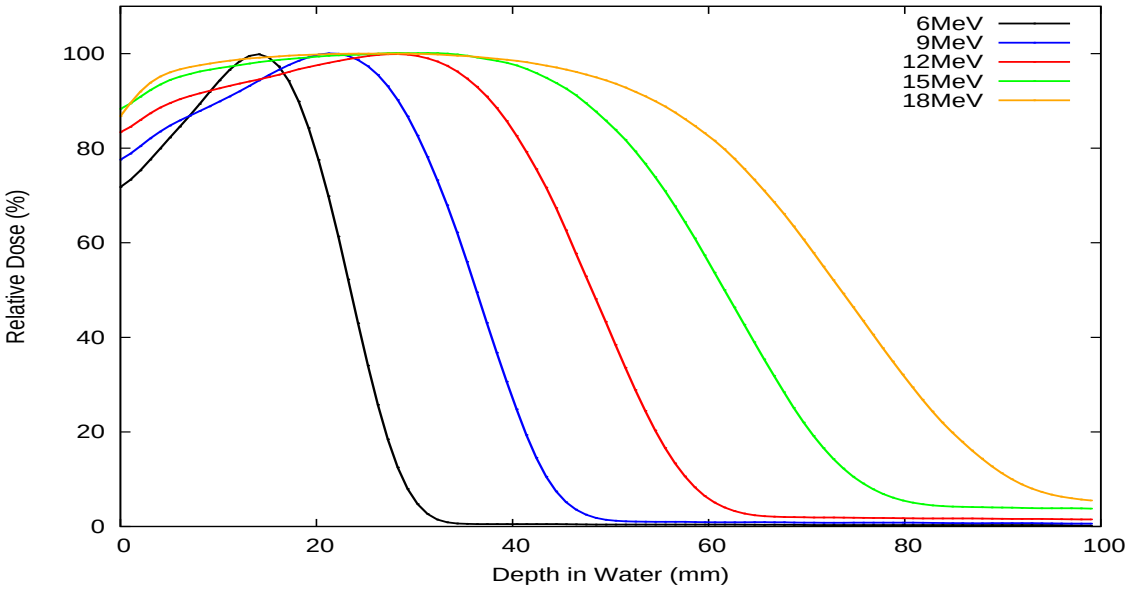

Figure 2.5: Examples of percentage depth dose curves of electron beams with nominal energies of 6, 9, 12, 15, and 18 MeV.

Figure 2.5 shows the general shape of electron PDD curves for several different nominal energy electron beams. These curves illustrate the main aspects common to electron beams. They build up dose to d_{max} quickly and then exhibit a region of relatively uniform dose with increasing depth. Figure 2.5 shows that the region of uniform dose is more pronounced in medium to higher energy beams than for lower energy beams. After the flat region, the dose drops off sharply to almost zero, with a steeper fall off for lower energy electron beams. The dose remaining after this fall off

is known as the tail and is attributed to bremsstrahlung x-rays that have been created within the treatment machine, collimation devices, or the surrounding medium. The bremsstrahlung tail dose increases with increasing energies. This is due to the increase in bremsstrahlung production with the increase in electron energy.

Electron Beam Parameters

Several parameters are defined for a clinical electron beam such as; the practical range R_p, the depth of dose maximum R_{100}, the therapeutic depth R_{85}, the half depth R_{50}, the surface dose D_s, and the bremsstrahlung tail dose D_x. These are shown on the PDD curve in Figure 2.6.

The practical range, R_p, is defined as the depth at which the tangent of the inflection point of an electron beam's PDD curve intersects the extrapolated line of the bremsstrahlung tail dose(10). R_q is defined as the depth at which this tangent intersects the dose maximum. G is the gradient of the tangent line, and R_{100} or D_{max} is the depth of dose maximum for the PDD curve being considered. The half depth, R_{50}, is the depth at which the dose drops to 50 % of d_{max}. D_x is the dose level of the bremsstrahlung tail. D_s is the dose at the surface, which is usually between 70-90 % of D_m.

The therapeutic range is commonly defined at either the depth at which the dose drops to the 90, 85, or 80 % level beyond D_{max}, depending on the local procedures(8). The therapeutic range most often coincides with the most distal treatment margin which usually results in adequate coverage of the treatment volume. A rule of thumb to estimate the depth of the therapeutic range, R_{90} and R_{80} in cm of water, can be estimated by Equation 2.6(6).

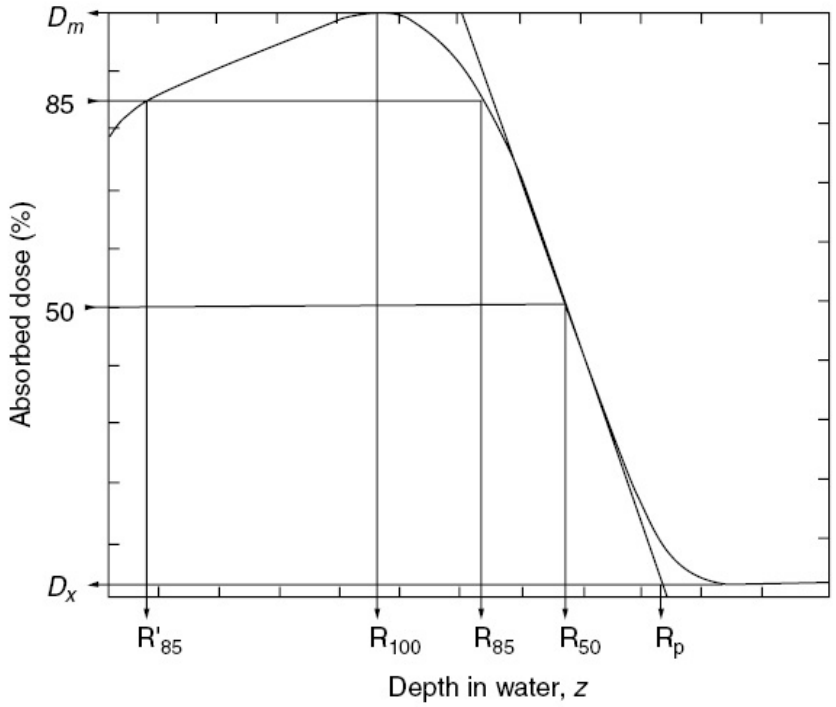

Figure 2.6: Typical electron PDD curve illustrating several electron beam percentage depth dose parameters used to characterise different energy electron beams; such as the practical range R_p, the depth of dose maximum R_{100}, the therapeutic depth R_{85}, the half depth R_{50}, and the tail dose D_x. Reproduced from (8)

$$R_{90} = \frac{E}{4}, \qquad R_{80} = \frac{E}{3}, \tag{2.6}$$

where E is the nominal energy of the electron beam in MeV.

Electron beams produced on different machines with the same stated nominal energy can produce different PDD curves. To allow the comparison of different electron beams, a measure of beams penetration power is used, this is known as the quality of an electron beam. The parameter used to describe the quality of an

electron beam under the IAEA TRS-398 protocol is the R_{50} depth(32). Historically, the parameter used has been the mean energy at the surface but as this is usually calculated using the depth of R_{50}, they are essentially the same.

Electron Beam Energy Specification

Several different parameters are used to describe the energy of an electron beam. One of these parameters is the most probable energy, $E_{p,0}$, on the phantom surface. This parameter is difficult to measure in the clinic. Fortunately, an empirical relationship has been developed and is shown in Equation 2.7(8).

$$E_{p,0} = 0.22 + 1.09 \times R_p + 0.0025 \times R_p^2, \tag{2.7}$$

where $E_{p,0}$ is in MeV, and R_p is in cm.

Another parameter used to specify the energy of an electron beam is the mean energy at the surface. An empirical relationship relates the half-value depth, R_{50}, and the mean energy at the medium's surface by Equation 2.8.

$$\bar{E}_0 = C \times R_{50}, \tag{2.8}$$

where $C = 2.33\,\mathrm{MeV}^{-1}$ and R_{50} is in cm(8). Although this relationship was derived from electron beam measurements conducted in the seventies it is still useful for today's electron beams, however, Equation 2.8 has been shown to overestimate the electron beam's energy(33). Strictly speaking, the formula is only valid for broad beam geometry(10). The criterion for broad beam geometry is that the depth dose is independent of the field size(10). This condition is considered meet when the field

size is larger than the practical range of the electrons. This will ensure that lateral electron equilibrium is upheld.

As introduced in section 1.4, the mean energy of an electron beam at a certain depth can be estimated with Equation 1.9 by using the practical range and the most probable energy at the surface. This energy is often used to compare certain values across different machines.

It should be noted that the above electron energy parameters and empirical formulas for electron beams are only approximations and are not intended to be an accurate statement of electron beams energy. Instead they are useful for the selection of dosimetric quantity as well as correction factors and comparing different machines. More accurate methods of determining some of these parameters have not significantly improved the overall accuracy in electron beam dosimetry. The improvement in accuracy of electron beam dosimetry has mainly come from greater accuracy in data regarding electron stopping power(10).

Beam Profiles

Beam profiles are often measured in conjunction with PDDs. Beam profiles are measurements made over the entire electron field in a plane perpendicular to the collimator axis of rotation at different depths in water, usually including the depth of d_{max}. Beam profiles are useful in determining different beam parameters such as off axis ratios, beam symmetry, flatness, and width of beam penumbra.

Off axis ratios are the ratio of the dose on the central axis to the dose at a point not on the central axis. Beam symmetry and flatness are specified over a selected central region of an electron beam, usually 80 % of the central region of a beam. The

beam penumbra is a measure of the steepness of the field and is the distance between the 80 % dose level and the 20 % dose level.

Beam profiles are usually measured with a scanning dosimeter at several different depths using an appropriate dosimeter to preserve the accuracy in the penumbral edges. They are normalised to the dose maximum on the central axis PDD curve for the corresponding characteristics such as field size and SSD, ect.

Isodose Curves

Isodose curves are lines that pass through points which have equal dose. They can either be displayed in absolute dose or as a percentage. Isodose distributions allow for a 2D visualisation of electron beams, whereas electron PDDs and profiles are essentially only 1D. Isodose plots will show the features of a typical electron beam, with the relatively uniform region of the field evident, as well as the steep fall off of dose. The main characteristics that are shown well with an isodose distribution, and is not shown in a PDD curve, is the increase of penumbra width as the depth increases. The lower value isodose lines bulge outward as the depth increases. This is an effect of the mean energy of the electrons. Lower energy electrons are scattered more easily than higher energy electrons. As the depth increases, the mean energy of the electrons decreases, hence the isodose lines and thus electron beams bulge outward at depth.

2.4 Summary

The previous section has described the general characteristics of clinical electron beams. Electron beams have a high surface dose and then a region of nearly uniform dose followed by a steep dose fall-off. This is a unique aspect which makes electron beams suitable for use in treating target volumes which are at depths close to the surface, as this allows underlying tissue beyond the treatment depth to be spared.

A description of a Modern Linac was included, and the main components in a Siemens Artiste electron beam line have been described. The main components such as: the bending magnet system, scattering foil, and electron applicators were included. These components are necessary and must be included in the MC simulation to achieve an accurate Linac model. Electron PDDs parameters, electron beam energy specifiers, beam profiles, and isodose distributions were introduced. These will all be used to assess the accuracy of the MC simulation and have been acquired directly from the physical machine.

Chapter 3

The Monte Carlo Method

Some processes in the physical world are inherently unpredictable. For example, the physical outcome of an electron scattered by an atom cannot be predicted with complete certainty. The Monte Carlo method combines the results of many such unpredictable events to compute a composite solution using random numbers to a desired statistical accuracy. The statistical accuracy of the composite solution depends on the number of random elementary events simulated. Each elementary event is either an event that cannot be analysed into a simpler event, or an event that is chosen not to be analysed into simpler events.

The main difference between a Monte Carlo type dose calculation and a deterministic dose calculation is in the computation sequence. A deterministic calculation computes on a point by point basis, therefore handling geometry serially and physical interactions in parallel. A deterministic dose calculation is complete once dose values have been calculated to all voxels included in the calculation volume. In contrast a Monte Carlo calculation computes on a particle by particle basis, therefore

handling geometry in parallel and physical interactions serially. A Monte Carlo algorithm simulates particle by particle and assigns dose to voxels along the path of simulated particles. After a finite number of particles have been simulated the accumulated dose distribution resembles the physical dose distribution, but it is still only an approximation. A Monte Carlo calculation's statistical accuracy can always be improved by simulating more particles. This means that a Monte Carlo calculation is always finished but never complete.

In radiation therapy planning, the Monte Carlo method is used to build up a composite dose distribution through the summation of dose deposited by individual interactions of photons and electrons with the surrounding medium. This chapter introduces the types of interactions that electrons and photons undergo as they traverse their surroundings, resulting in the deposition of dose. A more in depth discussion of the Monte Carlo method and a brief history behind the method is also included, as well as an introduction to the Monte Carlo software package used in the current investigation.

3.1 Background and History of Monte Carlo

The history of the Monte Carlo method has been comprehensively covered in many textbooks and articles, nevertheless, a short history of the method is included for completeness(10; 12; 34).

The name Monte Carlo was adopted from the famous Monte Carlo Casino in Monte Carlo, Monaco, in 1947. The earliest documented application of the method far out-dates the name. In 1777, Comte de Buffon proposed a technique to evaluate

π by using a simple Monte Carlo technique involving simulating a needle falling onto a ruled sheet of paper, noting that the probability of the needle intersecting a line is proportional to π(35) .

The modern Monte Carlo technique, where digital computers are employed, was ushered in during the initial development of thermo-nuclear weapons in the late 1940s. More specifically, the method was used to study neutron scattering and absorption. John von Neumann and Stainslaw Ulam both worked on the method at the Los Alamos National Laboratory and made substantial advancements. Von Neumann understood the importance of the method and quickly programmed a computer to carry out Monte Carlo calculations. From this point on there was an ever increasing surge of papers describing the uses of the method in theoretical physics, as well as several other fields including: economics, chemistry, computer science, statistical mechanics, and radiotherapy(35).

The use of the Monte Carlo method in radiation transport has resulted in the Monte Carlo method becoming ubiquitous to medical physics. The first medical physics paper on the method was published in 1949. Since then there has been an exponential growth in the number of papers mentioning the use of the Monte Carlo method alongside the introduction of several widely available code systems(34). The Monte Carlo method is considered to be the most accurate method for dose calculation to date, with some referring to it as the "gold standard".

3.2 Fundamentals of Monte Carlo Simulations

The Monte Carlo method obtains solutions by the summation of random elementary events. The random events are calculated using random numbers and probability distributions while the summation is performed by numerical integration. A rudimentary understanding of these concepts is required to grasp the inner working of a Monte Carlo simulation. The next section will briefly discuss random number sampling, probability distributions, and numerical integration with regards to the Monte Carlo method in radiation transport.

3.2.1 Random Number Generators

As the previous section alluded, the Monte Carlo method requires random numbers to run a simulation. These random numbers are generated by computer random number generator (RNG) routines. Most of these routines produce random numbers uniformly distributed over some interval, typically $[0, 1]$. However, any set of random numbers produced by a RNG routine are inherently non-random, as any computer routine is by definition predictable(12). Therefore, they are actually pseudo-random numbers, however they will be considered as random numbers for this paper and described as such. True random number generators cannot generate a large enough sequence of random numbers quickly enough for simulations in radiation therapy(36).

A random number set used in Monte Carlo simulations must appear to be independent, such that any statistical test concludes that no correlation between the numbers exists. This, as well as the number of events generally required in a simulation, calls for a very large random number set. The number of events required

in a simulation is often in the order of 10^7 to 10^{12}, depending on the simulation and accuracy sought.

RNG routines used in Monte Carlo simulations often require number seeds to start a sequence of random numbers. The use of a random number seed offers several advantages. Firstly, the same sequence can be produced on different machines. This allows results to be exactly recalculated in case of data corruption. Secondly, the analysis of simulations over large distances by different parties is possible without having to send large data files. Finally, initialising a simulation with a different seed guarantees the use of a completely different random number set(37). Using different seeds to generate completely separate random number sets allows results from simulations on cluster computer systems to be combined. It also allows for the addition of a second simulation with a different seed when a certain accuracy level has not yet been achieved by the first simulation.

3.2.2 Probability Distributions

To solve interesting problems with RNG routines, the uniformly distributed random numbers are used to draw variables from probability distributions related to the underlying physical processes. Each underlying process has its own specific weighted probability distribution which is sampled many times within a simulation.

There are a number of sampling techniques used in the construction of Monte Carlo codes. The complete details of such techniques are not required for a rudimentary grasp of the Monte Carlo method but can be found in several Monte Carlo texts(10; 12; 36). What is important to understand is that these methods map a uniformly distributed random number set onto a probability distribution function related to the

physical processes being modeled in order to obtain the parameters required. The parameters that are sampled in radiation therapy simulations are quantities such as particle trajectories, interactions, and energy deposition as the individual particles transverse through the different media.

Cross Sections

Radiation transport deals with the scattering and interactions of particles as they travel through mediums. To deal with this, probability distributions are needed to describe the likelihood of scattering or interactions occurring. If we consider a classical case such as ten pin bowling, the probability distribution is the cross sectional area of the pins to the oncoming bowling ball. In the case of an electron beam incident on any medium, the equivalent quantity is the cross sectional area of all the atoms presented to the electrons, however, atomic cross sections are not as simple as the classical ten pin bowling scenario.

Firstly, the pins themselves are not a hit or miss type of object such as those we are familiar with in the macroscopic world, but rather, the pins have a spectrum of deflection depending upon the bowling balls proximity to the scattering center of the pin(38). The closer to the scattering center, the greater the probability of interaction and the larger average deflection. Secondly, the cross section depends on the structure of both the pins and the ball. Electrons will scatter very easily in the presence of protons compared to neutrons whereas photons do not scatter very easily off either. Finally, the energy of the incoming particle will also contribute to the probability that an interaction will occur. Some interactions do not occur below a certain energy level due to the energy required to liberate particles, a so called cut-off energy.

Cross sectional data is needed for all interactions that are to be modeled in a simulation over the specific energy regime being considered. Photon cross sections are required for photoelectric absorption, Rayleigh scatter, Compton scatter, and pair production. For electrons, the cross section coefficients are required for all the collisional and radiative interactions, resulting in the unrestricted collisional and radiative stopping power respectively.

3.2.3 Numerical Integration

Monte Carlo calculations are in a formal sense just numerical integrations(36). Numerical integration methods are usually reserved for integrals where an analytical solution is very difficult to obtain without using severe approximations(12). Problems in radiation therapy require solutions to the coupled Boltzmann radiation transport equations. The system is coupled due to the coupled nature of electron and photon interactions, which will be discussed in section 3.4.3.

The solution to the radiation transport problem is difficult to obtain analytically because the parameter space of the problem is theoretically infinite due to the fact that the range of different secondary particles that can be liberated is physically unlimited(12). Practically, the parameter space is limited due to the assignment of an energy level at which we choose to stop the simulation of a particles. Nevertheless a numerical integration is required to solve the problem.

The Monte Carlo method performs numerical integration by sampling N different points, x_i, in the high dimensional parameter space, V. Each of these points is equivalent to a particle shower of an initial incident particle. The Monte Carlo integral, I in this space is given by Equation 3.1.

$$\int I dV \approx V\langle I\rangle \pm \sqrt{\frac{\langle I^2\rangle - \langle I\rangle^2}{N}}, \tag{3.1}$$

where

$$\langle I\rangle \equiv \frac{1}{N}\sum_{i=1}^{N} I(x_i), \qquad \langle I^2\rangle \equiv \frac{1}{N}\sum_{i=1}^{N} I^2(x_i). \tag{3.2}$$

From Equations 3.1 and 3.2 it can be stated that the estimated Monte Carlo integral converges to a real integral as the number of simulations, N, tends to infinity, and that the convergence rate is proportional to the square root of the number of samples(12). This leads to one of the most important statistical facts about a Monte Carlo calculation: the statistical uncertainty decreases by a factor of two if the number of simulations is increased by a factor of four. Therefore the Monte Carlo method obeys a rule of diminishing returns in regards to the number of simulations compared to the statistical accuracy of the solution.

3.3 Monte Carlo Algorithms

There are currently a number of different Monte Carlo packages available for use in radiotherapy(12). Some have been developed specifically for radiotherapy accelerator modeling, while others have been adapted from high energy physics applications. The difference between different simulation packages is usually found in their ability to simulate the transport of charged particles(10). The transport of neutral particles is relatively easy and requires substantially less computational power. Neutral particles are usually explicitly simulated at each interaction point, as the mean free path length

between interaction points is normally of the order of the simulation geometry.

The difficulty in simulating electron transport is due to the number of interactions electrons undertake before they lose all of their energy. The distance between electron interactions, with energies greater than 1 MeV, is in the range of 10^{-5} to 10^{-4} g/cm^2(10). One 6 MeV electron, which has a practical range of around 3 cm, will interact between 3×10^4 to 3×10^5 times before stopping. This would require the simulation of 10^{11} to 10^{13} electron interactions in a single simulation. Many of these interactions result in little change in energy or direction of the electron. If all these interactions were to be simulated explicitly the overall calculation time would become excessive. Therefore it is not feasible to simulate electron transport interaction by interaction. This has led to the use of Condensed History (CH) particle transport.

The Condensed History technique involves dividing all collisional and radiative charged particle interactions into hard or soft type interactions. A large number of subsequent soft type interactions are condensed and modeled in a single step, while the hard type interactions are modeled explicitly. Each electron will be transported until either a hard collision has occurred, or until it has traveled a distance equal to the step size. At the end of each step the cumulative effect of all the soft interactions on the electron's direction, energy, and position is taken into account by sampling scatter distributions from multiple scattering theory(12). A typical condensed electron history is shown in 3.1.

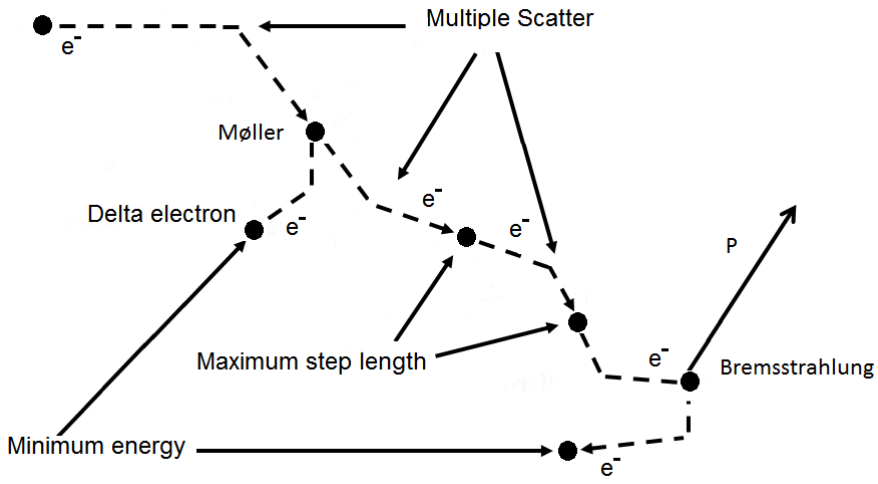

Figure 3.1: An example of a particle history created by a primary electron interacting through several processes resulting in secondary delta rays and bremsstrahlung x-rays. The simulated electron path demonstrates the Condensed History technique, where electrons travel in straight lines until either a hard collision occurs, or until they have traveled a distance equal to the step size. At the end of each step the electron changes direction and energy, this is sampled from a multiple scattering probability distribution. Reproduced from (12)

3.3.1 EGSnrc

Electron Gamma Shower (EGS) code system is a general purpose Monte Carlo simulation package for the transport of electrons and photons with energies from a few keV through to hundreds of GeV in arbitrary geometry(37). The original simulation package was developed for high energy physics in laboratories where high energy electron-photon transport models were needed(34; 39).

The latest EGS version, EGSnrc, has been reworked at the National Research Council of Canada. The EGSnrc family of code is the most widely used Monte Carlo code system in medical physics(34). It has been extensively cited in the literature. EGSnrc consists of several different codes such as BEAMnrc, DOSXYZnrc, BEAMdp,

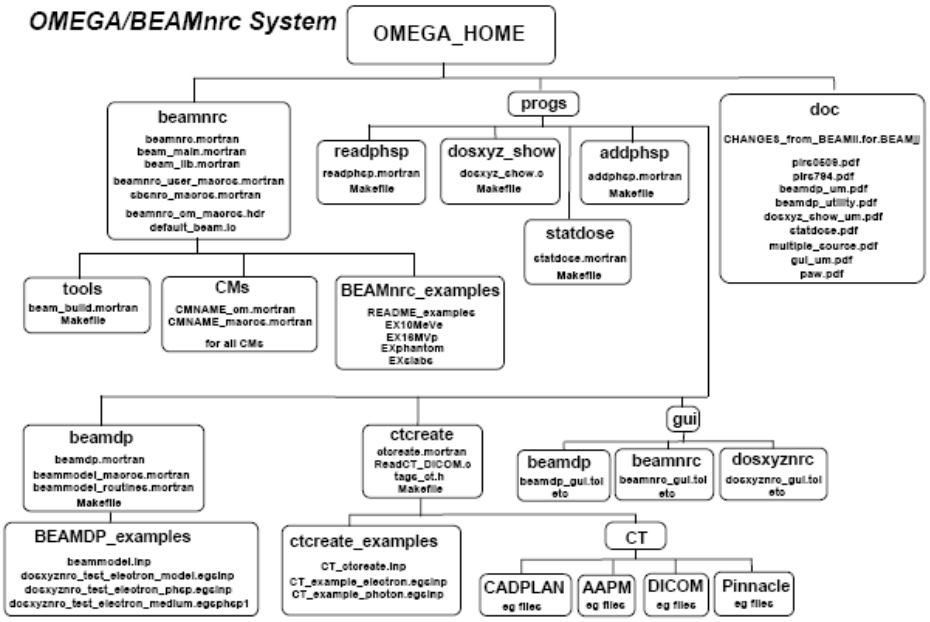

Figure 3.2: A schematic showing the user codes for the EGSnrc system indicating the modular nature of the code system. Reproduced from (37)

and Statdose. A schematic diagram of all the user codes is shown in Figure 3.2. Below is a brief description of the main codes used in this investigation.

BEAMnrc is a program designed specifically for use in radiotherapy to model different radiotherapy treatment machines, including high energy Linacs(40). It was originally part of the OMEGA project as a part of a Monte Carlo 3-D electron treatment planning system, but the BEAMnrc code is equally capable of simulating photons(28).

A Linac simulation is developed within BEAMnrc by modeling major components within the beam line using so called Component Modules (CMs). Each major component in the beam line is simulated by a separate CM. The CMs are either cylindrical or rectangular in their geometry and they are situated between parallel

planes perpendicular to the Z axis of the accelerator. The CMs can be combined in any arbitrary order as long as no CM overlaps or surrounds any another CM. The details of the different types of CMs available can be found in the BEAMnrc manual(40). The use of CMs makes the simulation of a Linac conceptually simple to perform.

The methodology of simulating a Linac in BEAMnrc has been extensively covered in the literature and the BEAMnrc manual(40). The simulation results are usually scored at the end of a particular CM. This creates a phase space file which contains all the information of every particle which passes the scoring plane. This phase space file can then be used with other user codes to perform dose calculations, or, be analysed itself.

DOSXYZnrc is a general purpose user code which allows the calculation of absorbed dose in rectilinear 3D voxel phantoms. Voxel dimensions, material composition and density are completely variable in all dimensions. DOSXYZnrc simulates the transport of electrons and photons from either inbuilt source models, such as mono-energetic or parallel beams, as well as user's phase space files generated from BEAMnrc.

BEAMdp and Statdose are data processing codes mainly used for statistical purposes. BEAMdp can be used to process phase space files created from BEAMnrc to derive energy, planar fluence, mean energy, and angular distributions of the particles scored. Statdose can be used to process 3-dimensional dose output files from DOSXYZnrc. Statdose can be used to normalise, re-bin, plot, and analyse dose distributions as well as compare two different dose distributions graphically and statistically.

Variance Reduction

Monte Carlo calculations can be very heavy on computer resources and thus time consuming. Aside from increasing computer resources, several techniques can be employed to decrease calculation times without unduly changing the statistical accuracy of the results. These techniques are known as variance reduction techniques. Many different variance reduction techniques are available for photon beam simulations, such as leading particle biasing, photon splitting, path length biasing and Russian roulette(40). There are fewer variance reduction techniques available for use in electron beam simulations.

One important variance reduction technique available for electron beams is range rejection. Range rejection is the ability to reject tracking electrons that do not have enough energy to escape a certain region. If the electron cannot reach a boundary then the history is terminated. The method for rejecting these electrons is very fast to compute as the range and distance are already calculated for other purposes(37).

Users can also implement a more efficient form of range rejection, for instance, rejecting any electron which cannot reach the scoring plane. Electrons in the upper section of the treatment head require a certain amount of energy to be able to reach the scoring plane. Therefore, simulating any particle in the upper head which does not have enough energy to travel to the scoring plane is inefficient in terms of computational time. Large sections of several components may also lie outside the main beam line and are shielded by lower components such as the jaws and electron applicator. Many of the electrons scattered into these sections of CMs are also unlikely to reach the scoring plane.

Setting individual range rejection energy levels for different regions in CMs

throughout the treatment head, based on their location in relation to the main beam line and distance from the scoring plane, can substantially decrease the calculation time needed. If range rejection energies are correctly chosen the calculation efficiency can be greatly increased while maintaining accuracy in the simulations(37). Range rejection does involve one approximation: that a rejected electron could emit bremsstrahlung photons which have the ability to escape the region. This may increase the uncertainty in regions such as the bremsstrahlung tail.

3.3.2 Xio eMC

The treatment planning system's algorithm under investigation in this work is XiO's electron Monte Carlo (eMC) algorithm. The eMC algorithm is based on the XMVC Monte Carlo algorithm, which is a fast algorithm for photons extended from the Voxel-Monte-Carlo (VMC) algorithm. XiO's eMC uses a condensed electron history technique and is said to be able to quickly calculate patient dose distributions which are clinically acceptable. The beam models used within the code have been developed by Electa(12) and are individualised using a limited number of user beam measurements. The model consists of a weighted combination of direct and indirect electron and photon sources. The dose calculation is performed by XMVC, while the interface is identical to XiO's interface. XiO's eMC is available for all major Linac vendors and has been locally verified to be able to model a Siemens Artiste Linac to a clinically acceptable level.

TPS Monte Carlo algorithms may require a special parameter which determines the endpoint of the calculation. This parameter is needed as the natural end point of an MC simulation is when all histories have been simulated. Since the general user

has no idea how many particle simulations are required to gain a particular level of accuracy, allowing the calculation to complete all requested particle simulations may not be a suitable endpoint. XiO's eMC completes a calculation when the statistical accuracy requested has been reached. The statistical accuracy of dose calculation in eMC is assessed by a parameter known as the mean relative statistical uncertainty (MRSU). The MRSU is defined by Equation 3.3(41).

$$MRSU = \sqrt{\frac{1}{N} \sum_{D(r_i) \geq aD_{max}}^{N} \frac{\sigma(r_i)}{D_i}^2}, \tag{3.3}$$

where D_i is the dose delivered to the i^{th} voxel in the calculation region, $\sigma(r_i)$ is the statistical uncertainty of the dose in the i^{th} voxel. The quotient is summed over all N voxels where the dose is higher than aD_{max}, also known as the MRSU threshold. The user has the ability to choose the value of a, however it is recommend to be set at 50 % of the maximum dose for patient calculations(12). The code will perform a certain number of simulations and then calculate the MRSU value before continuing. The calculation will then continue until the desired MRSU value is obtained, or, once all the specified histories have been simulated.

One of the advantages of a Monte Carlo calculation is their ability to accurately calculate dose when material in-homogeneities are present. The material input data for eMC is usually in the form of a CT scan. The only material related property in a CT scan is the CT number which is converted to electron density using the scanners unique CT to ED table. XiO's eMC assigns a mass density to each voxel based on the electron density and uses an empirical equation to estimate the stopping and scattering power of that material based on the assigned mass density(41).

3.4 Radiation Interactions with Matter

For a Monte Carlo simulation to accurately represent a physical situation, the underlying phenomenon must be adequately modeled. In regards to medical physics the underlying phenomenon to be modeled is the transport and interaction of electrons and photons with matter.[1] Electrons and photons interact with their surrounding medium through a number of different processes. The ability to link outcomes of these processes forms the basis for a successful Monte Carlo simulation. For a simulation to be efficient, only interactions which are important in regards to the relevant energy spectrum should be considered, in addition to limiting unessential interactions which result in an excess amount of CPU time which contribute minimally to the final result.

The main quantity of interest which results from these interactions is the absorbed does to a medium. The absorbed dose, D, is defined as

$$D = \frac{d\bar{\epsilon}}{dm}, \tag{3.4}$$

where $d\bar{\epsilon}$ is the mean energy imparted to mass of dm. The absorbed dose is directly related to energy deposition of photons and electrons through absorption mechanisms of interactions with the medium which are discussed in the next section.

3.4.1 Photon Interactions

There are several types of interactions that photons may undergo with matter which must be considered in a radiation transport simulation. These interactions can be

[1] Some more specialist modalities may be interested in the transport of protons, neutrons and other exotic particles.

divided into two groups, interactions involving nuclei of the absorbing material or interactions involving the orbital electrons of the absorbing material. Interactions that involve nuclei are pair production, photon-disintegration, and the photo-nuclear interaction. The photo-nuclear effect is not a significant contributor to dose in the energy regime under consideration, therefore it is not discussed here(38).

Photon interactions that involve orbital electrons either interacted with loosely bound electrons or tightly bound electrons. The difference between the definition of loosely bound and tightly bound electrons is not a characteristic of the absorbing material alone, rather it is also related to the relative magnitude of the interacting photon's energy and the electron's binding energy. A loosely bound electron is one whose binding energy is equal to or less than the incoming photon, and a tightly bound electron is one whose binding energy is much greater than the incoming photon's energy(38).

Loosely bound interactions are: Thompson scattering, the Compton Effect and triplet production. Tightly bound electron interactions are the photoelectric effects and Rayleigh scattering. Thompson scattering has a minor effect on the photons in the energy range involved and will therefore also be excluded from the discussion. The photoelectric effect, Compton effect, pair production, and triplet production transfer energy from the photon field to the electron field, which then impart their energy to the surrounding matter through the processes to be described in section 3.4.2. One of these three interactions will dominate depending on the material and the energy of the interacting photon.

Compton Effect

An interaction of a photon with a loosely bound electron of an absorbing material is known as the Compton effect or incoherent scattering. After the interaction, an electron is ejected from the absorber, which is known as a Compton electron, and the photon is scattered. The final energy of the scattered photon is the difference between the original energy of the photon, and the kinetic and binding energy of the final electron. Figure 3.3c shows a schematic of the Compton effect.

EGSnrc uses the total Klein-Nishina cross section to simulate incoherent Compton scattering. The Klein-Nishina cross section ignores the electron binding energy and considers the electron to be at rest. The equation for the Klein-Nishina cross section is shown in Equation 3.5.

$$\frac{\mathrm{d}\sigma}{\mathrm{d}cos\theta} = \pi r_0^2 Z X_{KN}, \tag{3.5}$$

where θ is the polar angle between the incident and scattered photon, Z is the atomic number, and X_{KN} is a term related to the photon's energy. More details can be found in the EGSnrc manual(37)

Photoelectric Effect

An interaction of a photon and a tightly bound inner shell electron is known as the photoelectric effect. The incoming photon is completely absorbed and the inner shell electron is ejected from the atom. The electron has a kinetic energy equal to the difference of the original photon's energy and the binding energy of the inner shelled electron. Figure 3.3a shows a schematic of the photoelectric effect.

The photoelectric effect is modeled in EGSnrc by using total cross section data obtained from a standalone Preprocessor for EGS (PEGS) program. More details can be found in the EGSnrc user manual(37).

Pair and Triplet Production

An interaction of a photon and the Coulomb field of a nucleus resulting in the complete absorption of the photon and ejections of a positron-electron pair is known as pair production. An interaction of a photon and a Coulomb field of an orbital electron resulting in the complete absorption of the photon and the ejection of a positron-electron pair as well as the electron itself is known as triplet production. Triplet production occurs at the same rate as pair production in hydrogen, but becomes increasingly less frequent as the atomic number increases(10).

Due to the creation of a positron-electron pair in both pair and triplet production there is a cut off energy for the interaction to occur. This cutoff energy is twice the rest energy of an electron, which is 1.02 MeV. Figure 3.3d and 3.3e shows a schematic of pair production and triplet production.

EGSnrc by default does not explicitly simulate pair and triplet production but uses a combined pair-triplet cross section. This cross section data is derived from scattering theory using the extreme relativistic first Born approximation. More details can be found in the EGSnrc user manual(37).

Rayleigh Scatter

An interaction of a photon and a tightly bound electron from an absorbing atom resulting in a coherent scattering of the photon is known as Rayleigh scattering. The

absorbing atom is neither excited nor ionised. Recoiling momentum is transferred to the absorbing atom, however, the energy is very small and the scattered photon has essentially the same energy as the original photon.

3.4.2 Electron Interactions

As electrons traverse any surrounding medium they experience interactions between their surrounding electric Coulomb field and the surrounding electron Coulomb fields of electrons and nuclei within the medium. This process is known as Coulomb scattering. Much of what is known about Coulomb scattering comes from various scattering experiments, such as the famous Geiger and Marsden experiment in 1909(29) from which the Rutherford α scattering model was conceived. However, when considering electrons there are various other parameters which complicate the scattering process. These parameters are such things as electron and nuclear spin, relativistic and quantum effects, recoil of the nucleus, and the finite size of the nucleus(29).

Coulomb scattering can be divided into two groups, elastic and inelastic Coulomb scattering. Inelastic scattering can be further separated into radiative and collisional scattering. The type of interaction that an electron will undergo depends on the classic impact parameter and the radius of the atom, a. The classic impact parameter, b, is defined as the perpendicular distance between the nucleus and the electron's trajectory before the interaction. Figure 3.4 graphically shows the definition of the classic impact parameter.

Electron interactions where the classic impact parameter is approximately equal to the radius of the nucleus ($b \approx$ a) will undergo an inelastic Coulomb interaction

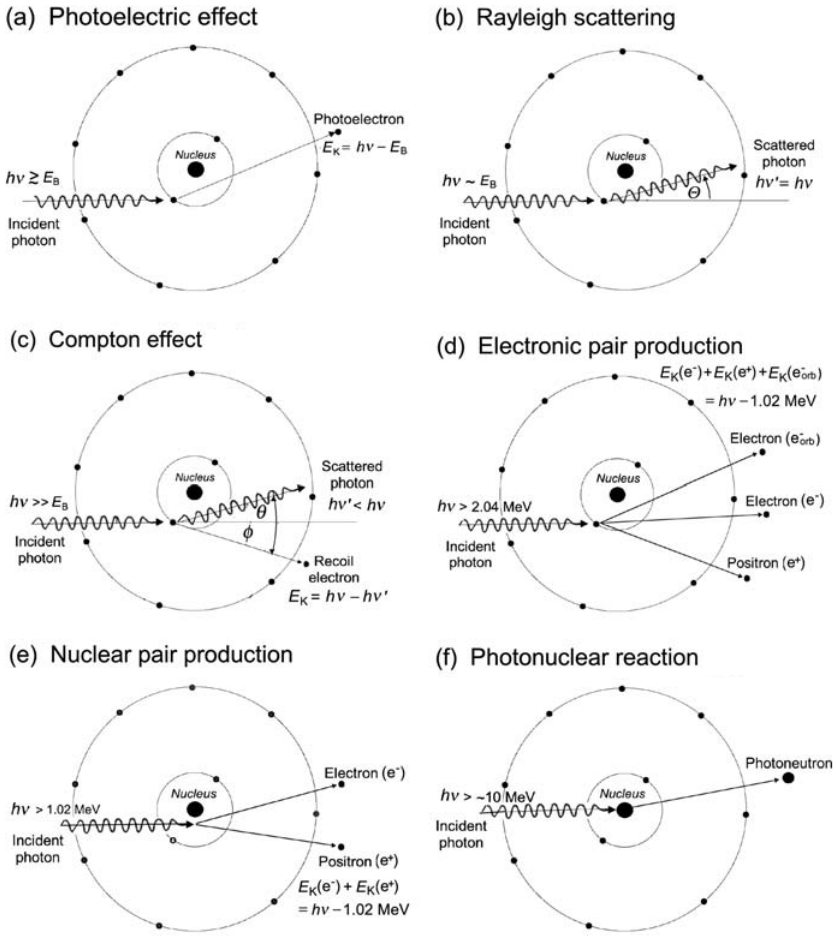

Figure 3.3: A diagram showing possible photon interactions with an atom. Showing: (a) The photoelectric effect- An interaction of a photon with a lightly bound electron resulting in complete absorption of the photon and ejection of an electron. (b) Rayleigh scattering- An interaction of a photon with a tightly bound electron resulting in the scattering of the photon. (c) The Compton effect- An interaction of a photon with a loosely bound electron resulting in a scattered photon and the ejection of a Compton electron. (d) Triplet production- An interaction of a photon with the Coulomb field of an atomic electron resulting in complete absorption of the photon and the ejection of a positron-electron pair and the interacting atomic electron. (e) Pair production- An interaction of a photon with the Coulomb field of a nucleus resulting in the complete absorption of the photon and ejection of a positron-electron pair. (f) The photonuclear reaction- An interaction of a photon with the Coulomb field of the nucleus resulting in complete absorption of the photon and the ejection of a photo-neutron. Reproduced from (29).

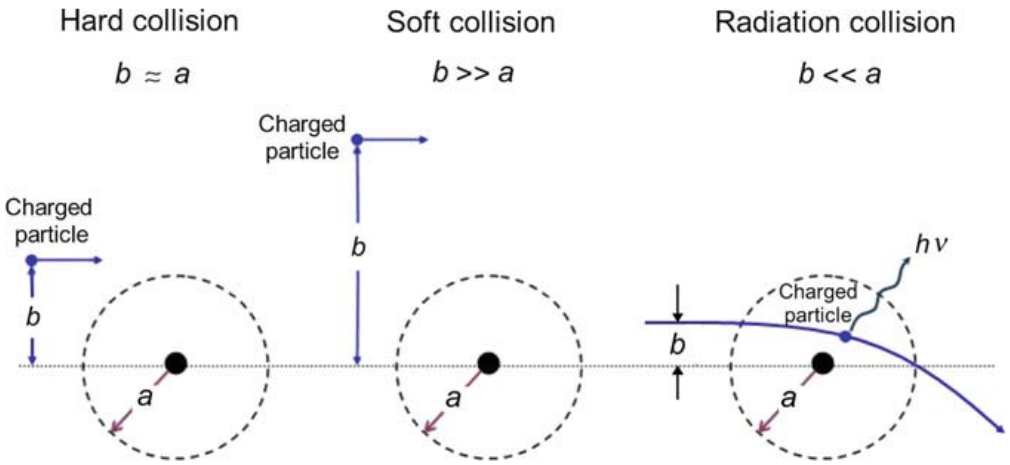

Figure 3.4: A schematic showing the three types of electron interactions with atomic material. The type of interaction depends on the relative size of both the classic impact parameter, b, and the radius of the nucleus, a. Hard collisions occur when $a \approx b$, soft collisions occur when $b >> a$ and radiative collisions occur when $b << a$. Reproduced from (29).

with the Coulomb field of the orbital electrons. These interactions are known as hard collision. The result of these interactions may lead to large energy losses and directional changes to the electron as well as the possibility of electrons being ejected. These are known as a δ rays and lead to ionisation of the atom. The ionised atom relaxes through either characteristic x-rays, or Auger and Coster-Kronig electrons. The number of hard collisions experienced by an electron is relatively small; however, the electron will lose approximately half of its kinetic energy after each hard collision.

Electron interaction where the classic impact parameter is much less or equal to the radius of the nucleus ($b << a$) will undergo an inelastic Coulomb interaction with the Coulomb field of the nucleus. These interactions are known as radiative collisions.

The majority of these interactions are elastic but several may lead to significant energy loss and directional change of the electron as well as the production of Bremsstrahlung x-rays.

Electron interactions where the classic impact parameter is much greater than the radius of the nucleus ($b >> a$) will undergo elastic Coulomb interactions with the Coulomb field of the whole atom. The result of these interactions can cause deflections of the original electron, however a negligible amount of energy is transferred to the medium from the electron. An electron undergoes a large number of soft interactions such that approximately 50 % of an electron's energy is lost through this process(29).

EGSnrc uses Møller scattering theory to model hard electron-electron interactions and uses the screened Rutherford elastic model based on Mott scattering theory to model electron-nucleus interactions. More details can be found in (37). Elastic scattering is not explicitly modeled but the cumulative effect is sampled during an electron's Condensed History step, as described in section 3.3.

3.4.3 Coupled Radiation Field

The above description of the interactions of photons and electrons describes how the electron and photon radiation fields are coupled. Photon interactions can transfer energy from the photon field to the electron field, interactions such as: the photoelectric effect, Compton scattering, pair production, and triplet production. Likewise, electron interactions can transfer energy from the electron field to the photon field, interactions such as: Bremsstrahlung production, annihilation of positrons, as well as excitation and ionisation resulting in relaxation through characteristic x-rays. The coupling of the photon electron field can be seen clearly

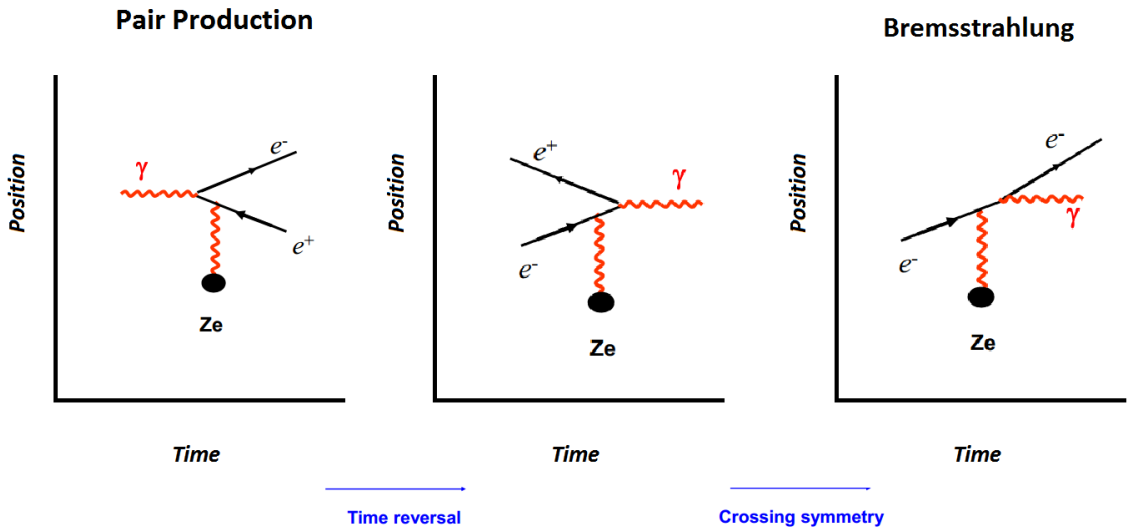

Figure 3.5: Feynman diagram showing the close relationship between pair production and Bremsstrahlung interactions through the Feynman rules of time reversal and crossing symmetry about the vertex. This demonstrates the close coupling of the photon and electron radiation fields.

between the pair production and Bremsstrahlung interactions when using a Feynman diagram to show the relationship between pair production and Bremsstrahlung through the Feynman rules of time reversal and crossing symmetry, shown in Figure 3.5.

3.5 Summary

The Monte Carlo method can be used effectively to gain statistical insight into unpredictable problems by using random numbers, numerical integration, and probability distributions. In radiotherapy, it is used to predict dose through the simulation of millions of individual photons and electrons by summating the energy deposited through their interactions. The types of interactions photons and electrons undergo are interactions such as the photoelectric effect, Compton effect, pair production, bremsstrahlung, and hard electron collisions resulting in ionisation or excitation.

There are several advantages in using Monte Carlo methods over conventional algorithms and measurements. This includes the ability to set volume elements (voxels) to any arbitrary size. This allows the measurement of ill-defined point parameters such as the electron backscatter factor. A Monte Carlo model also removes any perturbation effects due to dosimeters as well as uncertainties in experimental set ups.

This has led to the Monte Carlo technique becoming the gold standard in dose prediction for radiotherapy; however, it is important to understand that a simulation is an idealised model of radiation interaction in a idealised geometric environment. This idealised model will only ever be as good as the data used to create it or the current understanding and implementation of the physics involved.

Chapter 4

Monte Carlo Simulation of a Linear Accelerator

The modeling of an electron beam accelerator is generally more difficult than modeling a photon beam accelerator. This is a consequence of the complex interaction processes electrons undergo while transversing a medium, as discussed in section 3.4.2. An MC simulation of an electron beam is said to be the most accurate method of predicting dose for an electron beam, however, the predicted dose is only as good as the underlying model and algorithm, and must be verified against physical measurements.

This chapter details the iterative method used to develop an MC model of a Siemens Artiste's Linac treatment head with several standard electron cones using the EGSnrc code package. A description of the components modeled in BEAMnrc and details of the initial beam parameters is discussed. Validation of the model against measured dose data for several electron energies and field sizes is also included. Parameters discussed in Chapter 2 will be used to assess the accuracy of the model.

The model's accuracy sought in this work is 2 % 2 mm dose-distance to agreement between the measured and the calculated dose profiles.

4.1 Methods and Materials

The most recent version (4-r 2.3.1) at the time of writing of BEAMnrc(28) code, based on EGSnrc(37) code, was used to simulate a treatment head of a Siemens Artiste Linac. The simulations were carried out on a 3.1 GHz Intel Core i5 CPU personal computer with 4 GB of RAM.

The key Linac components, as described in section 2.1, were modeled within the BEAMnrc code using the inbuilt Component Modules (CM). Geometric details of the components were supplied by the manufacturer. A non-disclosure agreement was signed with the manufacturer. Therefore, specification of the components will not be reproduced here. Figure 4.1 shows a cross sectional schematic of the treatment head and electron applicator along the $X - Z$ axis modeled in BEAMnrc. The Z axis is directed along the collimator axis of the Linac, the Y and X axis are parallel and perpendicular to the Linac's treatment couch respectfully.

The different CMs used for the different components are tabulated in 4.1. A detailed description of the geometry of the different component modules can be found in the BEAMnrc manual(40). All the components were modeled to the manufactures dimensions except the collimating jaws. Modeling the intricacies of the entire X-MLC and Y-jaws was concluded to have little effect on the electron distribution and fluence as they are both retracted well outside the field when the machine is operating in electron mode. The Y-jaw and X-MLC were modeled as solid tungsten blocks with a

divergent face using the JAWS CM. The Cutoff energies for each CM was optimised according to the discussion in section 3.3.1. This should improve the overall efficiency of the model.

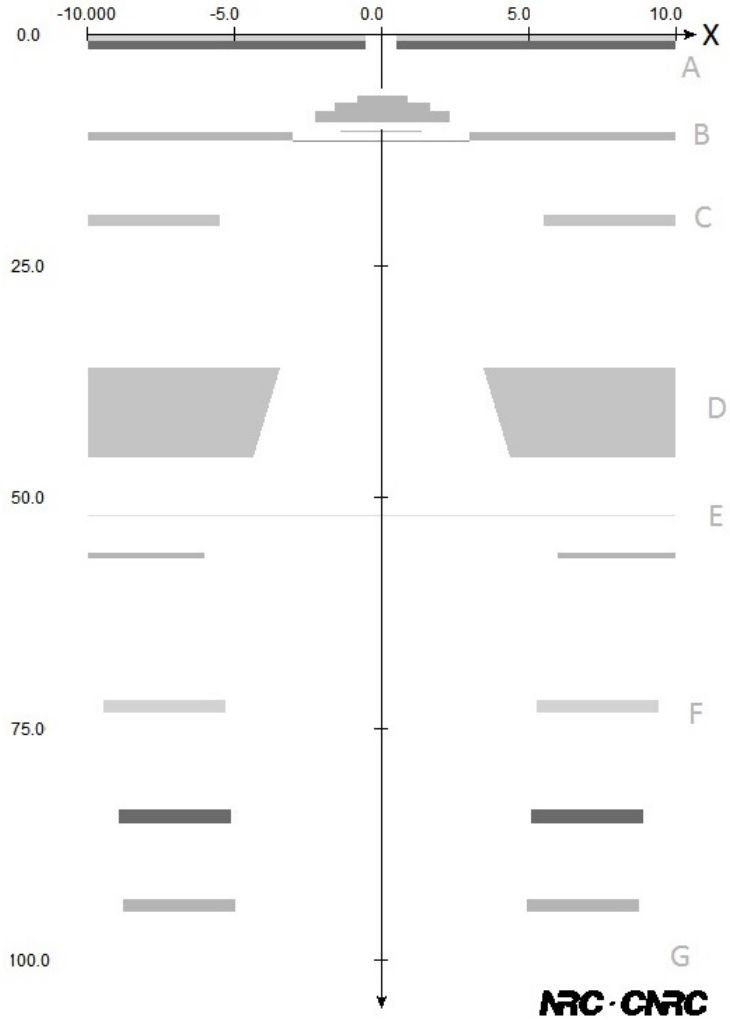

Figure 4.1: Cross sectional schematic of the Siemens Artiste treatment head Monte Carlo model, showing components used in BEAMnrc(28). From top, A: exit window and primary scattering foil, B: secondary scattering foil and dose monitoring chamber, C: shielding plate, D: lower X-jaws (MLC), E: reticule, F: electron applicator, G: air gap to isocentre. (Schematic is not to scale).

Component	Component Module (CM)
Exit window and primary scattering foil	CONESTAK
Secondary scattering foil	CONESTAK
Electron dose chamber	CHAMBER
Shielding plate	APPLICATOR
Y-jaws and X-MLC	JAWS
Reticule	SLABS
Electron applicator and Square Cutout	APPLICATOR
Air gap	SLABS

Table 4.1: Table of components in the electron beam line included in the Linac model and the component modules used to model them in the BEAMnrc Monte Carlo code in order of increasing Z position.

Simulation Parameters in BEAMnrc and DOSXYZnrc for all experiments were largely unchanged from the default settings. The lower energy electron (ECUT/AE) and photon (PCUT/AP) cut-off energy was set to 0.7 MeV and 0.1 MeV respectively. These levels represent the lowest energy to which a particle is tracked, remembering that an electron posseses a rest mass of 0.511 MeV. The electron step algorithm used was the Parameter Reduced Electron-Step Transport Algorithm II (PRESTA II) algorithm and the boundary crossing algorithm used was the EXACT algorithm. More details on these parameters and algorithms can be found in the BEAMnrc and DOSXYZnrc user manuals(40; 42).

The output of a BEAMnrc MC simulation consists of a phase space file. The phase space file contains information on every particle that crosses a particular plane. This plane is chosen by the user and can be at the end of any CM in a BEAMnrc MC simulation. The information related to individual particles contained inside a phase space file indicats such things as: the particles position, direction, charge, and energy.

In this simulation, phase space data was scored at an isocentric plane, which

was located 50 mm from the end of the electron applicators, for all electron energies and applicators simulated. The phase space data was later used to calculate dose distributions in water using the DOSXYZnrc code. This approach was used rather than compiling a shared library, where the DOSXYZnrc code could directly call the BEAMnrc code in the same simulation, as the phase space files produced will be used multiple times on different phantoms. Performing the simulations in this way reduces the overall calculation time required, which justifies the need to store large phase space file. On average, the phase space files were 3.0 GB in size.

Verification of the model was performed through the comparison of depth dose curves and beam profiles to physical measurements. Comparisons of isodose plots were also made with the treatment planning system, XiO eMC algorithm. The physical measurements were acquired using a scanning water phantom (Blue Phantom 2, IBA advanced radiotherapy, Germany). The measurements were made on several Siemens Artiste machines using a 3G-pSi diode radiation field detector from Scanditronix-Wellhöfer (Scanditronix–Wellhöfer Dosimetry, IBA advanced radiotherapy, Germany). Measurements for nominal energies of 6, 9, 12, and 15 MeV with standard electron applicators of 10 x 10 cm, 15 x 15 cm, 20 x 20 cm, and 25 x 25 cm as well as a 50 mm diameter circle were used to verify the model. Electron beam parameters discussed in section 2.3 were compared to assess and tune the model to the desired accuracy of 2 % 2 mm.

This level of accuracy was used as Van Dyke et. al. (43) stated that electron dose calculation algorithms should be able to achieve 2 % 2 mm accuracy along the central axis PDD, allowing for a larger error in the built up region. The rest of the dose distribution should achieve at least a 4 % 4 mm accuracy; however, the goal for this

study is to apply the 2 % 2 mm Van Dyke criterion over the entire dose distribution, including the build up region.

DOSXYZnrc Verification Phantom

The DOSXYZnrc verification phantom used consisted of a plane of rectangular voxels along the $X - Z$ axis. This allowed PDDs, profiles and isodose curves to be obtained from the output of a single simulation. Voxels size for the phantom were set to an (X, Y, Z) size of $(1.0, 5.0, 0.5)$ mm for energies 6 and 9 MeV and $(1.0, 5.0, 1.0)$ mm for energies 12 and 15 MeV. A 200 mm wide area around these voxels was set to water, except in the positive Z direction; therefore the resulting phantom is roughly a 400 mm cube of water. This allows the simulation results to be compared directly to the measured results.

The output file from DOSXYZnrc is in the form of a text file and contains information on the simulation geometry, voxel dose, and uncertainty results. The file was read into an Excel spread sheet and a macro was coded to automatically re-organise the data into appropriate dose planes using the header information. An input was also included to automatically select different profile depths. The profiles and PDDs were automatically graphed and compared to the measured data. The Excel macro also calculated the electron beam parameters described in section 2.3 for the simulation results.

Initial Beam Parameters

Several initial beam parameters are required as inputs in the BEAMnrc simulation. The initial beam parameters are used to describe the electron beam as it exits

the bending magnet system and enters the treatment head. The beam parameters required are the type of beam (e.g. point, rectangular or elliptical), the size, energy distribution, and initial divergence.

The initial beam parameters were not supplied with the manufacturer's data as they are not identical for every machine. Rather, they depend on the customer's requirements and initial machine set up. The lack of knowledge regarding the initial beam parameters adds to the difficulty in modeling electron beams(13; 28).

The focal spot size can be experimentally determined as described by Haung et. al. (13), however, this can be tedious and time consuming to perform. Furthermore, the current model aims to be a generic model of several beam matched Siemens Artiste machines whose focal spots are likely different. Therefore, determining the actual focal spot's size was avoided in favour of a generic focal spot size capable of modeling a generic Artiste machine.

The initial beam parameters in previous studies have typically been a mono-energetic, mono-directional pencil beam with a Gaussian fluence distribution of 1-2 mm in radius(33; 44; 45; 46; 47). The starting energy is usually estimated using Equation 2.8 and measured values of R_{50}. An iterative method is then employed to the initial energy to tune the model until the model's R_{50} matches the physical R_{50}. Previous studies using this method, along with the manufacturer's data, have achieved the accuracy sought here. Therefore, the initial beam parameters chosen were a mono-energetic pencil beam with a Gaussian fluence distribution of radius 1 mm. The starting energy, E_0, was estimated from data obtained from scanning water phantom measurements. This starting energy was then iteratively adjusted to tune the model to match the physical measurements.

4.2 Simulation of a Siemens Artiste Linac

4.2.1 Initial Simulation Results

The results of using the iterative method and initial beam parameters described in section 4.2.1 are shown in Figures 4.2 and 4.3. This method could not achieve the desired accuracy over the entire PDD. From Figure 4.2, it can be seen that the BEAMnrc MC simulation predicts a lower build up dose than the measured build up dose. The PDD curve was within 2 % of the measured value in the range of d_{max} to R_{50}. The model also predicts that the dose should fall more quickly than what the measured results show beyond the depth of R_{50}.

The profile results show worse agreement than the PDD results. Figure 4.3 shows a comparison of profiles from the BEAMnrc MC simulation against the physical measurements for several depths. It can be seen that the simulation disagreement increases as the distance increases from the central axis. Figure 4.3 also reflects the disparity between measured and calculated PDD curves in the different depth profiles.

The initial results showed larger than expected differences when compared to the measured data. Initially it was thought that this was caused by an error in the implementations of the manufacturer's data into BEAMnrc. After extensive checking of the geometric data in the model this was ruled out. It was then concluded that the initial pencil beam parameters were incorrect.

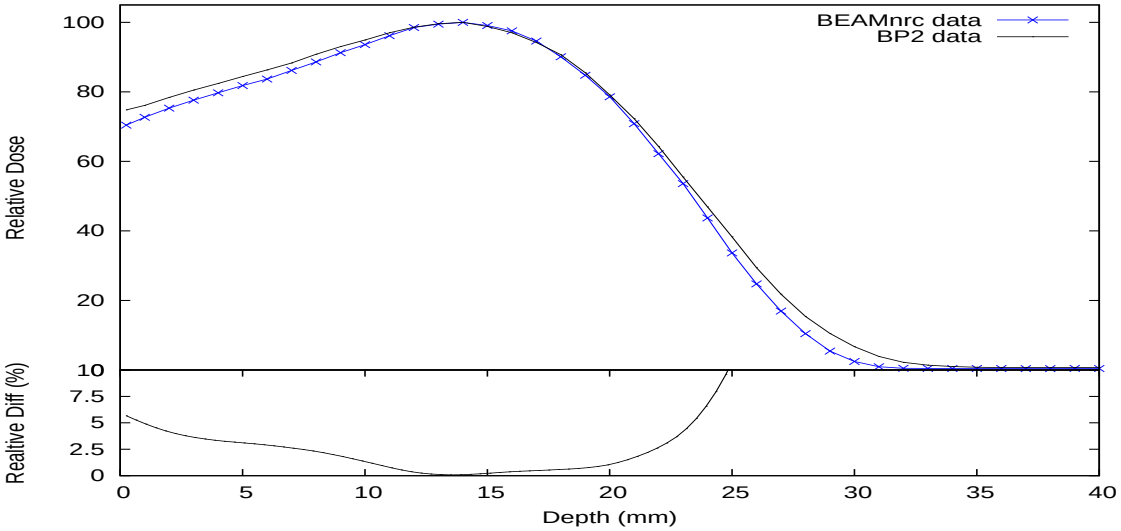

Figure 4.2: Percentage depth dose curves for BEAMnrc Monte Carlo simulation (blue) and water phantom measurements (black) of a Siemens Artiste Linac 6 MeV electron beam with 10 cm square applicator attached, using initial source settings of a mono-energetic pencil beam with a Gaussian fluence distribution.

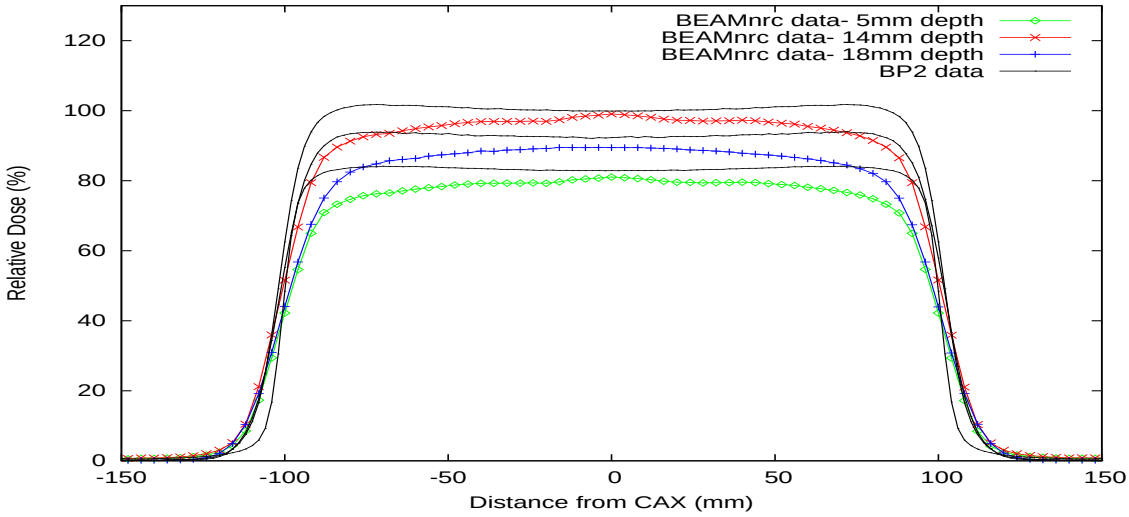

Figure 4.3: Profile curves for BEAMnrc Monte Carlo simulation (coloured) and water phantom measurements (black) of a Siemens Artiste Linac 6 MeV electron beam with 20 cm rectangular applicator attached, using the initial source settings of mono-energetic pencil beam with a Gaussian fluence distribution.

When considering the type of bending magnet system employed (section 2.2.1) it was concluded that the initial electron beam could not be modeled by a mono-energetic pencil beam. The need for a wider energy spread is evident in the PDD results. Energy spread in the initial beam would increase the dose beyond d_{max}, due to higher energy electrons penetrating to greater depths. The surface dose of the PDD would also increase as lower energy electrons will penetrate less and deposit their dose closer to the surface. Therefore, determining the required degree of energy spread should improve the model.

Although the energy spread was considered to be the most important variable that requires altering, there are three other variables in the initial pencil beam that may require alterations to further improve the models PDD and profile accuracy. These are; the beam radius, divergence, and radial distributions. To determine the effects each of these parameter on the beam profiles, a sensitivity analysis was performed. This type of sensitivity analysis has previously been performed by Haung et. al.(13). Haung et. al. determined the effect of beam radius, angular spread, energy, and the positioning and thickness of the scattering foil on the electron fluence at the scoring plane.

These parameters, which included the scattering foil thickness, were adjusted independently to determine their effect on the fluence uniformity verses radial distance from the central axis (CAX). A model with no secondary scattering foil was also simulated to determine the magnitude of the contribution from the secondary scattering foil. The model was scored at 100 cm, and the phase space was then analysed using BEAMdp(48). The initial pencil beam parameters discussed in section 4.2.1 were used as the base line for comparison. Radial fluence results normalised to

the central axis for the different parameters are shown in Figure 4.4.

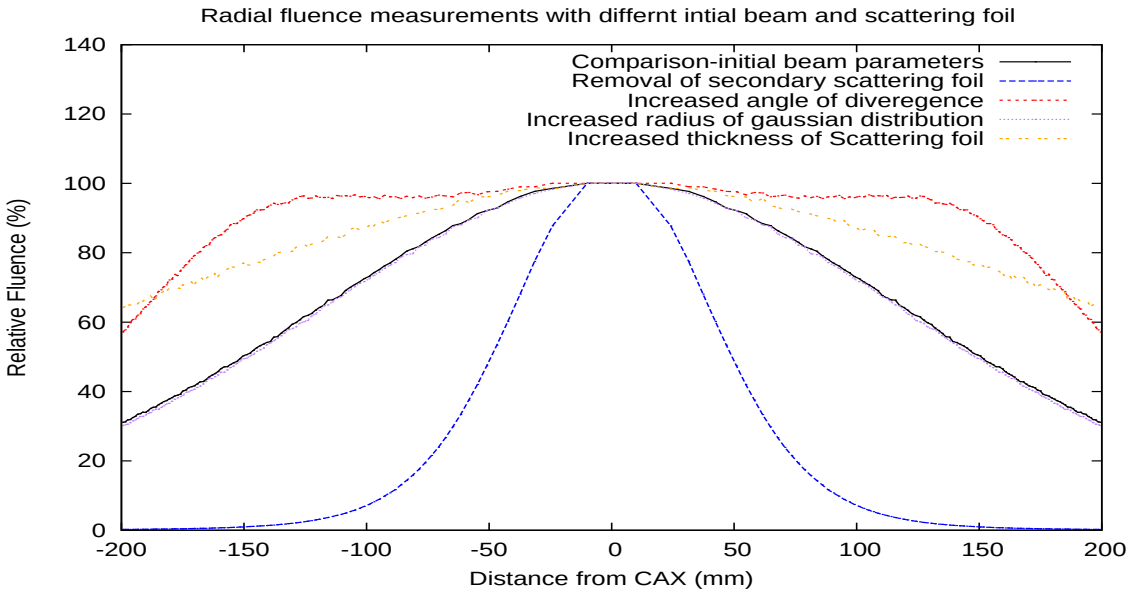

Figure 4.4: Sensitivity analysis of electron fluence with distance from the central axis using different initial beam parameters. Initial beam parameters were independently adjusted to determine the relative effect each parameter had on the radial electron fluence. Initial beam parameters that were adjusted were: the beam radius, angle of divergence, and thickness of the secondary scattering foil. Results are compared to a mono-energetic beam with Gaussian fluence distribution with a radius of 1 mm with the manufactures scattering foil dimensions. Fluence measurements were made at 100 cm SSD.

To achieve a flat beam for all electron applicators it is assumed that the radial fluence vs. distance from the CAX should be relatively flat over the largest field size to be modeled, which corresponds to 125 mm at the isocentre. Figure 4.4 shows that increasing the beam divergence greatly improves the fluence uniformity. Increasing the thickness of the secondary foil also had a strong effect. Increasing the beam radius had no effect over the range of radial sizes commonly reported in the literature. Figure 4.4 also shows the large effect that the second scattering foil has on the radial fluence distribution when compared to the distribution from a model without the secondary

scattering foil present.

Although changing the scattering foil thickness improves the radial fluency profile, it may alter the energy spectrum, as well as possibly increasing the proportion of photon contamination within the beam. It was decided to retain the scattering thickness provided by the manufacture. The results from the sensitivity analysis were consistent with results from Haung et. al.(13).

A value for the divergence was obtained from the sensitivity analysis that provided a relatively flat fluence over the beam width. The beam radius, peak energy, and energy spread were finely adjusted until the model achieved the desired accuracy for each energy with a 10×10 cm electron applicator. The results showed that the beam divergence had the greatest effect on improving the beam profiles. The beam radius, peak energy and energy spread have little effect on the beam profiles and these parameters were used to iteratively tune the model's PDD. The final beam parameters and BEAMnrc simulation times are shown in Table 4.2 for all energies for a 10×10 cm electron applicator.

Initial Beam Parameters for a 10 by 10 cm applicator				
Beam	6 MeV	9 MeV	12 MeV	15 MeV
Peak energy (MeV)	6.40	9.40	12.49	16.15
FWHM of energy spectrum	0.21	0.30	0.30	0.25
Angular Divergence (°)	4.80	4.40	3.30	3.30
Beam radius (mm)	1.00	1.00	1.00	1.00
Number of Particles in phase space ($\times 10^6$)	93.00	83.00	102.00	110.00
Ratio of electrons to photons	0.53	0.45	0.36	0.22
Simulation time (Hr)	10.10	10.70	12.05	15.47

Table 4.2: Final beam parameters and simulation results of an BEAMnrc MC simulation of a Siemens Artiste for 6, 9, 12 and 15 MeV electron beams for a 10×10 cm electron applicator.

To determine if the parameters in Table 4.2 were suitable for all field sizes a quick

comparison of the largest electron field size possible was performed. Large electron field sizes are said to be the most sensitive to the initial beam parameters, therefore, if the parameters produce acceptable results for a large field size then they are more than likely able to produce acceptable results for all smaller field sizes(45). The largest (non-clinical) field size available is an open electron field with no electron applicator with jaws set to 40×40 cm. This was simulated and the profile as well as PDD comparisons to measured results showed excellent agreement for all energies, this gives confidence that the initial beam parameters are correct. Figure 4.5 shows profile results for the 6 MeV electron beam without an electron applicator, other energies profiles are much the same and are not reproduced here.

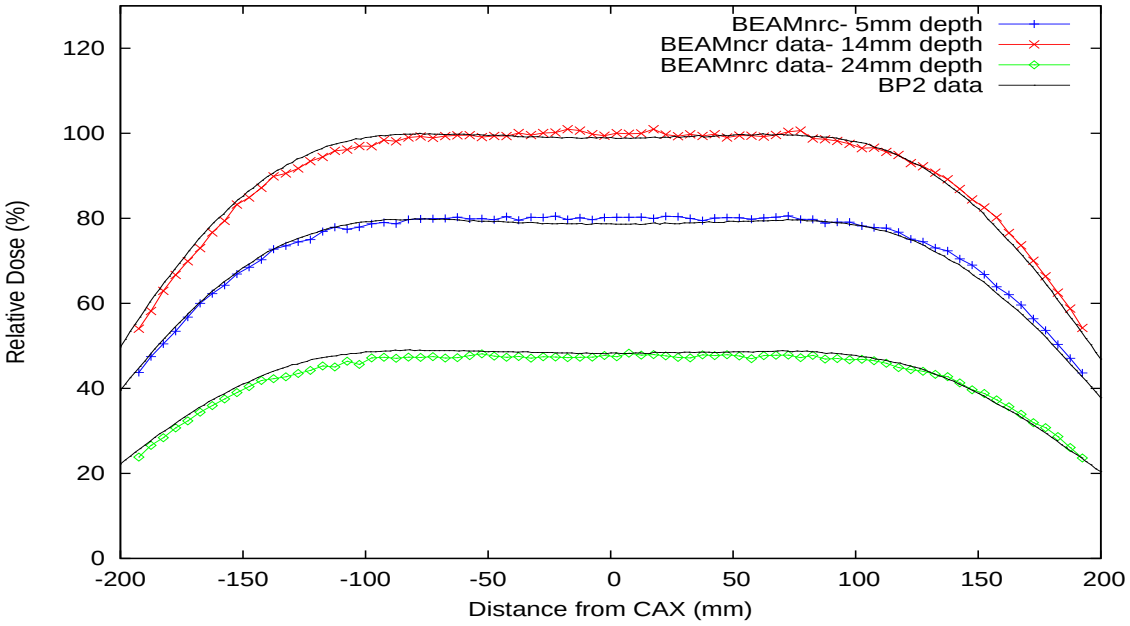

Figure 4.5: Verification of the final beam parameters for an BEAMnrc MC simulation (coloured) of a Siemens Artiste Linac compared to water phantom measurements (black) of a 6 MeV electron beam with no electron applicator attached at 100 cm SSD.

4.2.2 Final Simulation Results

The final simulation of all the other beams were modeled using the final parameters tabulated in section 4.1. Five hundred million (5×10^8) histories were used in the final BEAMnrc simulations for all energies, resulting in calculation times of between 8 and 17 hours. The difference in calculation time depended on the initial energy of the beam, as well as the electron applicator size. On average, each phase space file contained 90 million particles, of these particles, 47-78 % were low energy photon contamination. The ratio of electrons to photons decreased as the energy increased. The increase in low energy photon contamination with increasing energy is most likely due to the increase in bremsstrahlung interaction cross section as the average electron energy increases, as well as the electrons possessing enough energy to undergo many more bremsstrahlung interactions. In all simulations the statistical uncertainty in the phase space file was below 0.2 % for electrons and below 0.03 % for photons over the scoring plane.

The DOSXYZnrc phantom as described in section 4.1 was then used to obtain PDD and profile data for the simulation. Two hundred million (2×10^8) histories were used in the dose calculations. The particle recycling rate was adjusted, depending on the number of particles available in each phase space, so the counting statistics remain valid. All DOSXYZnrc calculation voxels within the beam had an averaged dose uncertainty of less than 0.5 %.

All available electron applicator sizes were modeled for the 6 MeV energy electron beam. The higher energy electron beams were only modeled with a 10×10 cm applicator, as the higher energy beams are not often used for treatments utilising internal shielding due to their penetrating power. Hence modeling all sizes is

somewhat redundant from a clinical point of view. The higher energy beams were included for completeness.

6 MeV PDD curves for all applicator sizes were verified against physical measurements, however, due to the similarities only the PDD curve for a 10×10 cm applicator are reproduced here. PDD curves for the other energies were also calculated. Several profiles at different depths for each applicator size and energy were calculated and used to verify the beam profile with depth against the physical measurements. The final results are presented in the next section.

Depth Dose Curves

Comparisons of measured and calculated central axis percentage depth dose curves are presented in Figures 4.6, 4.7, 4.8, and 4.9 for 6, 9, 12, and 15 MeV electron beams receptively.

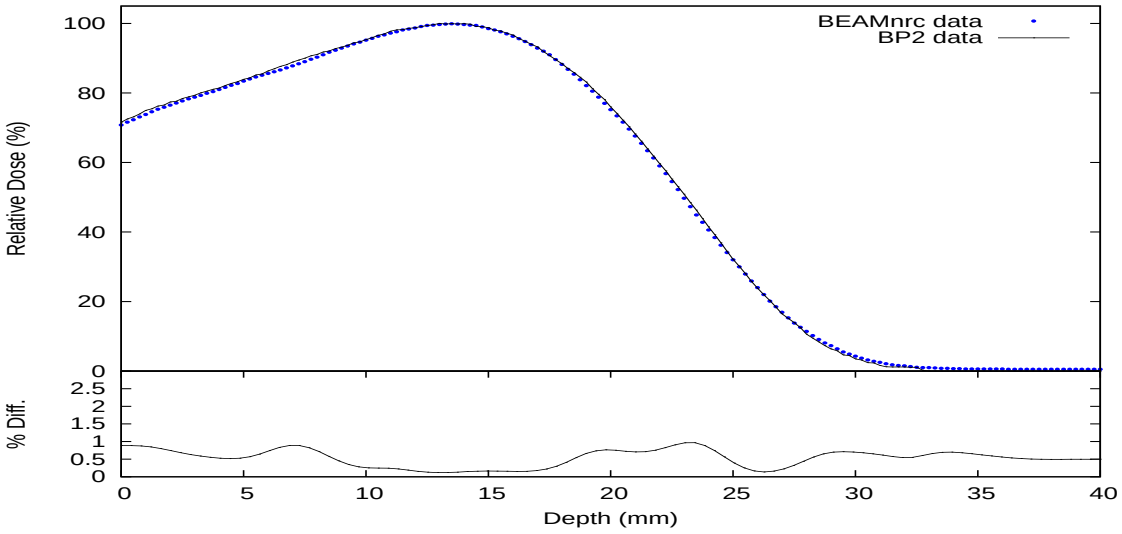

Figure 4.6: Percentage depth dose curves comparison and percent difference between a BEAMnrc MC simulation (blue) and a water phantom measurement (black) for a 6 MeV electron beam from a Siemens Artiste Linac with 10 cm square electron applicator attached at 100 cm source to surface distance.

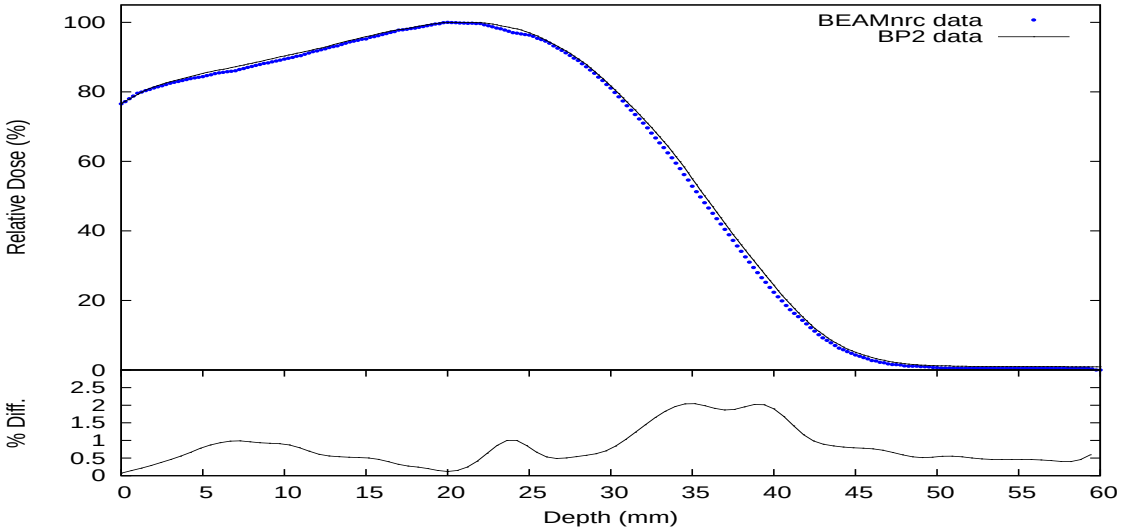

Figure 4.7: Percentage depth dose curve comparisons and percent difference between a BEAMnrc MC simulation (blue) and a water phantom measurement (black) for a 9 MeV electron beam from a Siemens Artiste Linac with 10 cm square electron applicator attached at 100 cm source to surface distance.

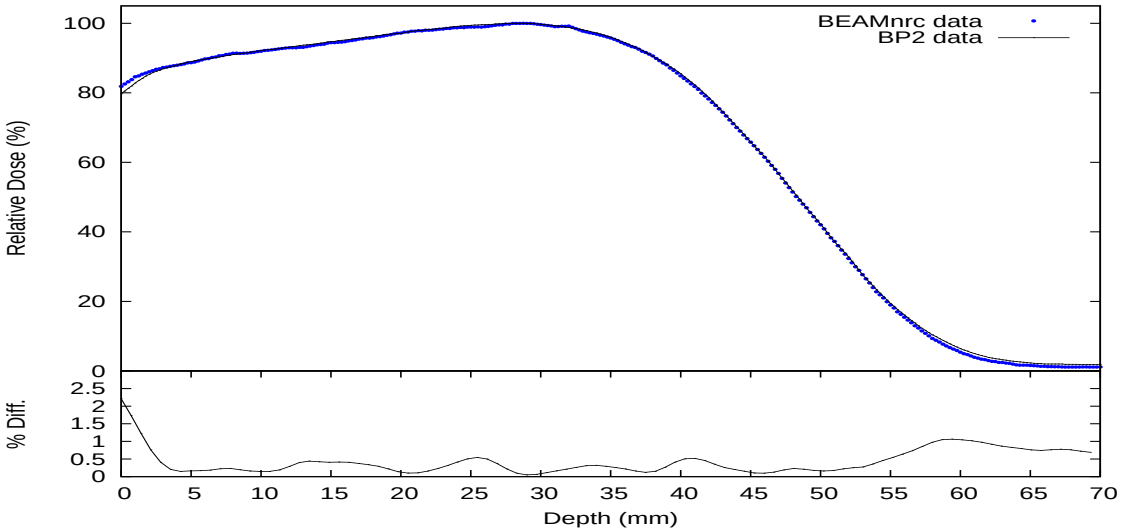

Figure 4.8: Percentage depth dose curve comparisons and percent difference between a BEAMnrc MC simulation (blue) and a water phantom measurement (black) for a 12 MeV electron beam from a Siemens Artiste Linac with 10 cm square electron applicator attached at 100 cm source to surface distance.

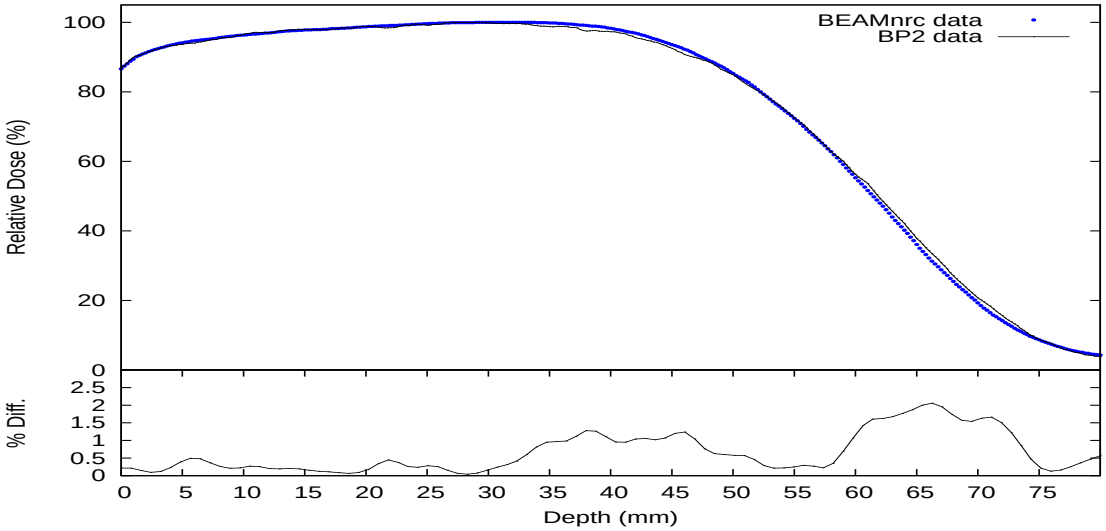

Figure 4.9: Percentage depth dose curve comparisons and percent difference between a BEAMnrc MC simulation (blue) and a water phantom measurement (black) for a 15 MeV electron beam from a Siemens Artiste Linac with 10 cm square electron applicator attached at 100 cm source to surface distance.

The agreement between the measured and BEAMnrc MC depth dose curves is excellent. The largest error (2 %) was located at some depth, well past the depth that is of interest in this study. The differences in the PDD curves conclude that there are only minor differences between the physical and simulated electron energy spectrums. This result gives confidence in the BEAMnrc MC simulation and the spectrum used.

Electron beam parameters

Energy	Parameter	Measured	Variance	BEAMnrc	Uncertainty	Difference
6 MeV	$R_{100}(mm)$	14.03	0.002	13.70	0.78 %	0.32 mm
	$R_{80}(mm)$	20.0	0.083	19.71	0.50 %	0.32 mm
	$R_{50}(mm)$	23.78	0.016	23.30	0.50 %	0.48 mm
	$R_p(mm)$	29.38	0.023	28.97	0.50 %	0.41 mm
	$R_q(mm)$	18.13	0.049	17.63	0.50 %	0.50 mm
	$D_s(\%)$	72.1	0.420	72.17	0.40 %	0.09 %
	$D_x(\%)$	0.10	0.001	0.29	0.40 %	97.07 %
	G	2.60	0.001	2.56	0.50 %	1.84 %
	$E_p0(MeV)$	6.08	0.001	5.98	0.50 %	1.68 %
	$E(MeV)$	5.53	0.002	5.43	0.50 %	1.81 %
9 MeV	$R_{100}(mm)$	20.95	0.810	21.37	1.26 %	0.42 mm
	$R_{80}(mm)$	30.93	0.003	30.80	0.53 %	0.13 mm
	$R_{50}(mm)$	36.22	0.0029	36.02	0.63 %	0.21 mm
	$R_p(mm)$	43.93	0.049	43.91	0.60 %	0.02 mm
	$R_q(mm)$	28.30	0.020	28.13	0.60 %	0.17 mm
	$D_s(\%)$	79.10	4.613	78.17	2.07 %	1.19 %
	$D_x(\%)$	0.40	0.002	0.94	2.07 %	80.52 %
	G	2.81	0.002	2.78	0.60 %	0.12 %
	$E_p0(MeV)$	8.97	0.002	8.96	0.60 %	0.12 %
	$E(MeV)$	8.44	0.002	8.39	0.60 %	0.51 %

Table 4.3: Table of measured and BEAMnrc MC calculated electron beam parameters for 6 and 9 MeV electron beams with a 10×10 cm applicator. Explanation of these parameters is given in Chapter 3.

Tables 4.3 and 4.4 shows the BEAMnrc MC and physically measured beam parameters for a 10×10 cm applicator for all electron energies modeled. Column 1 and 2 outline the energy and parameters for each row. The physical measured parameters are shown in column 3 and the MC calculated parameters are shown in column 5. The average difference between the physical parameters measured from several Artiste machines is shown in column 4. Column 6 shows the estimated uncertainty in the calculated parameters obtained from a combination of the voxel uncertainties in the DOSXYZnrc

calculation and methods used to obtain the parameters. The final column shows the percentage difference between the physical machines and the model.

Energy	Parameter	Measured	Variance	BEAMnrc	Uncertainty	Difference
12 MeV	$R_{100}(mm)$	28.33	0.289	29.17	0.50 %	0.84 mm
	$R_{80}(mm)$	41.40	0.027	41.78	0.60 %	0.38 mm
	$R_{50}(mm)$	46.53	12.622	48.49	0.60 %	1.97 mm
	$R_p(mm)$	58.13	0.029	58.89	0.70 %	0.77 mm
	$R_q(mm)$	38.00	0.060	38.09	0.70 %	0.09 mm
	$D_s(\%)$	82.93	0.183	84.20	3.49 %	1.52 %
	$D_x(\%)$	0.90	0.002	1.45	3.49 %	46.99 %
	G	2.89	0.001	2.83	0.70 %	2.04 %
	$E_p0(MeV)$	11.81	0.001	11.97	0.70 %	1.33 %
	$E(MeV)$	11.24	0.001	11.30	0.70 %	0.50 %
15 MeV	$R_{100}(mm)$	31.05	0.729	32.49	0.64 %	1.44 mm
	$R_{80}(mm)$	52.75	0.143	52.82	0.50 %	0.07 mm
	$R_{50}(mm)$	61.95	0.090	62.01	0.50 %	0.06 mm
	$R_p(mm)$	74.85	0.310	76.07	0.80 %	1.22 mm
	$R_q(mm)$	48.23	0.202	47.95	0.80 %	0.27 mm
	$D_s(\%)$	87.58	0.229	88.85	3.30 %	1.45 %
	$D_x(\%)$	1.60	0.002	3.48	3.30 %	74.03 %
	G	2.81	0.004	2.71	3.30 %	3.79 %
	$E_p0(MeV)$	15.19	0.012	15.43	0.80 %	1.56 %
	$E(MeV)$	14.43	0.005	14.45	0.80 %	0.11 %

Table 4.4: Table of measured and BEAMnrc MC calculated electron beam parameters for 12 and 15 MeV electron beams with a 10×10 cm applicator. Explanation of these parameters is given in Chapter 3.

The results in Tables 4.3 and 4.4 confirm that all of the parameters agree with the physically measured parameters to within the Van Dyke criterion of 2 %2 mm, with the exception of the bremsstrahlung tail dose. The model predicts on average a 70 % higher bremsstrahlung tail than the physical measurements. 70 % higher tail dose is high, but the absolute difference is small. This could be due to the optimisation in the range rejection in the upper treatment head resulting in less photon production

in the treatment head. The uncertainties for each parameter calculated were in most cases of the same order of magnitude as the difference between the various Artiste machines.

Beam Profiles

The following figures show comparisons between measured and calculated beam profiles from the BEAMnrc MC model. Beam profile comparisons of a 6 MeV electron beam with applicators sizes of 5, 10, 15, and 20 cm are presented in Figures 4.10, 4.11, 4.12, and 4.13 respectively. Beam profile comparisons for energies of 9, 12, and 15 MeV, with a 10 cm electron applicator are presented in Figures 4.14, 4.15, and 4.16 respectively. All scans were normalised to d_{max} along the central axis for the corresponding applicator size and energy.

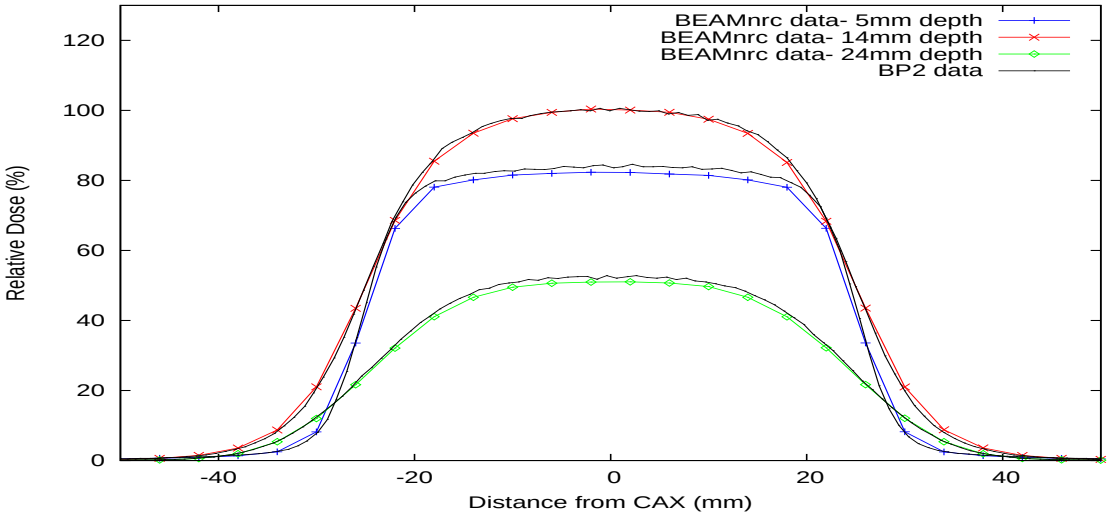

Figure 4.10: Beam profiles in water at different depths for BEAMnrc Monte Carlo simulations (coloured) and water phantom measurements (black) of a Siemens Artiste Linac 6 MeV electron beam with a 5 cm diameter circular electron applicator attached with 100 cm source to surface distance.

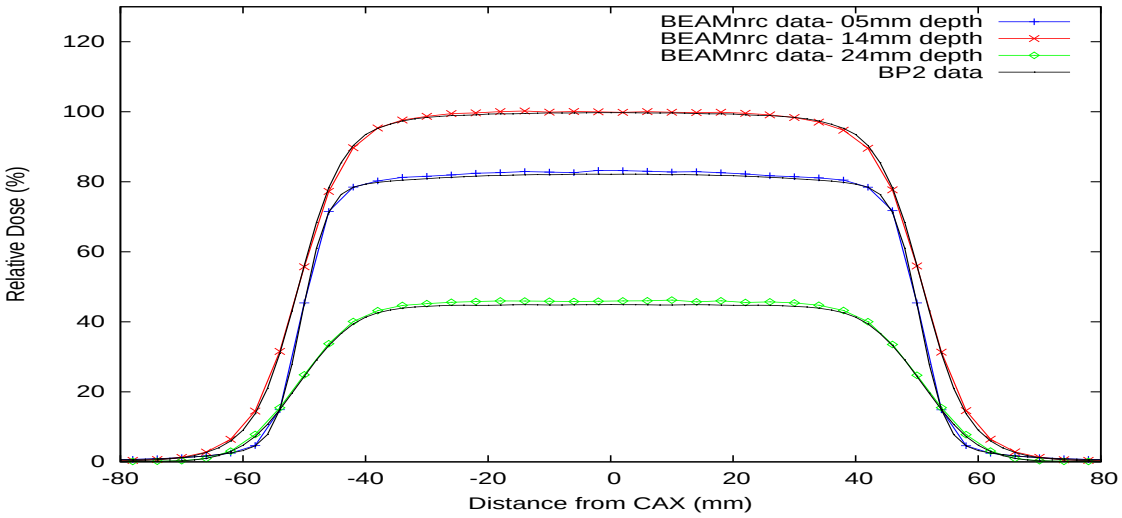

Figure 4.11: Beam profiles in water at different depths for BEAMnrc Monte Carlo simulations (coloured) and water phantom measurements (black) of a Siemens Artiste Linac 6 MeV electron beam with a 10 cm rectangular electron applicator attached with 100 cm source to surface distance.

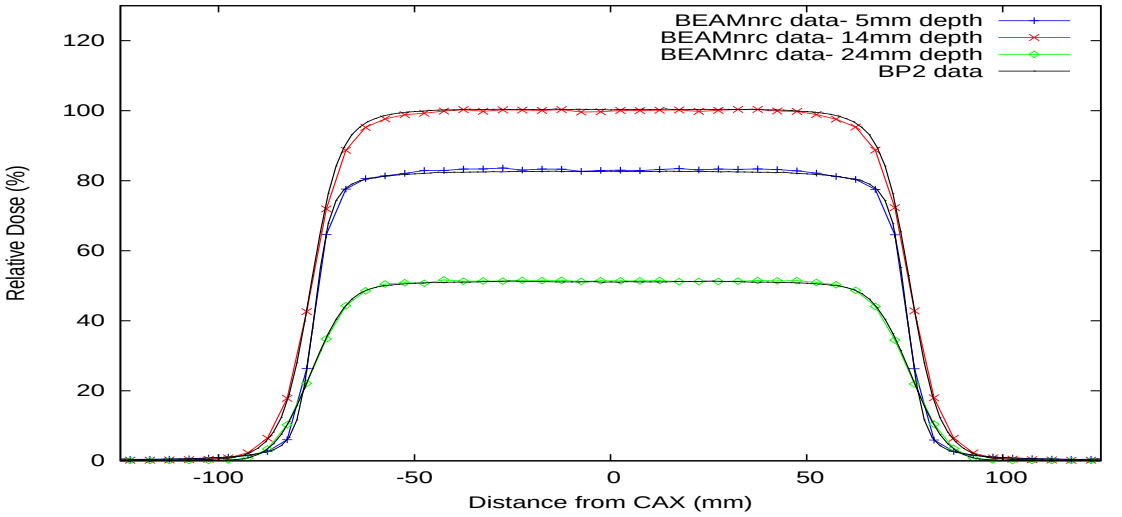

Figure 4.12: Beam profiles in water at different depths for BEAMnrc Monte Carlo simulations (coloured) and water phantom measurements (black) of a Siemens Artiste Linac 6 MeV electron beam with a 15 cm rectangular electron applicator attached with 100 cm source to surface distance.

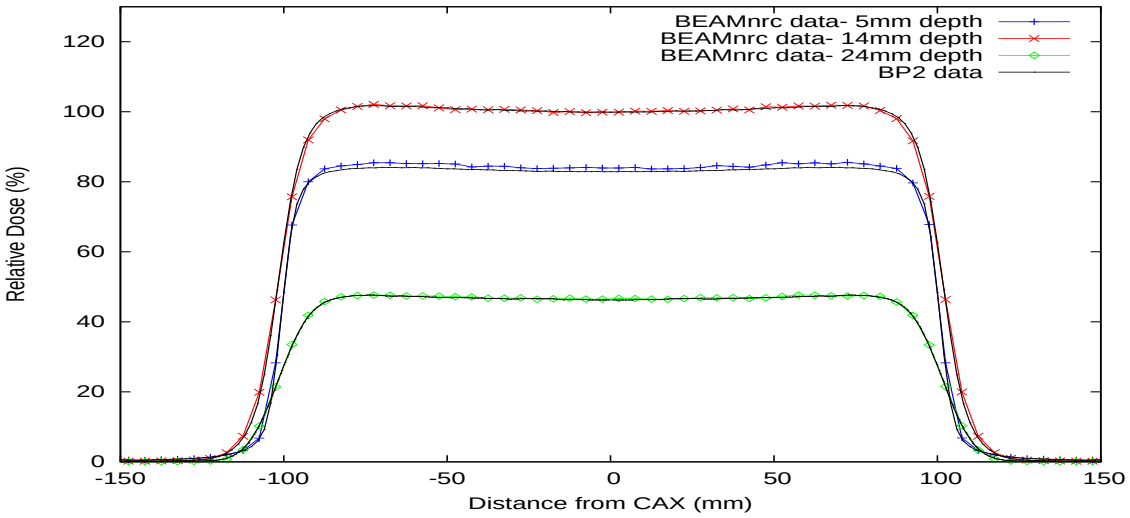

Figure 4.13: Beam profiles in water at different depths for BEAMnrc Monte Carlo simulations (coloured) and water phantom measurements (black) of a Siemens Artiste Linac 6 MeV electron beam with a 20 cm rectangular electron applicator at a 100 cm source to surface distance.

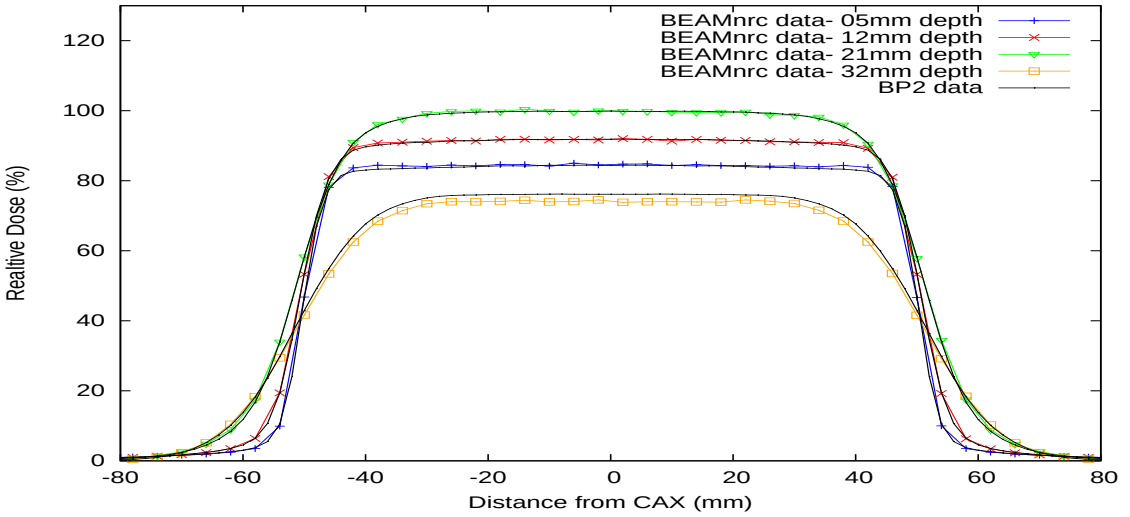

Figure 4.14: Beam profiles in water at different depths for BEAMnrc Monte Carlo simulations (coloured) and water phantom measurements (black) of a Siemens Artiste Linac 9 MeV electron beam with a 10 cm rectangular electron applicator at a 100 cm source to surface distance.

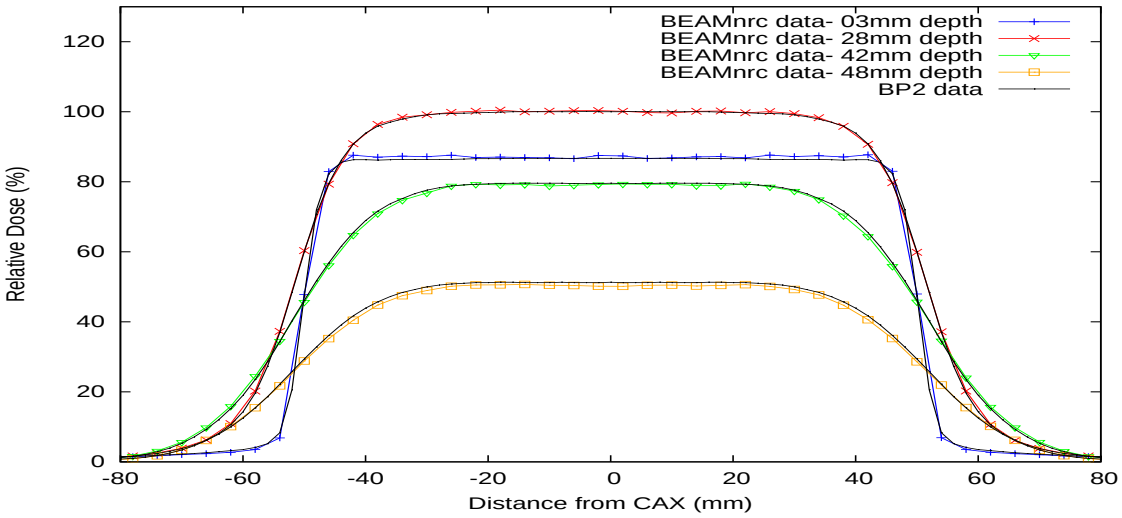

Figure 4.15: Beam profiles in water at different depths for BEAMnrc Monte Carlo simulations (coloured) and water phantom measurements (black) of a Siemens Artiste Linac 12 MeV electron beam with a 10 cm rectangular electron applicator attached with 100 cm source to surface distance.

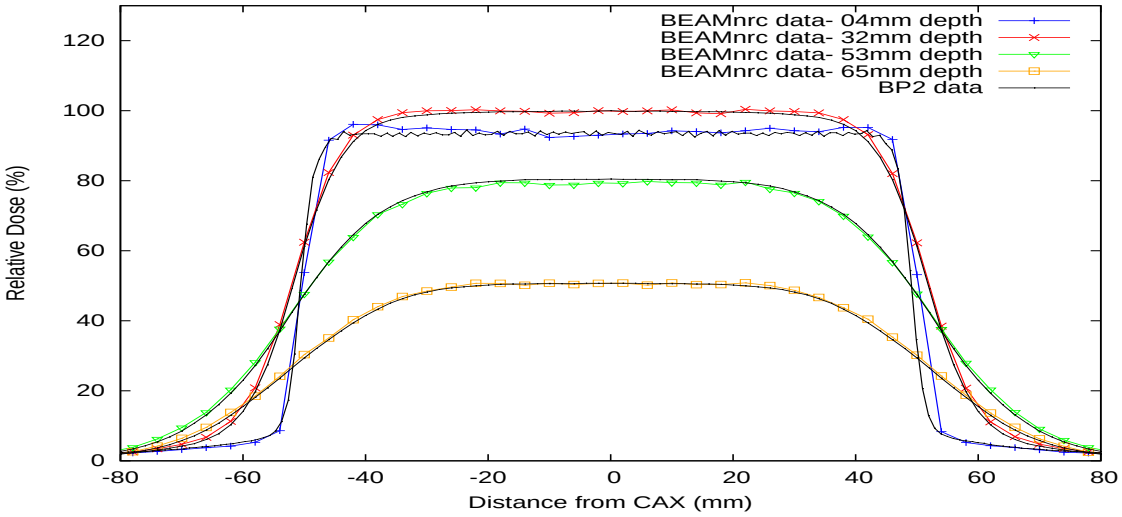

Figure 4.16: Beam profiles in water at different depths for BEAMnrc Monte Carlo simulations (coloured) and water phantom measurements (black) of a Siemens Artiste Linac 15 MeV electron beam with a 10 cm rectangular electron applicator attached with 100 cm source to surface distance.

The BEAMnrc simulation beam profiles showed excellent agreement to the measured results for all electron beam energies and applicator sizes for multiple depths and field sizes. The agreement of the beam penumbra was good. Several of the profiles do show a small degree of statistical noise, however, all simulated beam profiles easily surpass the Van Dyke criterion.

Isodose Maps

Figure 4.17 shows isodose comparisons between the BEAMnrc MC simulation(dashed lines) and XiO calculated dose distributions (solid lines) for all energy electron beams for the Siemens Artiste Linac for a $10 \times 10\,\text{cm}$ electron field size. All data were normalised to d_{max} on the central axis for a $10 \times 10\,\text{cm}$ applicator and respective energy. Isodose maps calculated from physical data were possible but comparisons were not made due to software export limitations.

Overall, the match of the isodose curves was excellent, with the exception of certain peripheral areas with low dose. The peripheral areas are areas where few primary electron histories in the simulation will reach during a simulation and hence are more prone to statistical noise. The isodose plot for 12 MeV showed a large difference in the bremsstrahlung tail dose, with XiO eMC estimating a higher dose than the BEAMnrc simulation possibly due to the implementation of the variance reduction technique described in section 3.3.1, however, the bremsstrahlung tail dose for all other energies show excellent agreement.

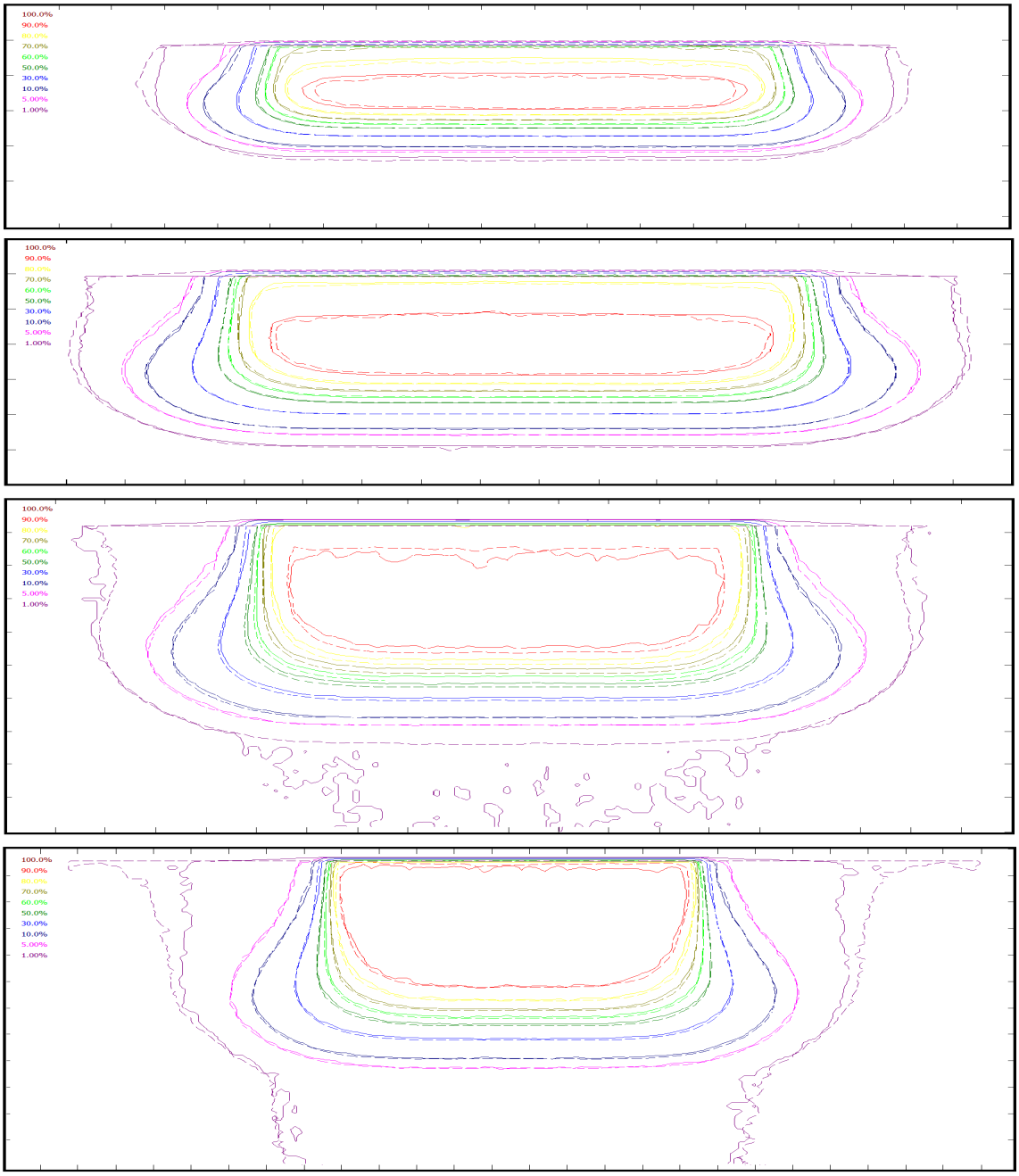

Figure 4.17: Isodose distributions in water for a BEAMnrc Monte Carlo simulation (dashed line) and XiO eMC (solid line) treatment planning algorithm for 6, 9, 12, and 15 MeV electron beams with 10 cm rectangular electron applicator attached at 100 cm source to surface distance.

4.3 Discussion

The need to use an energy spectrum and angular divergence of the initial electron beam to obtain a model which agrees with the physical measurements obtained for both PDDs and beam profiles was unexpected. Little mention is made in the literature regarding the need to use an energy spectrum, rather, a mono-energetic initial electron beam is often used to develop a model of similar accuracy.

The use of an initial mono-energetic beam may be acceptable in most situations or for modeling other vendor's Linacs, however, acceptable results could not be achieved here using this assumption. It is unreasonable to think that the initial energy of electrons emerging from the vacuum window to be completely mono-energetic. There will always be some energy spread present, but if the energy spread is small enough it may be reasonable to use a mono-energetic initial electron beam. The energy spreads of the initial electron beams used here are shown in Figure 4.18 and were modeled as Gaussian distributions. The spread in the Gaussian distribution shows that there is either a substantial spread in electron energies after they pass through the bending magnet, or that some components in the treatment head model are incorrect. Considering the bending magnet system employed, it is highly possible that a physically larger spread of initial electron energies does exist, however, the bending magnet system employed does not account for the beam divergence needed to match beam profiles. The bending magnet system is designed to minimise the beam divergence, as discussed in 2.2.1. Increasing the divergence of the initial beam to achieve acceptable results has been mentioned in several studies which focus on large electron field sizes.

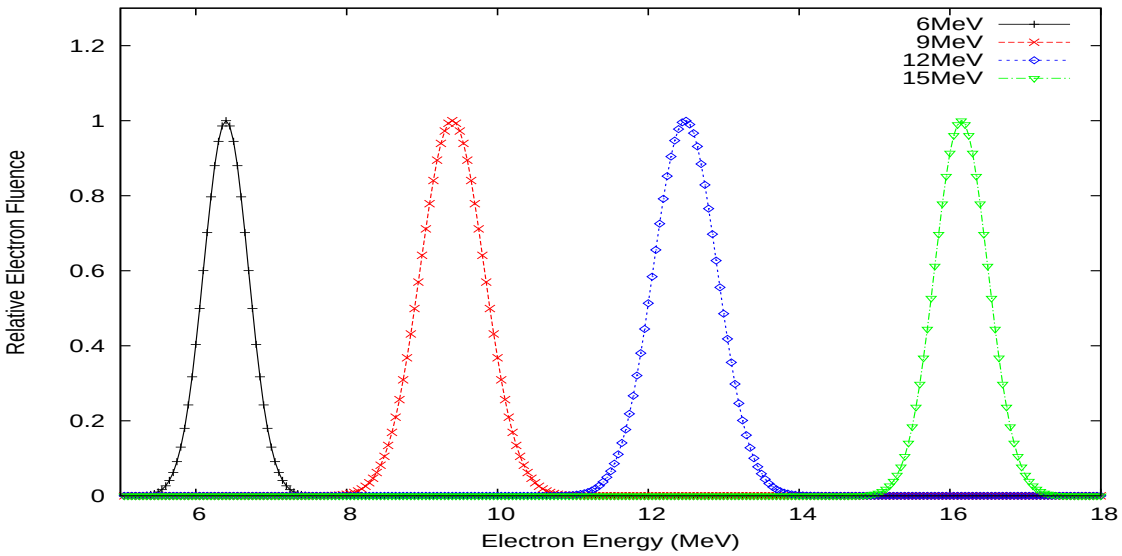

Figure 4.18: Graph of the energy distribution of the electrons in the initial electron beam used in the BEAMnrc MC Linac simulation of a Siemens Artiste for 6 (black), 9 (red), 12 (blue), and 15 (green) MeV electron beams.

4.4 Conclusion

The MC code BEAMnrc was used to develop a model of a Siemens Artiste Linac treatment head and associated electron applicators. A number of different field sizes were simulated for a 6 MeV electron beam, whereas the higher energy electron beams of 9, 12, and 15 MeV were only simulated with a single field size of 10 cm. The resulting phase space files scored from the simulations were used with the dose calculation code DOSXYZnrc to estimate percent depth dose curves, beam profiles and dose distributions. The results from the BEAMnrc simulation were compared to physical measurements as well as dose estimations from XiO's eMC algorithm and showed excellent agreement for all energies and field sizes investigated.

Different electron depth dose parameters were also calculated to further assess

the accuracy of the simulation. All the parameters agree within the accuracy sought of 2 % 2 mm for all energies, with the exception of the gradient and bremsstrahlung tail dose. Many of the simulation parameters agreed to within sub-percent levels to the measured parameters. Depth dose parameter agreement, as well as the agreement between the profiles, PDDs, and isodose distributions give confidence that the electron spectrum at the isocenter for the simulation is close to the physical electron beam spectrum. This allows the model to be used to investigate electron backscatter, as electron backscatter is very sensitive to the electron spectrum involved.

Chapter 5

Dose Distributions in the Presences of Lead

The BEAMnrc MC simulation of a Siemens Artiste was developed and verified in Chapter 4. The results of which show that the model was able to accurately predict the relative output in a simple water phantom for all energies modeled. The relative dose distributions predicted by this model agreed well with XiO's eMC algorithm. Hence, the model can be used to investigate dose distributions involving high density materials. The results of which can be compared to XiO's eMC predicted dose and physical dose measurements, specifically focusing on the contribution of dose from backscattered electrons from a lead interface. Such situations are found in treatments which benefit from internal shielding, as outlined in the introduction (section 1.4).

This chapter outlines the methods used to simulate internal shielding situations and measurements. Dose distributions and EBF values are calculated from the results. Comparisons between XiO eMC, the BEAMnrc MC model, and film measurements

will be made. The intention of which is to determine XiO's ability to estimate the EBF and corresponding dose distributions from internal shielding. This will allow the optimisation of the future outcome for radiotherapy patients who may benefit from the use of internal shielding.

5.1 Methods and Materials

A three-way comparison was performed between XiO, the BEAMnrc MC model, and physical measurements. A simple measurement geometry was chosen that loosely represents the placement of lead shielding at the therapeutic depth within tissue. A 10 × 10 cm electron field was used for all energies at a standard distance of 100 cm SSD. The therapeutic depth at which the lead was placed corresponded to a depth of 20, 30, 40, and 52 mm for electron beams with energies of 6, 9, 12, and 15 MeV respectively.

To be able to directly compare the different predicted dose distributions and measurements from all three methods they must all be performed in a comparable geometry. The measurements were performed on a simple rectilinear geometry phantom, rather than in a more realistic patient phantom. Results from such a phantom will focus on EBF and upstream dose caused by the lead interface and avoid the influence of other complex electron effects on the results, such as dose estimation under conditions of rapidly sloping surfaces.

The phantom consists of a large body of water in which a slab of lead was placed horizontally, which shielded one half of the beam. The phantom is schematically shown in Figure 5.1. The lead was chosen only to cover one half of the field as this

allows the measurement of a regular PDD and a measurement of a PDD that contain electron backscatter from an otherwise identical measurement geometry. A peace of 2 mm thick lead shielding was used. This thickness was chosen as it is often used in clinical practice and is readily available.

The measurement plane for all three methods is shown in Figure 5.1 as the dashed line. The calculation volume for XiO eMC and the BEAMnrc MC model is shown as the bold cube. PDD measurements were obtained from line A and B respectively. The EBF value was calculated as the ratio of the dose at the lead-water interfaces and the equivalent depth on the regular PDD.

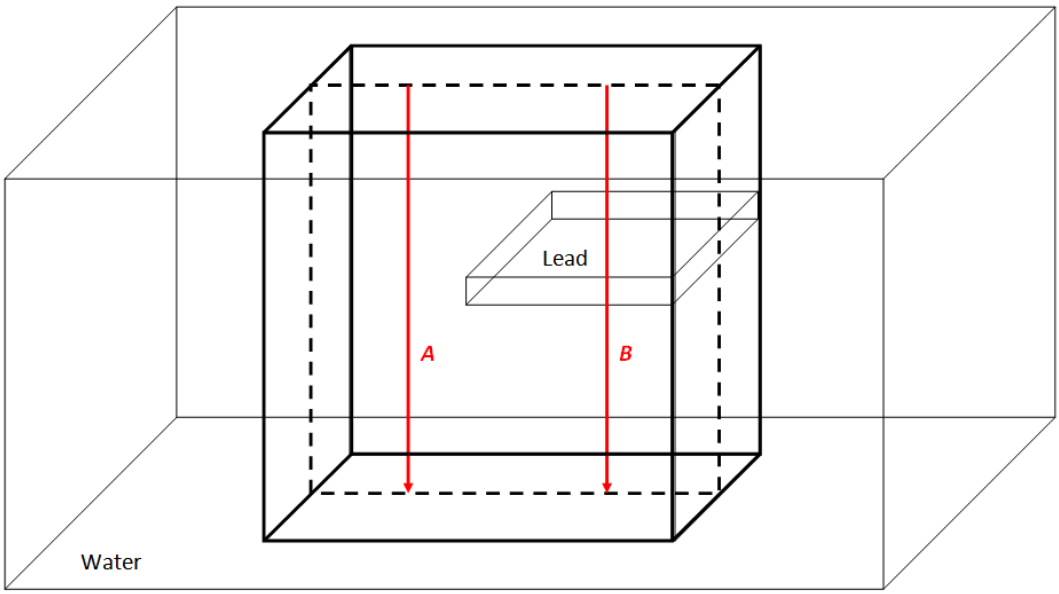

Figure 5.1: Schematic of the phantom used to measure simulated electron backscatter factors and upstream dose from several clinical electron beams. Consisting of water in which lead shielding is placed at desired depths. The figure shows the BEAMnrc MC and XiO eMC calculation volume(bold cube) as well as the film plane(dashed line) surrounded by water. This configuration allows the calculation/measurement of regular PDD curve (arrow A) as well as a PPD curve through lead (arrow B) to be measured at the same time.

5.1.1 Physical Backscatter Measurements

Physical measurements were made using Gafchromic EBT2 film (Lot # A10061001B, ISP, Wayne, USA). Gafchromic film was chosen as the ideal measurement device as it enables a 2D dose plane to be easily obtained. Gafchromic film can also be cut into any shape required as long as the orientation in respect to the original sheet is noted. The film is also water proof and is nearly water equivalent with an effective atomic number of 6.98(49)(the effective atomic number of water is 7.30(50)). This allows the film to be submerged into a water phantom. It has also been shown that Gafchromic film has little energy dependence in both photon and electron beams and does not show any dose rate dependence in electron beams(50). This is ideal for electron beams where the mean electron energy changes with depth.

Film Calibration

The Gafchromic film's dose response was first calibrated. Although it has been reported that EBT2 film has little energy dependence, a calibration for all electron energies under investigation was performed. Gafchromic film calibration for each electron energy was at a depth of at least d_{max} inside a plastic water phantom. An ion chamber measurement was performed at the same position to measure the dose delivered to the film. The measurement films were cut to sizes of 20 by 20 mm with their orientation clearly labeled. It has been shown that there is no increase in uncertainty when EBT2 film is cut to this dimension(49). The region of interest used for analysis was a 10 mm central square to avoid possible edge artifacts. The scanning direction of all the film was in the landscape direction of the original film, this is to avoid any polarizing artifacts on the pixel value read out of the film. All

films were scanned twice at the center of the scanning bed to maintain a constant scanner response for each film.

The film scanner used was an Epson Perfection V700 scanner operated in professional mode. The scans were performed as transmission scans with all image enhancements switched off, and at a resolution of 75 DPI. The images were saved as 48 bit RGB tagged image file format (TIFF). Prior to scanning, the scanners light source was allowed adequate time to warm up. Post exposure darkening of EBT2 film has been reported(49), therefore each peace of film was allowed 48 hours after irradiation to stabilise. The pixel value was read from the two scans and averaged using the red channel.

The calibration results are shown in Figure 5.2 for all energies. The results confirm that Gafchromic film has little energy dependence in the energy range of 6 to 15 MeV for electron beams. A dose response curve was calculated over the entire electron energy range from these results. The absolute percent difference between the measurement points and the curve was calculated. The percentage difference was on average 0.8 %. This curve was used in later measurements to convert from optical density to dose.

Film Measurements

The film measurements were made in a custom water phantom, aptly named Hiro's bucket phantom, which mimics the schematic in Figure 5.1. A jig accommodates the lead shielding and a piece of Gafchromic film. The depth of lead shielding was altered by altering the water level inside the bucket. The source to surface distance (SSD) was kept constant at 100 cm. This phantom allows the electrons to incident directly

onto the water's surface. The phantom and jig are shown in Figure 5.3.

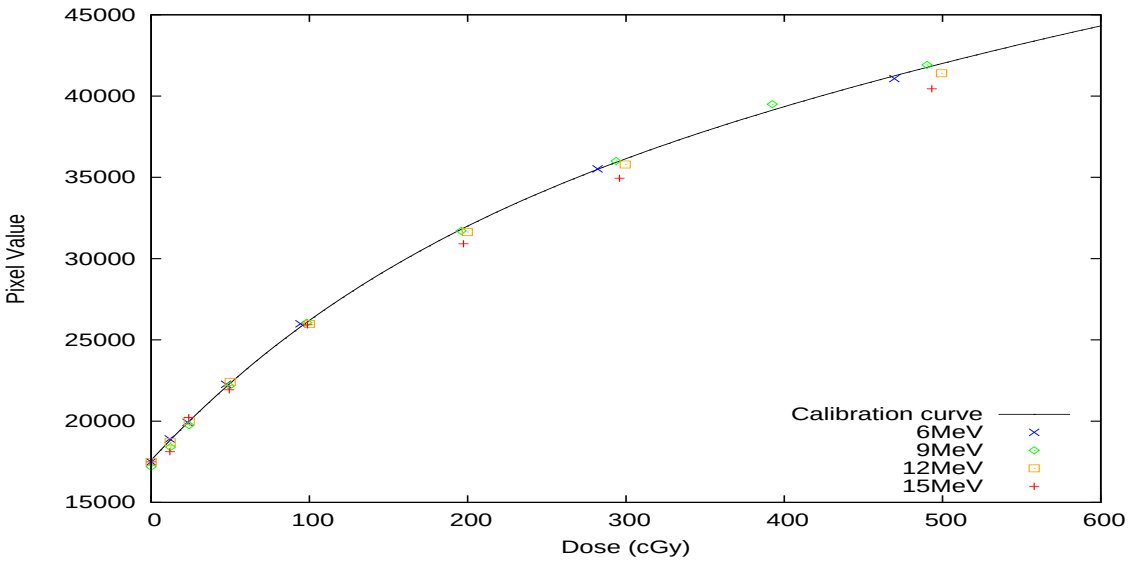

Figure 5.2: Optical density versus dose curve for EBT2 Gafchromic film for electron beam energies of 6, 9, 12, and 15 MeV. A calibration curve calculated from the average of each energy is also plotted, which was used in later measurements to convert film measurement pixel density to dose.

The measurement films were cut to a width of 15 cm, which is larger than the electron field to allow for lateral electron bulging with depth. The lead shielding was cut into two pieces to allow the placement of the film. The two pieces of lead were firmly placed against the film to minimise the gap caused by the film. The scanning procedure for the measurement film was the same as the calibration films. As the film was submerged into water the 48 hour stabilisation time allowed moisture levels to reach equilibrium before the films were scanned. The scanned film was converted to dose using the curve in Figure 5.2 and the dose plane was then exported to be compared to the other results.

Figure 5.3: Photo of experimental setup showing: Siemens Artiste Linac with electron applicator and water filled bucket (left) where a jig holding lead shielding and Gafchromic film (Right) is submerge. The depth of the lead interface is controlled by the water level in the bucket.

5.1.2 XiO Simulations

The XiO dose calculations were performed on a phantom study set defined by rectangular contours, shown in Figure 5.4. Each contours' area was assigned its own relative electron density which was then used to calculate the stopping and scattering power as described in section 3.3.2. The isocenter was set to the center of the top surface, placing the cone 5 cm from the surface at an SSD of 100 cm. An MRSU value of 0.50 % with an MRSU threshold of 50 % was used and the voxel size was

set to 1 mm cubes. The number of histories was set to the maximum available. The calculations were performed with absorbed dose to medium and the heterogeneity correction turned on. Dose planes as per Figure 5.1 for each energy were exported to be compared to the other results.

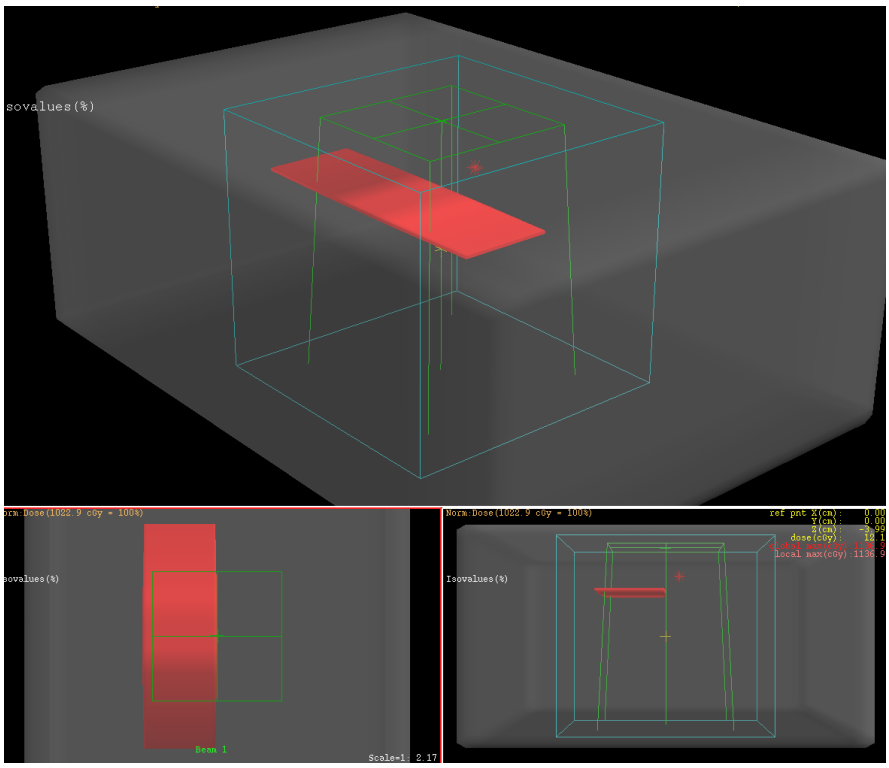

Figure 5.4: Screen shot from the treatment planning system, XiO, showing the phantom used to calculate dose distributions involving lead. The calculation volume is shown as the blue cube, the beam is represented by the green lines, and the lead is shown in red.

5.1.3 Monte Carlo Simulations

The MC simulations were performed on a phantom created in DOSXYZnrc. The phantom consisted of several planes of voxels along the $X - Z$ axes. Each voxel can independently be assigned a material composition. The central plane consisted

of 0.1 x 0.5 x 0.1 cm voxels for 6 and 9 MeV and 0.1 x 0.5 x 0.2 cm voxels for 12 and 15 MeV. Voxels were assigned as water and lead appropriately to mimic schematic 5.1. The outer surrounding planes of voxels were larger in the Y direction; these voxels were included to allow for the lead shielding to extend perpendicular to the measurement plane. This creates the correct backscatter conditions.

The phase space files from the previous simulation in Chapter 4 were used as source inputs. As these phase space files were taken at the isocenter they were positioned on the top surface of the phantom. Two hundred million histories were simulated with a recycling number of 2. The output file was then processed through the Excel macro as describe in sections 4.1. This macro rearrange the data into $X - Z$ dose planes which were then exported to be compared to XiO and film measured dose planes.

5.2 Results

5.2.1 PDD Comparisons

Percentage depth dose curves were calculated from each dose plane for all measurement sets along line A and B. The PDDs were normalised to the maximum dose value on the regular PDD curve along line A. The resulting PDD curves were compared for all the data sets and are presented in Figures 5.5, 5.6, 5.7, and 5.8 for 6, 9, 12, and 15 MeV electron beams respectively. The BEAMnrc data was chosen as the baseline results due to it being a good match to the physical machine, as shown in Chapter 4. Absolute percentage differences between the BEAMnrc compared to XiO and film data sets were also calculated and are displayed on the same figures.

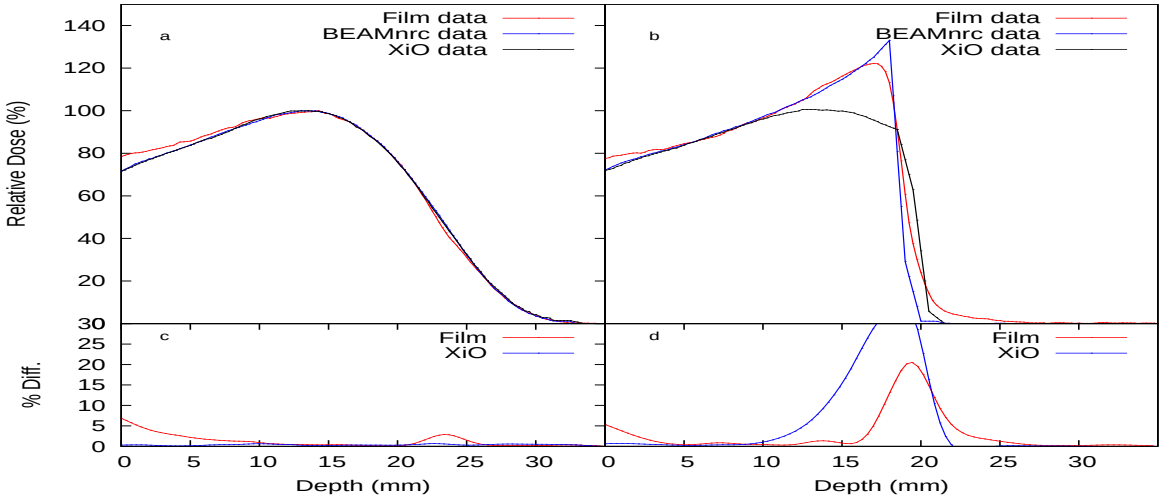

Figure 5.5: Comparison of 6 MeV electron depth dose curves, with (right column) and without (left column) lead shielding, between XiO's eMC algorithm(black), BEAMnrc MC simulation(blue) and Gafchromic film measurements(red). The lead shielding was positioned at a depth of 20 mm corresponding to the therapeutic depth for 6 MeV.

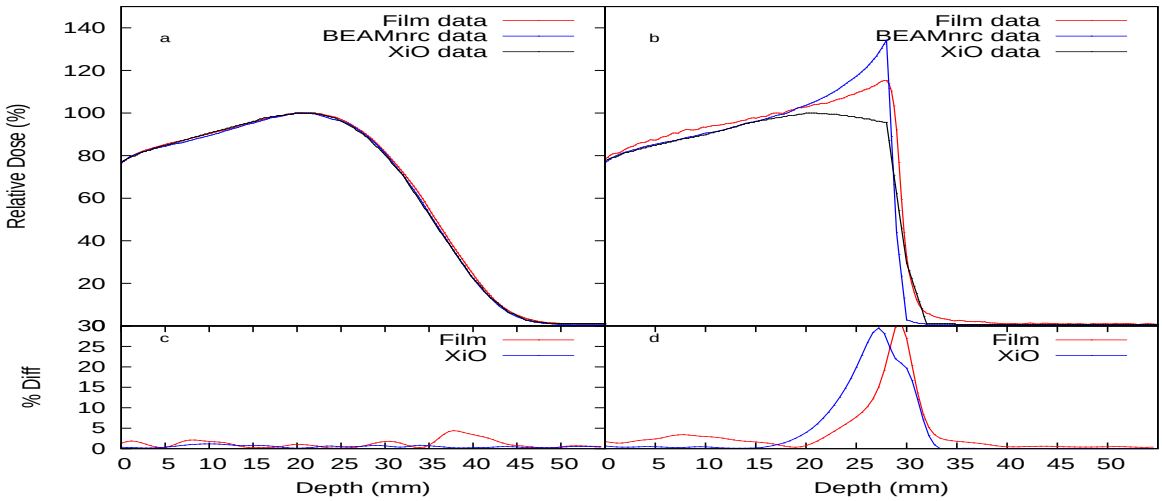

Figure 5.6: Comparison of 9 MeV electron depth dose curves, with (right column) and without (left column) lead shielding, between XiO's eMC algorithm(black), BEAMnrc MC simulation(blue) and Gafchromic film measurements(red). The lead shielding was positioned at a depth of 30 mm corresponding to the therapeutic depth for 9 MeV.

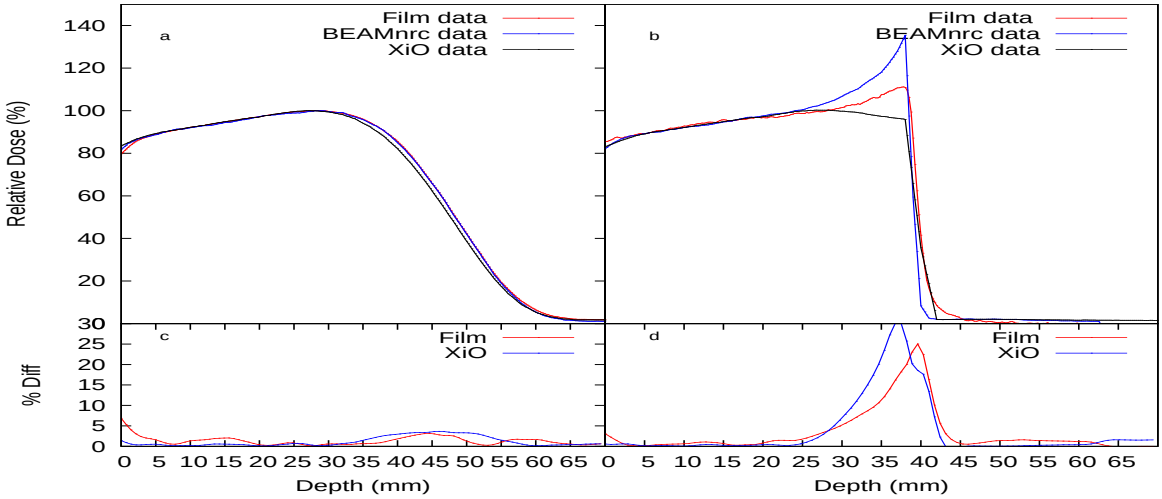

Figure 5.7: Comparison of 12 MeV electron depth dose curves, with (right column) and without (left column) lead shielding, between XiO's eMC algorithm(black), BEAMnrc MC simulation(blue) and Gafchromic film measurements(red). The lead shielding was positioned at a depth of 40 mm corresponding to the therapeutic depth for 12 MeV.

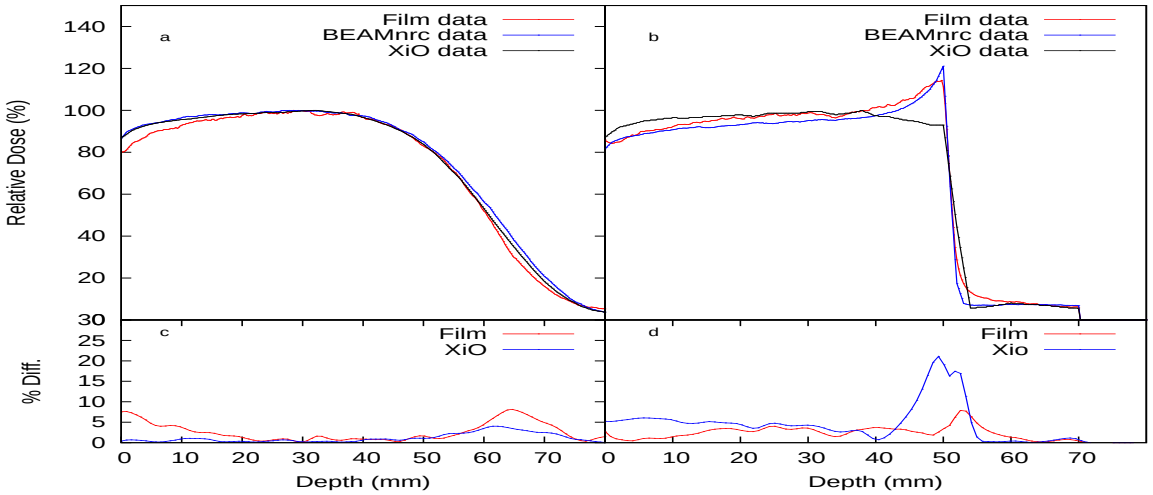

Figure 5.8: Comparison of 15 MeV electron depth dose curves, with (right column) and without (left column) lead shielding, between XiO's eMC algorithm(black), BEAMnrc MC simulation(blue) and Gafchromic film measurements(red). The lead shielding was positioned at a depth of 52 mm corresponding to the therapeutic depth for 15 MeV.

The PDD curves shown in Figures 5.5, 5.6, 5.7, and 5.8 show good agreement between the BEAMnrc MC and film measurements, however, there is a notable difference between the two in the vicinity of the lead interface. The best agreement is seen in Figure 5.8 between the 15 MeV film and the MC.

At the lead-water interface, the dose measured by the film is lower than the BEAMnrc MC predicted dose for each energy electron beam. The film measurements also display slightly higher transmission dose than both XiO's eMC and the MC calculations. XiO's eMC predicted the lowest electron backscatter for each energy.

Figure 5.9 shows the value of the calculated EBF value for each of the three calculation methods for each energy electron beam. For comparison, the EBF values estimated from Equation 1.8 are also included. The values are plotted against the mean energy of the electrons at the lead interface, estimated by Equation 1.9 and values from Tables 4.3 and 4.4

There is little agreement between any of the EBF values shown in Figure 5.9. The MC and equation predicted values agreed to within 7 % on average. The EBF values calculated from the BEAMnrc MC and the film agreed to within 14 %. XiO's values were consistently lower by 30 % than the equation's predicted EBF values and 20 % lower than the BEAMnrc simulation values, while the agreement with the film values ranged from 10 to 20 %.

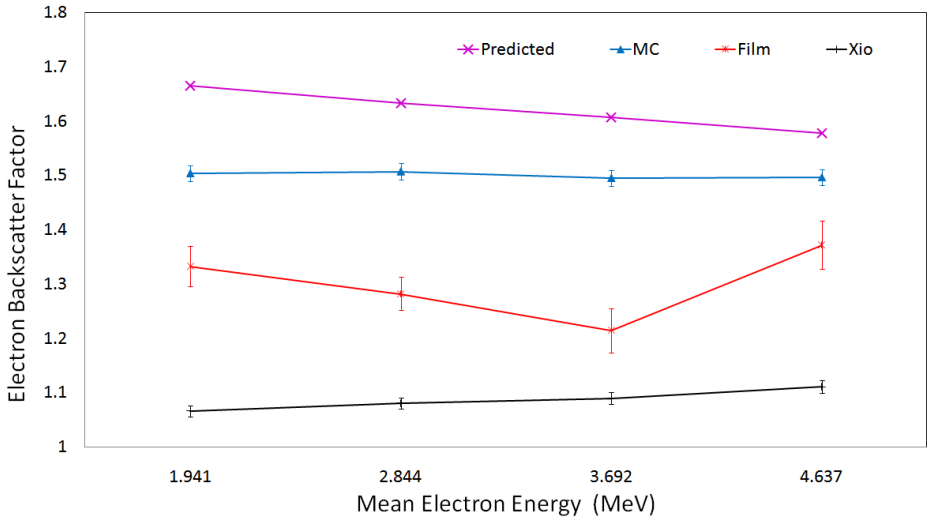

Figure 5.9: Graph comparing electron backscatter values calculated from Gafchromic film, XiO eMC, BEAMnrc MC and predicted by Equation 1.8 against the mean energy at the lead interface. Measurement depths were 20, 30, 40, and 52 mm for energies 6, 9, 12, and 15 MeV. The resulting mean energies at the lead interface were 1.941, 2.844, 3.692, and 4.637 MeV respectively.

There was no clear trend amongst the different methods either. XiO's eMC EBF values steadily increase with increasing energy. The BEAMnrc MC EBF values were roughly constant over all energies tested. This is consistent with the relationship proposed by Joseph(25), which is that the EBF value increases with energy in the region of 0.5 MeV and 1.5 MeV and then remains nearly constant up to around 3 MeV. The film's EBF values do not follow any trend; this may be due to the limitation of the experimental setup.

5.2.2 Gamma Comparisons

In certain instances it is misleading to use a strict dose point comparison to compare two different dose distributions. In these situations a gamma comparison can be

used. A gamma comparison is comprised of a combination of dose and distance agreement between two dose distributions. A commonly used dose and position criteria is 3 % in dose and 3 mm in position, however, the criteria for each can be assigned independently. One data set is assigned as the reference and compared to the second data set. A gamma value is calculated at every dose point for the reference data set to determine if a point in the second data set agrees within the dose and position criteria. Values below 1 satisfy both the dose and position criteria, while a gamma value above 1 will fail either, or both, the dose and position criteria (10).

Gamma values on the central axis plane were calculated and compared to determine the upstream agreement amongst the three data sets. The specification for the gamma test was set to the local standard of 3 % 3 mm percentage-distance to agreement, with a cut off at a dose level of 3 % of dose maximum. The BEAMnrc MC dose distribution was used as the reference data set as it showed the least amount of noise. The gamma results are shown in Figure 5.10

The gamma results in Figure 5.10 show that, for all dose distributions modeled, the agreement was better between the film measurements and BEAMnrc MC dose planes compared to the XiO eMC and BEAMnrc MC dose planes. There exists a significant difference at the lead interface between the film-BEAMnrc dose planes, especially in the lower energy beams; however, the agreement improves quickly for all electron beams in the upstream direction from the lead interface when compared to the XiO eMC-Gafchromin film results. This result was expected as it had already been observed in the PDD curves in Figures 5.5, 5.6, 5.7, and 5.8.

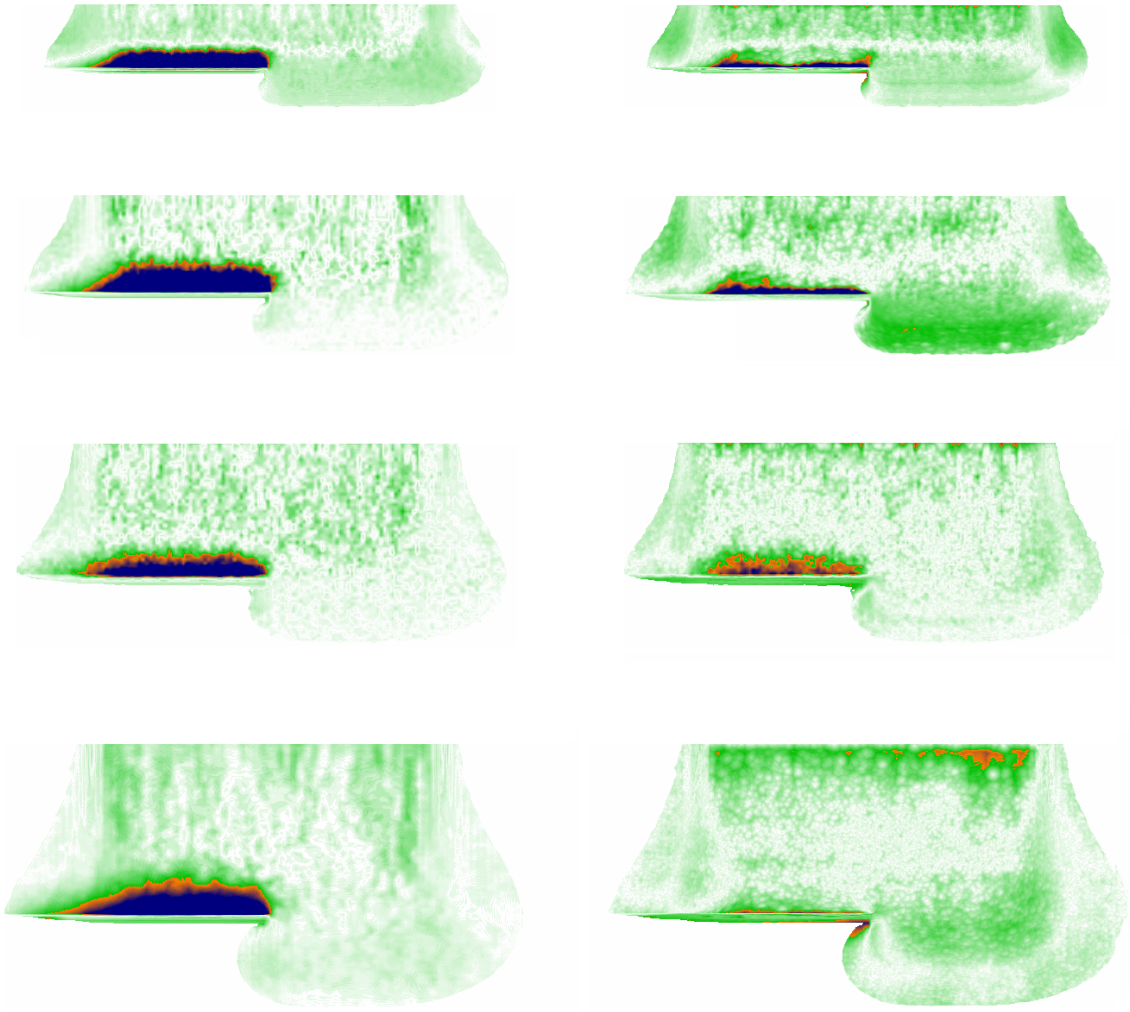

Figure 5.10: Gamma comparisons of the central $X - Z$ axis dose plane between XiO eMC and BEAMnrc MC dose distributions (left) and Gafchromic film and BEAMnrc MC (Right), for all electron beam energies examined. gamma values in the range of 0 to 1 are represented in white to green. Gamma values of 1 to 2 are represented by orange. Gamma values above 2 are represented in dark blue. The calculation was set to a percent distance agreement of 3 % 3 mm. The gamma value was calculated using the Monte Carlo results as the reference data set. From top: 6, 9, 12, and 15 MeV electron beams with lead covering one half of the beam positioned at the beam's therapeutic depth.

5.3 Discussion

5.3.1 Film Measurement Limitations

The results from the previous sections showed that the three different methods for predicting a dose plane in the vicinity of a metal tissue interface are not in full agreement with one another. Overall the film measurements agreed more closely to the BEAMnrc MC results than they do to XiO's eMC results for the majority of energies investigated.

The discrepancy between the MC and the film results could be explained by the presence of a gap in-between the lead created by the film. This gap could decrease the local electron backscatter and allow dose to be transmitted through and be deposited beyond the shielding. In theory this gap will be the thickness of the film itself, but it is most likely larger due to set up limitations. The PDD curves in Figures 5.5 to 5.8 shows exactly what would be expected if a larger gap was present, when compared to the MC results

To estimate the effect that a gap would have on the measurement results, a simulation in DOSXYZnrc was performed. The gap is far too small to simulate on XiO's eMC. The gap width was set at 300 microns in DOSXYZnrc, which corresponds to the total thickness of the film at 285 microns and allows for set up limitations. It is highly likely that the actual gap is much larger than 300 microns, but simulating the gap at this thickness will estimate the best possible physical measurement achievable using the current set up. A new material was made in the PEGS data set to accommodate the Gafchromic film in the simulation. The composition of the Gafchromic film simulated was taken to be 41 % Hydrogen, 43 %

Carbon and 16 % Oxygen(49). Several other elements are present in trace levels and were ignored as the effect of these trace elements is considered to be negligible. The resulting PDD curves through the lead with the gap included were compared to the previous BEAMnrc MC simulations without the gap, for all energy electron beams, and are shown in Figure 5.8.

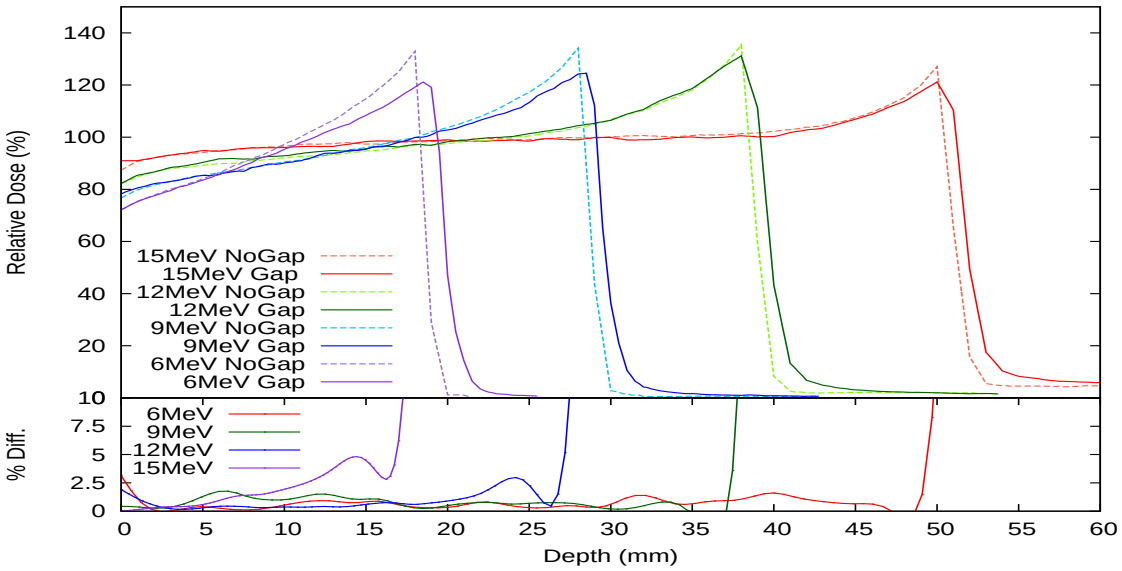

Figure 5.11: BEAMnrc MC comparison of the electron backscatter from shielding with a 300 micron gap in the lead(solid lines) vs. no gap in the lead(dashed lines). PDDs are on the central axis. This gap is present when measuring backscatter using EBT2 film as the film passes through the lead shielding, however the gap is not present in the Monte Carlo and XiO calculations.

The results from the gap simulation show that for all energy beams the EBF value decreases when the gap is considered. The decrease is more pronounced for the lower energy beams than the higher energy beams. It also shows that the amount of transmission increases significantly. This is far more pronounced than what is seen in the measurement results. The gap also decreases the amount of upstream dose

contribution for the lower energy beams, however this is not evident in the higher energy beams. This effect is again not very evident in the previous film results.

Percentage differences relative to the film results were calculated for the BEAMnrc MC results simulating the gap in the lead. The percentage differences were then compared to the percentage differences from the initial BEAMnrc MC results. This data is presented in Figure 5.12. The percentage difference between the BEAMnrc MC results with and without the gap and the film results show an overall decrease in the vicinity of the lead interface for all energy electron beams when the gap is introduced. The most significant decrease was seen in the 6 and 9 MeV results.

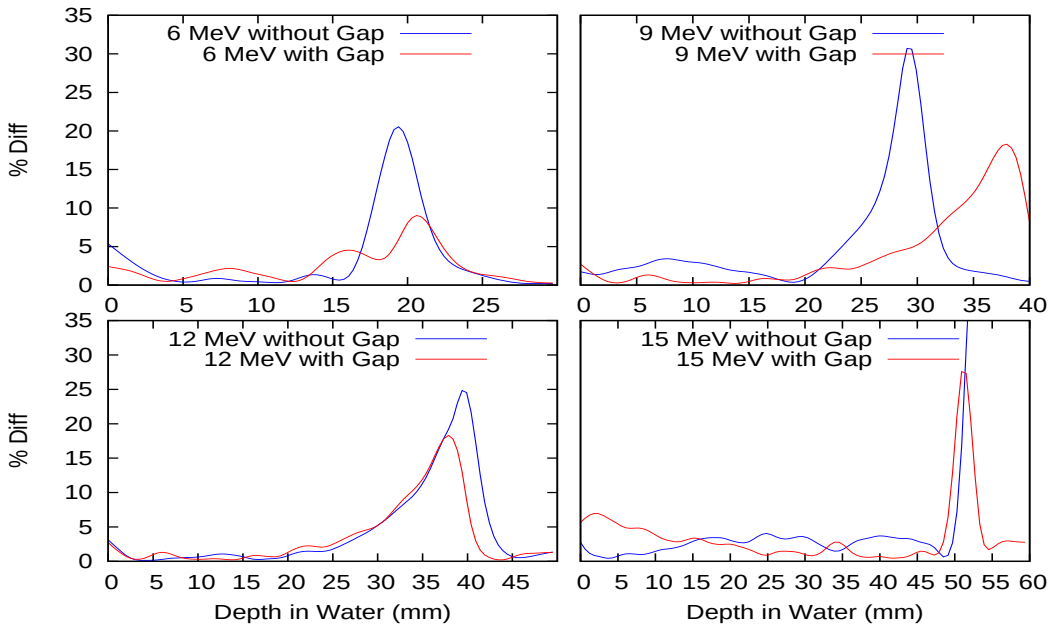

Figure 5.12: Percentage difference comparisons between BEAMnrc MC results with and without a gap to film results of the EBF and upstream dose for electron beams of energies 6, 9, 12, and 15 MeV. The figure shows that the percentage difference decreases in the vicinity of the lead interface when the gap to accommodate the Gafchromic film in the physical measurement is accounted for. The lead interface was positioned at depths of 20, 30, 40, and 52 mm for the 6, 9, 12, and 15 MeV electron beams respectively.

From this simulation it can be concluded that the film measurements are underestimating the EBF and upstream dose enhancement due to the gap in the lead. The agreement between the BEAMnrc MC with the gap and film measurements are closer for all energies, as shown in Figure 5.13. Although the agreement has improved, there is still a large difference for 12 MeV. This may indicate that the experimental setup for the 12 MeV measurement had a larger gap than the other experimental set ups. However, there is a significant amount of noise in the gap simulated BEAMnrc MC data due to the small voxel sizes used to simulate the thickness of the lead. The simulation of this gap will not be included in any further measurements; rather, ignoring the gap will give a result that should be closer to what would occur in a normal internal shielding treatment.

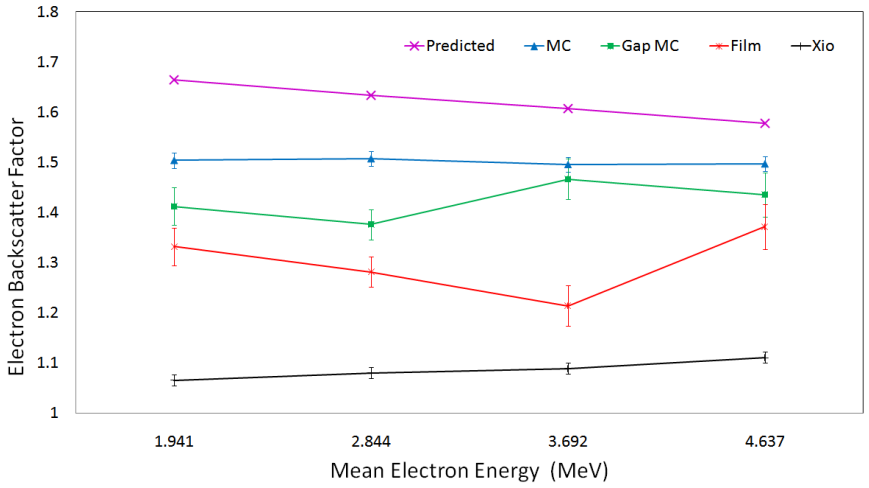

Figure 5.13: Graph comparing electron backscatter values calculated from Gafchromic film, XiO eMC, and BEAMnrc MC simulations with and without a gap in the lead against the mean energy at the lead interface. Estimated values from the currently used equation are also plotted. The measurement depths were 20, 30, 40 and 52 mm for energies of 6, 9, 12, and 15 MeV. The mean energies at the lead interface were 1.941, 2.844, 3.692, and 4.637 MeV respectively. An improvement in agreement between the BEAMnrc MC and Gafchromic film values can be seen when the gap is included in the BEAMnrc simulation.

5.3.2 Comparison with Pencil Beam Algorithm

Although more and more centers are using Monte Carlo type algorithms for electron dose calculations, such as XiO's eMC which was examined in the previous sections, there are still many centers using an older type of electron algorithm, namely the Hogstrom's Pencil beam algorithm(51). As this algorithm is still widely used it is interesting and worth while to perform a simple comparison between XiO's Hogstrom type pencil beam algorithm, XiO's eMC, and BEAMnrc algorithms.

The Pencil beam algorithm calculates dose by summation of dose distributions from many individual electron pencil beams. The individual pencil beam dose distributions are calculated using the Fermi-Eyges scattering theory. A complete description of the algorithm can easily be found in the literature and text books(6; 8; 10; 51; 52). Even though the Monte Carlo method offers a more accurate calculation method, the pencil beam algorithm is still in wide use due to several reasons such as: difficulty in commissioning for local machines, little demand by local radiation oncologists, and the financial expense of purchasing alternative Monte Carlo type algorithms(52).

Figure 5.14 compares PDD curves for 6, 9, 12, and 15 MeV energy electron beams calculated using XiO's eMC and pencil beam algorithms as well as the BEAMnrc MC results. The simulation geometry was exactly as described in section 5.1.2. The comparison shows that there is significant improvement in using XiO's eMC to estimate the transmission dose through the lead shielding. The fact that the pencil beam algorithm cannot accurately calculate transmission dose is not surprising as the Fermi-Eyges scattering theory assumes that all electrons reach their practical range, which depends on the relative density of material the electron is traveling through.

This is physically not true as electrons which are scattered by large angles, such as backscattered electrons, have shorter ranges(52). The comparison also confirms that XiO's eMC does predict a small degree of electron backscatter.

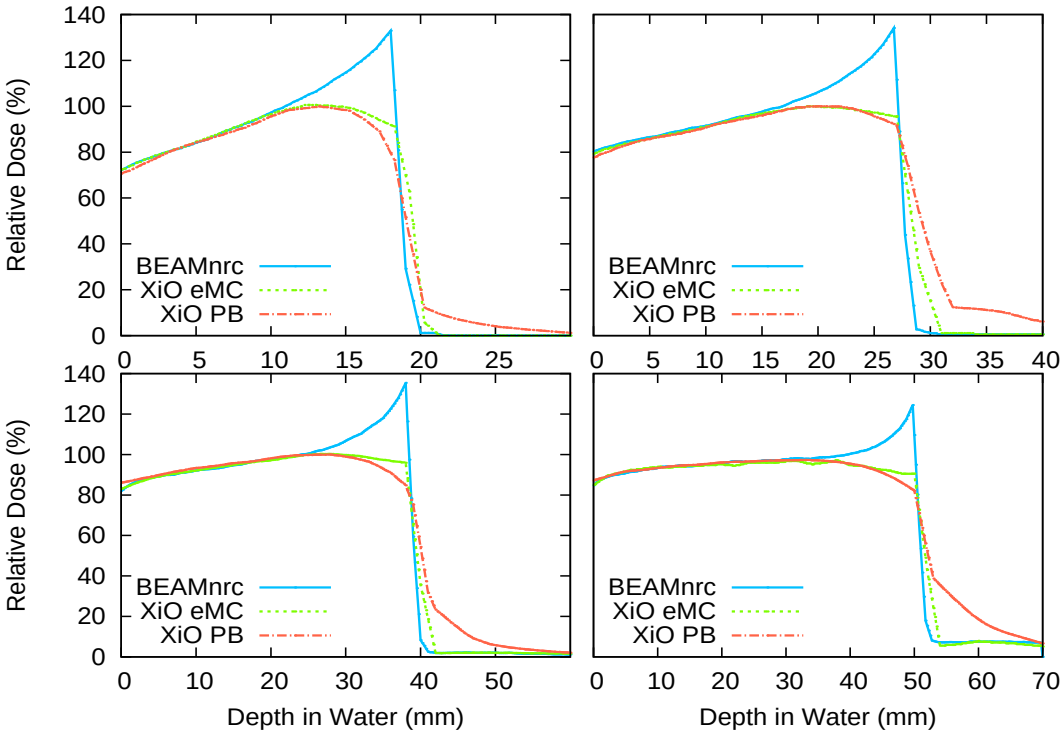

Figure 5.14: Comparison of electron depth dose curves involving lead shielding calculated by XiO's eMC algorithm(green) and XiO's pencil beam algorithm (red) against BEAMnrc Monte Carlo simulations(blue). The figure shows 6(top right), 9(top left), 12(bottom right), and 15(bottom left) MeV electron depth dose curves with lead shielding positioned at depths of 20, 30, 40, and 52 mm, corresponding to each beam's therapeutic depth.

5.4 Conclusion

A BEAMnrc MC model of a Siemens Artiste Linac was used to model dose distributions in the presence of lead shielding, emulating an internal shielding

treatment situation. Several different energy electron beams were examined, with the lead interface placed at their respective therapeutic depths. DOSXYZnrc was used to calculate dose distributions for each different electron energy beam. These results were compared to dose distributions estimated from XiO's eMC TPS and Gafchromic film measurements.

The resulting dose distributions were used to calculate electron backscatter factors (EBF). The EBF values from the various methods were not in complete agreement with each other. EBF values were largest for the DOSXYZnrc simulations, and XiO eMC algorithm overall predicted the lowest EBF values.

The dose distributions were also used to compare the estimated upstream dose enhancement caused by the shielding. The upstream dose enhancement from the lead interface was not prominent in the XiO eMC simulations. Agreement of the upstream dose enhancement was best between the BEAMnrc MC simulations and Gafchromic film measurements for the majority of energies.

The dose distributions were compared using a percentage-distance to agreement calculation. The comparison between the dose distributions of all three measurement techniques concluded that the agreement was best between the BEAMnrc MC dose distribution and the Gafchromic film measurements. The comparisons between the XiO eMC dose distributions and BEAMnrc MC dose distributions show significant disagreement upstream from the lead interface, which was also seen in the PDD results.

EBF values were also predicted by the equation by Klevenhagen(19), and were found to universally predict a greater EBF value than all three measurement techniques for all energies examined. As discussed in section 1.4, the accuracy of

this equation in situations where the energy is in the region of 3 MeV or below is questionable. This energy region at the lead interface is common if the lead is to be placed at the therapeutic depths for the local electron beams. For these reasons the clinical use of this equation is questionable and physical measurements should always be made to verify the predicted values.

An investigation of the effect of the gap in the experimental setup was also undertaken. The results concluded that the gap decreases the EBF value that the Gafchromic film should measure, therefore the Gafchromic film results presented here are most likely underestimating the EBF values and upstream dose enhancement. This further emphasizes that XiO's eMC underestimates the electron backscatter.

Overall, it can be concluded that XiO's eMC algorithm should not be used to estimate dose distributions when lead shielding is involved. Furthermore, the use of the equation by Klevenhagen(19) to estimate the EBF value is also questionable and warrants further investigation. The dose distribution agreement between BEAMnrc and the Gafchromic film measurements were found to be clinically acceptable in all regions except for the region very close to the lead interface. This disagreement is thought to be due to the physical limitations of the experimental measurement set up.

Chapter 6

Evaluation of Currently Employed Equations

This chapter will focus on determining if Equation 1.8 is capable of estimating the EBF value, for the local electron beams over a wide range of energies, to a clinically acceptable accuracy level. The upstream dose enhancement will also be examined over the same energy range to determine the accuracy of Equation 1.11. The accuracy of Equation 1.8 in the energy range of 1 to 3 MeV is already under debate in the literature, as discussed in section 1.4. Since Equation 1.8 was fitted to data over the range of 3 to 35 MeV and it may not be appropriate to use this equation to calculate values for lower energies. The results from Chapter 5 show a trend of divergence from the equation as the energy decreases from 4 MeV. It is expected that the results in this chapter will show a similar trend of overestimation for energies lower than 4 MeV.

6.1 Methods and Materials

To assess the accuracy of the equations, the BEAMnrc MC model developed in Chapter 4 was used to simulate lead interfaces at multiple depths for each energy electron beam. The BEAMnrc phase space file used for these calculations was the same phase space files for energies of 6, 9, 12, and 15 MeV as verified in Chapter 4. Calculations were performed on a DOSXYZnrc phantom with an SSD of 100 cm. The simulation time was minimised by using a phantom with only a single column of $(5, 5, 1)$ mm (X, Y, Z) voxels positioned centrally along the Z axis to an adequate depth for the electron beam in question. The calculation parameters for DOSXYZnrc remained the same as those described in Chapter 5.

Positioning the lead at multiple depths in water allowed for the calculation of EBF values and upstream EBI curves over a large range of mean electron energies. The mean energy at the interface was estimated with Equation 1.9 using the values of R_p and the mean energy at the surface E_0. The value of E_0 was calculated with Equation 2.8 using the R_{50} value. Both the values of R_p and R_{50} were calculated from the BEAMnrc results and are shown in Tables 4.3 and 4.4. Equations 6.1 and 6.2, along with Equation 6.3 and Table 6.1 were used to estimate EBF values and upstream EBI curves at the corresponding energy for comparison. These equations were introduced in Chapter 1 and are reproduced here for convenience.

EBF and Upstream EBI Equations

To estimate the EBF value for a lead interface the following equation was used;

$$EBF = 1 + 0.735 \exp^{-0.052 E_m}, \tag{6.1}$$

where E_m is the energy at the lead interface and can be calculated using Equation 1.9, which estimates the mean energy, E_z, at a depth of z mm.

To estimate the upstream dose enhancement the following equation was used;

$$EBI(t) = EBF \times A \exp^{-kt}, \tag{6.2}$$

where t is the distance in mm in the upstream direction from the lead interface. The value of EBF is calculated from Equation 6.1. k is a constant dependent on the primary electron beam energy and is calculated using Equation 6.3.

$$k = 0.61 E_m^{-0.62}. \tag{6.3}$$

The value of the constant A in Equation 6.2 is also dependent on the primary electron beam energy and is estimated using Table 6.1.

Beam Energy (MeV)	A	k
1-9	1.0	calculated by Equation 6.3
10-13	0.934	calculated by Equation 6.3
14-25	0.792	0.10

Table 6.1: Constants used in conjunction with Equation 6.2 to determine the upstream intensity of backscattered electrons (EBI) from a lead interface for a given electron energy at the interface. Reproduced from (26).

Lead Positions

The range of lead depths simulated for each energy electron beam are shown in Table 6.2. Each simulation had an adequately thick layer of lead to ensure maximum electron backscatter was achieved. Two million histories were simulated with a recycling rate of 2, which resulted in a statistical accuracy of less than 1.0 % for all

voxels shallower than the lead interface. The total number of simulations performed was 84 and each simulation required around 1 hr of calculation time. This resulted in a number of EBF values and upstream EBI curves for a range of mean electron energies at the lead interface in the range of 0.2 to 14 MeV.

Energy	Depth Range (mm)	Interval (mm)
6 MeV	3 - 29	1
9 MeV	3 - 45	2
12 MeV	3 - 60	3
15 MeV	4 - 76	4

Table 6.2: Table describing the positions (range and interval) at which lead was placed for electron backscatter factor simulations. A range of depths was used to alter the mean energy at the lead interface according to Equation 1.9.

The output file from the DOSXYZnrc simulations was rearranged using an Excel Macro, resulting in a single depth dose curve along the central axis for each simulation. The curves were normalised to d_{max} for a standard 10 $\times$ 10 cm electron field PDD curve for the corresponding energy, simulated in an identical phantom without lead present.

6.2 Results

6.2.1 Electron Backscatter Factor

Figure 6.8 displays the resulting PDD curves for all lead depth positions for each electron beam energy. The bold red curve represents the standard electron PDD. The EBF values were calculated from these PDD curves as the ratio of dose at the interface from the simulation involving lead to the regular PDD. The calculated EBF

values are plotted for each energy in Figure 6.2 as a function of the mean energy at the lead interface. The estimated EBF values from Equation 6.1 are also plotted on Figure 6.2 for comparison.

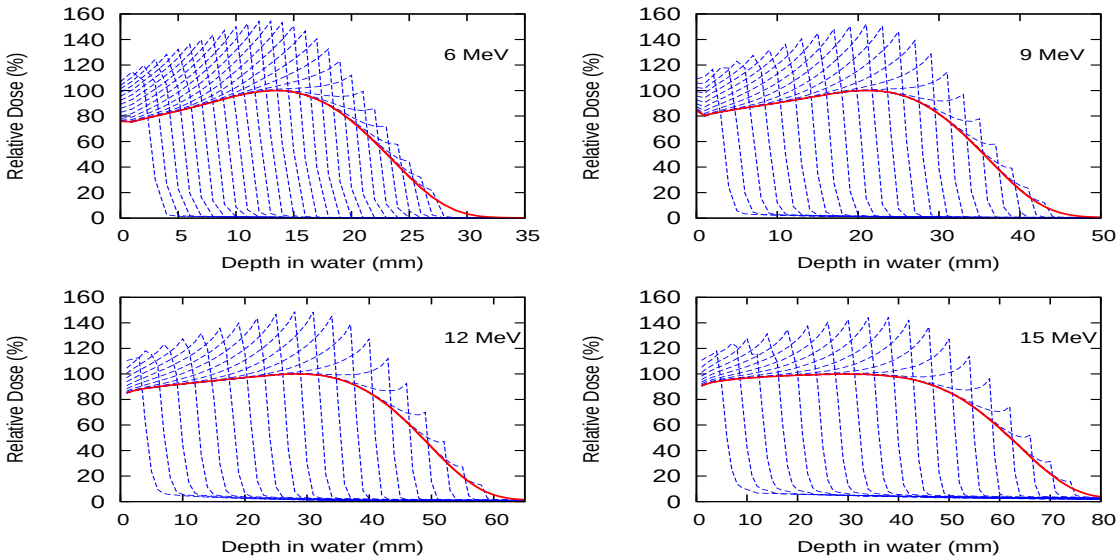

Figure 6.1: Graph of depth dose curves for different lead positions for electron beams with energies of 6, 9, 12, and 15 MeV(blue curves). The red curves represents the standard percentage depth dose curve for each energy respectively. The electron backscatter and upstream dose due to the lead is clearly seen. The depth positions of the lead are described by Table 6.2.

The results from the BEAMnrc MC simulations, as shown in Figure 6.2, clearly do not follow an exponential curve of the type $A + B\exp^{-c\times E_m}$, such as the current equation. The disparity between the current equation and the MC results is most evident in the lower energy range. The current equation overestimates the EBF value by 11.6 % on average in the energy range of 1 to 5 MeV, with a maximum overestimation of 31 %. The agreement in the energy range above 5 MeV is much better and on average the equation only overestimates the EBF value by 3.8 % in this energy range.

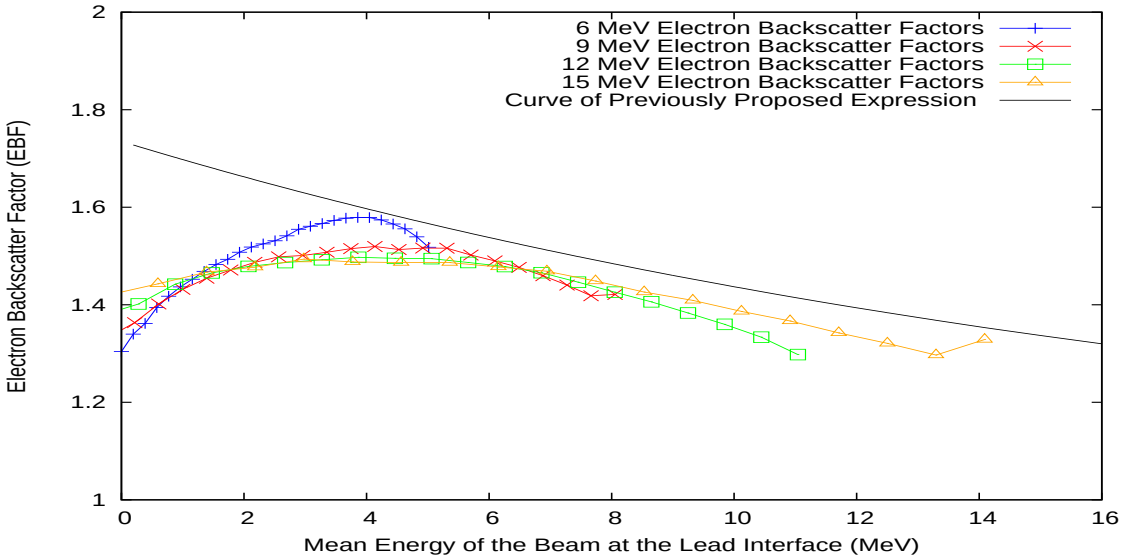

Figure 6.2: Comparison of BEAMnrc MC simulated EBF values to estimated EBF values from Equation 6.1 for electron backscatter created by electron beams with energies of 6 (blue), 9 (red), 12 (green), and 15 (orange) MeV from lead plotted against the mean electron energy at the interface. The depth of lead interfaces are described by Table 6.2.

6.2.2 Upstream Electron Backscatter Intensity

To determine if the upstream EBI Equation 6.2 is able to estimate the upstream dose enhancement to a clinically acceptable level, the upstream EBI curves from the BEAMnrc MC simulations were collated. This was performed by subtracting the nominal PDD curve for each of the lead interface simulation results which resulted in upstream EBI curves for a range of lead interface energies. The upstream EBI curves for all the simulations are shown in Figure 6.3, separated into several different energy ranges. Figure 6.3 also show the upstream EBI range over each energy interval estimated by Equation 6.2 (black dashed curves).

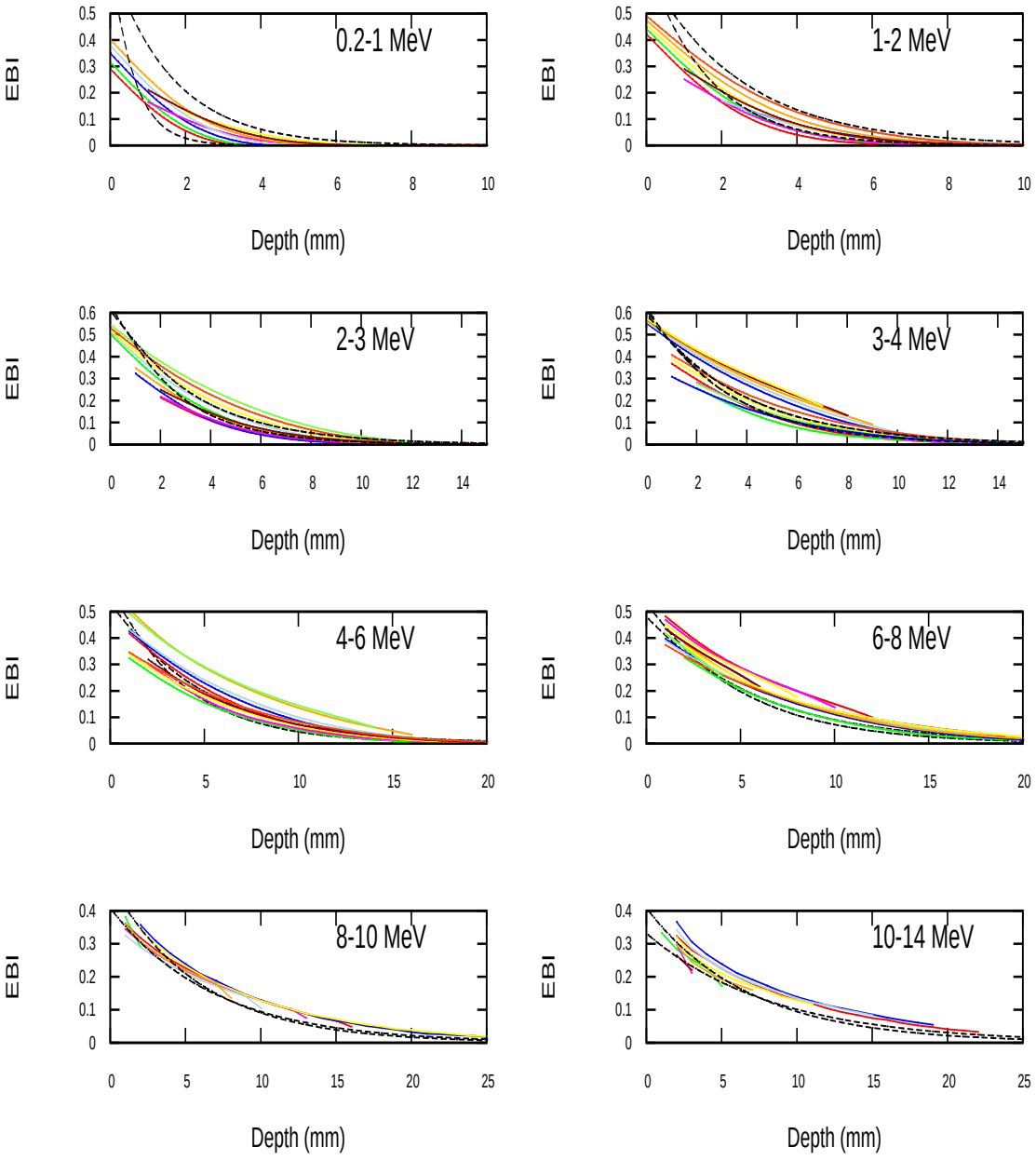

Figure 6.3: Graph of relative upstream electron backscatter intensities (EBI) in the upstream direction from a lead-water interface for several different energy ranges calculated from BEAMnrc Monte Carlo simulations (coloured). The dashed black lines represent the upstream EBI range estimated by Equation 6.2.

6.2.3 Analysis

Electron Backscatter Value

The results from Section 6.2.1 show that the current equation overestimates the EBF value over the entire energy range investigated. To be able to easily estimate the EBF value for the local electron beams, a new empirical equation was fitted to the data. This equation must reflect the decreasing EBF value seen at low energies, as shown from the results. This cannot be done with a single exponential decay equation. A least squares method was used to fit a double exponential function to the data, which is shown in Equation 6.4. The equation is also plotted with the BEAMnrc results for the local electron beam (red) and previous results from the literature (blue) in Figure 6.4.

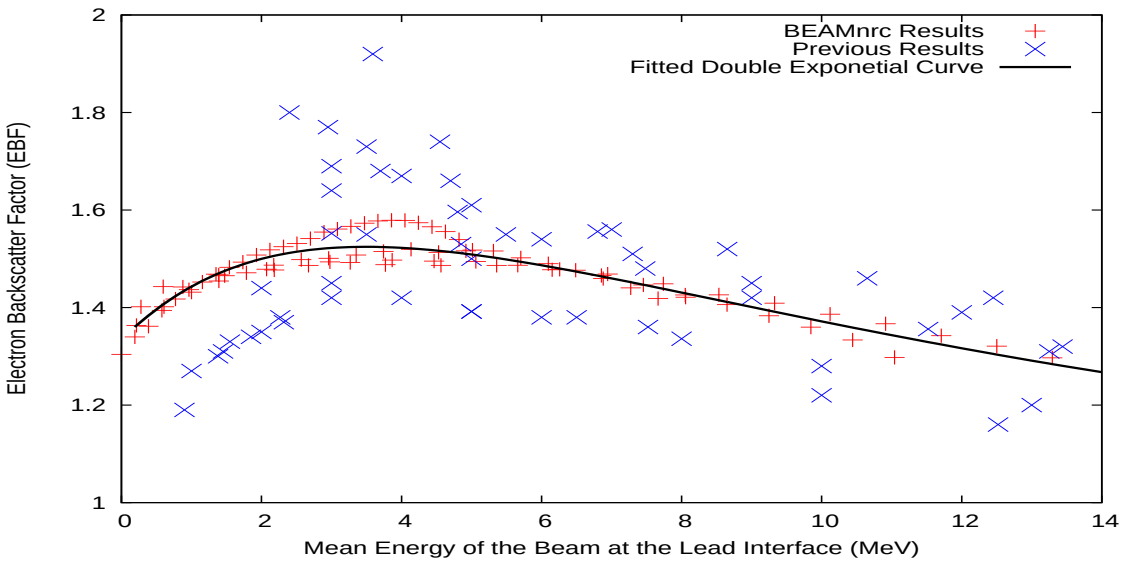

Figure 6.4: Graph of EBF values calculated from a BEAMnrc MC simulation (red) and previous results sourced from the literature (blue). The proposed empirical double exponential equation (black curve) is also plotted. The double exponential equation agrees with the MC simulated EBF values with an average percentage difference of 1.3 % with a maximum percentage difference of 4.9 %.

$$EBF(E_m) = 1 + 0.936\exp^{-0.089E_m} - 0.602\exp^{-0.375E_m}. \quad (6.4)$$

Equation 6.4 agrees with the results in this work to an average percentage difference of 1.3 %. The maximum percentage difference was 4.9 %. The equation agrees with previous EBF values from the literature(14; 19; 21; 22; 23; 24; 25) to an average percentage difference of 7.9 %. The average percentage difference between Equation 6.4 and the literature is fairly large, however, when the variation amongst the reported EBF values is considered, a percentage difference of 7.9 % is acceptable. Furthermore, Equation 6.4 generally follows the trend of the previously reported results.

Electron Backscatter Intensity

The results in Figure 6.3 show acceptable agreement between the currently used equation and the Monte Carlo results for the upstream EBI over every energy range for the local electron beams to a considerable upstream distance from the interface. However, the equation does to some extent predict lower values of EBI for energies above 2 MeV, below this energy the equation estimates a higher EBI, especially near the lead interface. This overestimation at lower energies has already been seen in Figure 6.2.

Although the equation showed acceptable agreement over much of the energy ranges, a new equation was fitted to this data to allow for a more accurate method of estimating the upstream EBI empirically for low energies. To do this, the upstream EBI curves for each energy range shown if Figure 6.3 were averaged. An exponential decay curve of the type $A\exp^{-k\times t}$ was fitted to each of the energy ranges. The

coefficients of each of these curves was plotted against the mean energy to determine if any relationship existed. The relationship between the coefficient A and the mean energy was found to be describable by a linear function, and the relationship between the coefficient k and the mean energy was found to fit a power function remarkably similar to Equation 6.3. The resulting empirical equation to estimate the upstream EBI is shown in Equation 6.5.

$$EBI(t) = A \exp^{-kt}, \tag{6.5}$$

where t is the upstream distance from the lead interface in mm, A is a coefficient calculated with Equation 6.6, and k is a coefficient calculated with Equation 6.7.

$$A(E_m) = -0.041E_m + 0.847, \tag{6.6}$$

$$k(E_m) = 0.601E_m^{-0.736}, \tag{6.7}$$

where E_m is the mean energy at the lead interface.

The resulting equation agreed with the averaged upstream EBI curves to within 10 % for the first 15 mm upstream from the lead interface for all energy ranges. The predicted curves from these equations are shown in Figure 6.5 in blue. Figure 6.5 also shows the averaged upstream EBI curves for each energy range (black) and predicted curves from Equation 6.2 (red) for comparison.

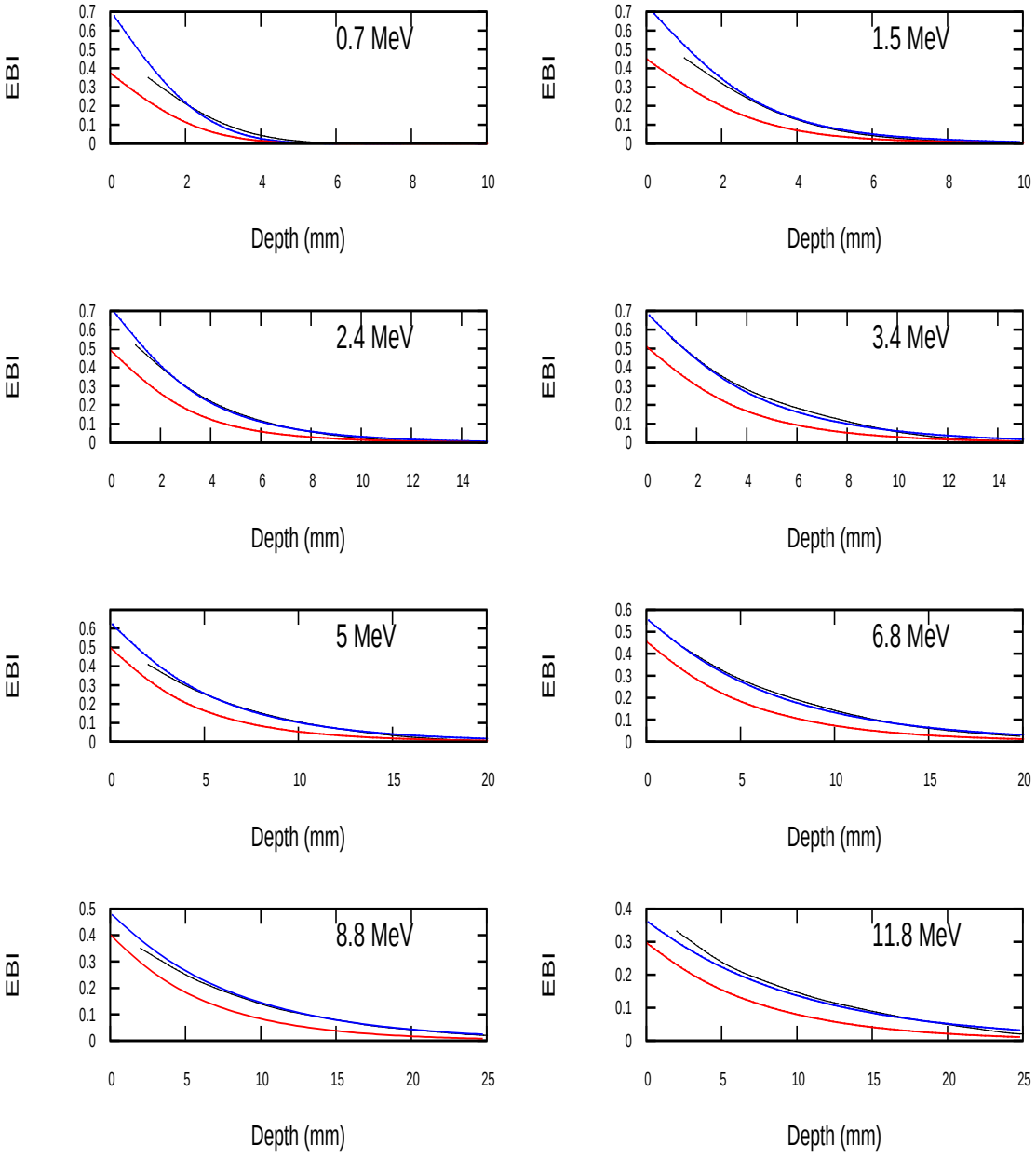

Figure 6.5: Graph of relative upstream electron backscatter intensity (EBI) in the upstream direction from a lead-water interface for several different energies. Showing the overestimation between the Monte Carlo data (black) against the estimation from the clinically used equation (red), this overestimation increases with increasing energy. A proposed new equation (blue) (Equation 6.5) for the estimation of the upstream electron backscatter intensity is also plotted and shows better agreement.

6.3 Discussion

The above proposed equations are physically limited in that the value of the EBF does not agree with the value of EBI when the upstream distance, t, is set to zero. Physically, these two values should agree at this point. This limitation is clearly shown when both the EBF and EBI values at the lead interface are plotted together, as seen in Figure 6.6. This disagreement at the interface is due to both equations being derived independently of each other. This limitation also exists with Equation 6.2 above 9 MeV, where the coefficient A drops to 0.934 and above 14 MeV where the coefficient A drops to 0.792.

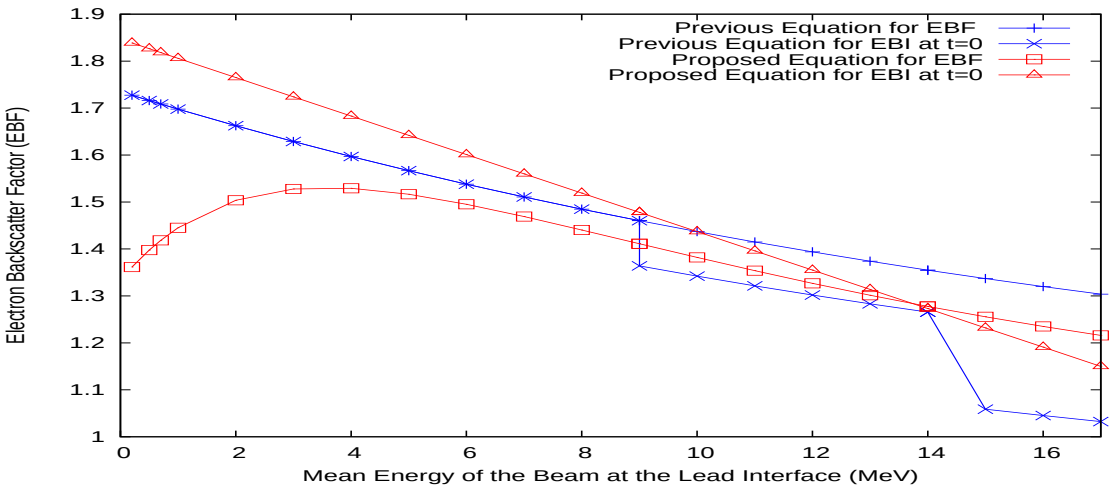

Figure 6.6: Graph comparing the values predicted by the previous equations (blue) and new equation (red) for the EBF and EBI at the lead interface ($t = 0$). The values should be identical; clearly both the new and original sets of equations do not agree under this condition.

Therefore, an equation was derived which does satisfy this condition and a new term electron backscatter, EB, was introduced. The new term, EB, in Equation 6.8 is defined as the ratio of dose at a distance, t, in mm which is at, or upstream from

a lead interface, to the dose at the same depth without the lead interface present. Therefore, satisfying $EBF(E_m) = EBI(E_m, t = 0) = EB(E_m, t = 0)$.

$$EB(E_m, t) = EBF(E_m) \exp^{-kt}, \tag{6.8}$$

where the value of EBF is calculated using Equation 6.4, and k is described by the logarithmic expression derived from the data and shown in Equation 6.9.

$$k(E_m) = -0.130 \ln(E_m) + 0.410, \tag{6.9}$$

where E_m is the mean energy at the lead interface. The resulting equation is one that can be used to estimate the dose enhancement caused from a lead interface for a depth at, or shallower than the depth of the interface for any electron energy locally available. Combining Equations 6.4, 6.8 and 6.9 results in the final equation,

$$EB(E_m, t) = 1 + \left(0.936 \exp^{-0.089E_m - 0.41t} - 0.602 \exp^{-0.375E_m - 0.41t}\right) E_m^{0.13t}, \tag{6.10}$$

A similar comparison to Figure 6.5 was performed to assess the agreement of Equation 6.10 against the Monte Carlo and predicted EBI curves. This is plotted in Figure 6.7. Overall, the agreement is still excellent for the higher energy EBI curves. The results were acceptable for the lower energy curves, however, the independently derived Equation 6.5 showed better agreement over all energy ranges. The average Pearson's correlation between the MC curves and the independently derived equation curves was 0.998, whereas the curves predicted from the new equation had an average Pearson's correlation of 0.987

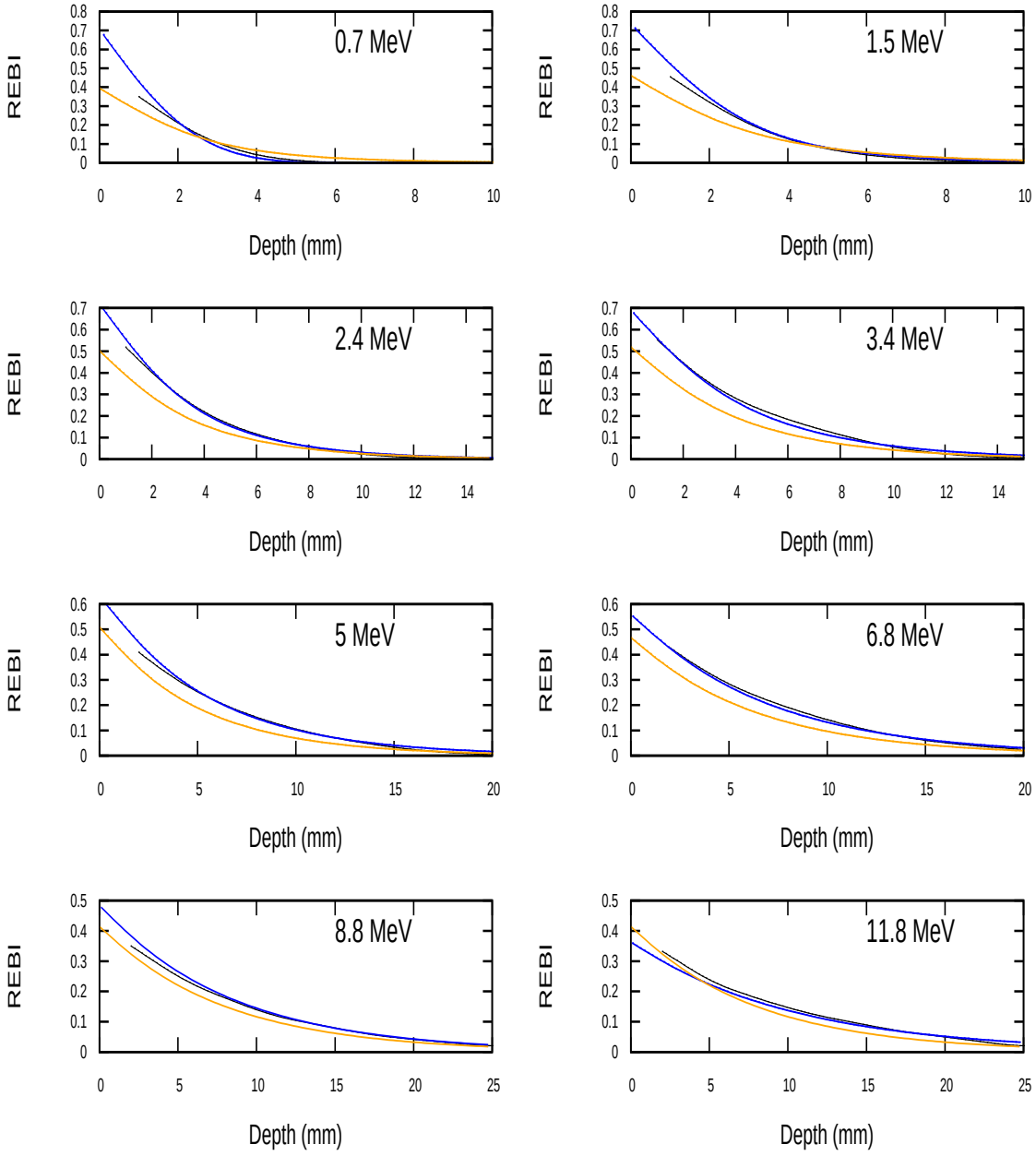

Figure 6.7: Graph of relative upstream electron backscatter intensity (EBI) in the upstream direction from a lead-water interface for several different energies. Showing the comparison between the Monte Carlo data (black) against the proposed independently derived equation (blue) (Equation 6.5) and the new proposed equation (yellow) (Equation 6.10) which satisfies the condition $EBF(E_m) = EBI(E_m, t = 0)$ for the estimation of the upstream electron backscatter intensity.

Equation 6.10 can also be slightly modified to empirically predict the depth dose curves involving a lead interface at any particular depth. Multiplying Equation 6.10 by the standard electron PDD curve and describing the lead position relative to the surface yields the following expression,

$$EB_{PDD}(x) = \begin{cases} PDD(E_0, x)(1 + (EBF(E_m) - 1)\exp^{-k(E_m)(z-x)} & \text{if } 0 \leq x \leq z \\ 0 & \text{otherwise,} \end{cases} \tag{6.11}$$

where x is the depth from the surface in mm, E_m is the energy at the lead interface at a particular depth, z, in mm for an electron beam with a nominal percentage depth dose curve, $PDD(hv)$. Equation 6.11 ignores any penetration into the lead, which should be adequately thick to provide saturation backscatter levels. Predicted PDD curves from Equation 6.11 are shown in Figure 6.8 and are compared against the MC calculated curves. The results reflect the disagreement at lower energies seen in Figure 6.7. Overall, the equation empirically predicts the PDD curves to an acceptable accuracy level over a wide range of energies along the central axis.

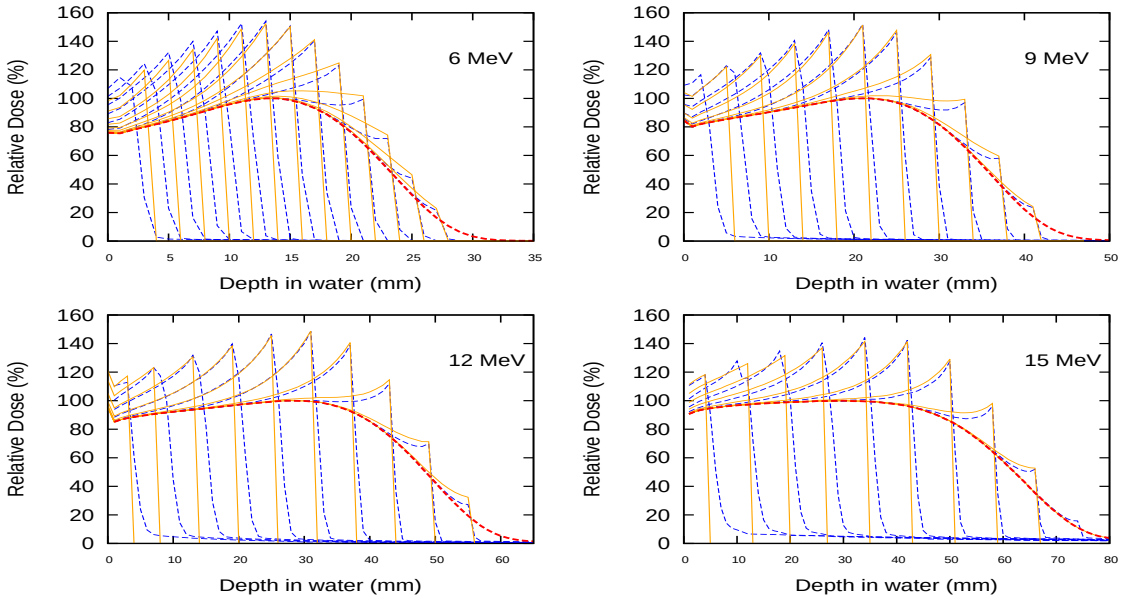

Figure 6.8: Graph of depth dose curves for different lead position for 6, 9, 12, and 15 MeV electron beams predicted by Monte Carlo calculations (blue) and by Equation 6.11 (orange). The red line represents the nominal percentage depth dose curve for each energy electron beam respectively.

6.4 Conclusion

A number of Monte Carlo lead shielding interface simulations, at different depths and energies in water, for the local electron beams were performed. The results from these simulations showed that the currently used clinical equations are not able to estimate the EBF value and upstream EBI over the entire energy range in question to a clinically acceptable level. This disagreement between the equations and the results for the EBF values is significant in the 4 MeV and below mean energy at the interface range. This energy range is often where the lead-tissue interface is present in an internal shielding treatment and therefore, it is imperative that an empirical equation is available to accurately estimate the EBF value.

This has lead to the proposal of a new empirical equation which was fitted to the MC data. The equation estimates the EBF value to an average percentage difference of 1.3 % with a maximum of 4.9 % over all the MC simulation data collated here. This equation also follows a trend similar to previously measured EBF values from the literature.

A similar disagreement was found for the equation used to estimate the upstream dose enhancement from the lead interface. The upstream EBI equation fails in the lower energy range. This will allow a more accurate estimation of the required thickness of absorber needed to diminish the upstream dose enhancement in this energy range.

Although the proposed Equations 6.4 and 6.5 from the simulation results for the EBF and EBI showed excellent agreement they did not meet the condition of agreement at the lead interface, where the distance from the lead surface is zero for the EBI equation. This led to a new equation for electron backscatter that can be universally used to calculate the EBF value at the interface and the upstream EBI value for all local energy electron beams. In deriving Equation 6.10 the results showed that there was a sacrifice in accuracy in estimating the upstream EBI for the lower energy beams, although, the loss of accuracy is justified to ensure that the equations agree under this condition.

Chapter 7

Final Conclusions

This thesis set out to investigate the limitations in the current local internal shielding method for electron treatments, focusing on the accuracy of XiO's eMC algorithm, through comparisons with Monte Carlo simulations and film measurements. Comparisons between the three methods were primarily presented through electron backscatter factors (EBF) and upstream electron backscatter intensity (EBI) curves. The investigation also sought to confirm the accuracy of the equations used to estimate the electron backscatter factor and upstream electron backscatter intensity for electron beams produced by a Siemens Artiste Linac. The accuracy of the current equations was determined through comparisons of multiple Monte Carlo simulations over a range of electron energies to the corresponding predicted values of EBF and EBI curves.

One concerning result found in the literature was the vastly varying values of measured EBF as reported from several different studies; this is especially evident in the energy region below 4 MeV. In this energy region the EBF value has been stated

to be between 1.92 and 1.27, a difference of more than 50 %. Many of the studies explicitly state that the difference is most likely due to either limitations in attempting to measure a point type quantity with volumetric devices, or the differences in spectra involved and hence concluding that the EBF value are machine specific.

The machines used to derive these electron backscatter equations were several linacs and a betatron which are now obsolete. The energy range over which the EBF values were measured was in the energy regions of 3 to 35 MeV and 1 to 25 MeV for the upstream EBI. Extrapolating these equations to all types of electron generating devices and to lower energy regions could prove erroneous due to the spectral difference between machine fluences and unforeseen relationships in the lower extrapolated energy region.

This has lead to the two specific questions this investigation sought to answer.

1. Does XiO's eMC algorithm possess the ability to accurately predict dose around high density material such as lead? And if XiO's eMC is shown to fail in these situations, then to what extent does it fail?

2. Do the currently used empirical equations predict, to a clinically acceptable accuracy level, the correct values for the EBF and upstream EBI for the local electron beams?

To answer these questions the Monte Carlo method was used due to its ability to calculate dose to arbitrary sized voxels, which is advantageous in measuring point quantities such as the EBF. Furthermore, the Monte Carlo method avoids any fluence perturbation in the results which would be present if a conventional dosimeter was used. The intention of using a Monte Carlo simulation was to emulate the electron

spectral characteristics of the local Linacs. The development of a Linac treatment head MC model and the process of verifying its accuracy has been described and the results presented, concluding that the model easily surpassed the sought accuracy of 2 % and 2 mm. The model was verified against measurements made with a BP2 scanning water phantom using an electron diode detector over several field sizes and energies. This level of agreement to the physical measurements gives confidence in the similarity between the physical and simulated electron energy fluence.

Physical dose distributions involving electron backscatter from lead were measured using Gafchromic film submerged in water. The results of which were compared to both XiO's eMC electron treatment planning algorithms and results from the BEAMnrc MC model. The dose distributions derived from the Gafchromic measurements showed some interesting features. The BEAMnrc MC measurements were not in full agreement with the measurements derived from the Gafchromic film. These deviations have been explained and are associated with the limitations of the measuring apparatus used to position the film and lead. Even with these limitations in the measurement apparatus the derived dose distributions agreed better with the BEAMnrc simulation results than the XiO eMC predicted dose distributions for all electron beams with the exception of 12 MeV. It is thought that the apparatus's limitation was larger in this particular measurement set up.

The MC Linac simulations, film measurements, and XiO eMC dose distributions were used to answer the specific questions. The main findings were summarised within Chapter 5: *Dose Distribution in the Presence of High Atomic Material* and Chapter 6: *Evaluation of Currently Employed Equations*. This section will relate those findings to form a definite answer to these research questions.

1. Does XiO's eMC algorithm possess the ability to accurately predict dose around high density material such as lead? And if XiO's eMC is shown to fail in these situations, then to what extent does it fail?

The results demonstrated that, over the energy range examined, XiO's eMC algorithm does not possess the ability to accurately predict the dose around lead. All of the dose distributions from XiO's eMC in this study show little dose enhancement upstream of the lead when compared to the upstream dose enhancement measured by the film, BEAMnrc simulations, and reported in the literature. EBF values calculated from XiO were 10 to 30 % lower than these three methods. Furthermore, the highest EBF value estimated by XiO's eMC coincides with the lowest measured value reported in the literature measured for an electron beam with an energy three times greater. Therefore, it can be confidently stated that XiO's eMC is not accurate around high density material, with the overall results showing the extent of dose prediction failure is between 10 to upwards of 20 % over the energy range investigated when compared to other means of estimation for the local electron beams.

2. Do the currently used empirical equations predict, to a clinically acceptable accuracy level, the correct values for the EBF and upstream EBI for the local electron beams?

The results verify that over the energy range of 1 to 5 MeV the equation is unable to predict the EBF value to a clinically acceptable level. The equation overestimated the EBF value in this region by 11.6 to 31 %, however, above 5 MeV the equation more accurately predicts the EBF value but still overestimates it by 3.8 %. The deviation in the lower energy region has lead to the derivation of a new equation which estimated

the EBF value for local beams over the entire energy range available. This equation is plotted in Figure 7.1.

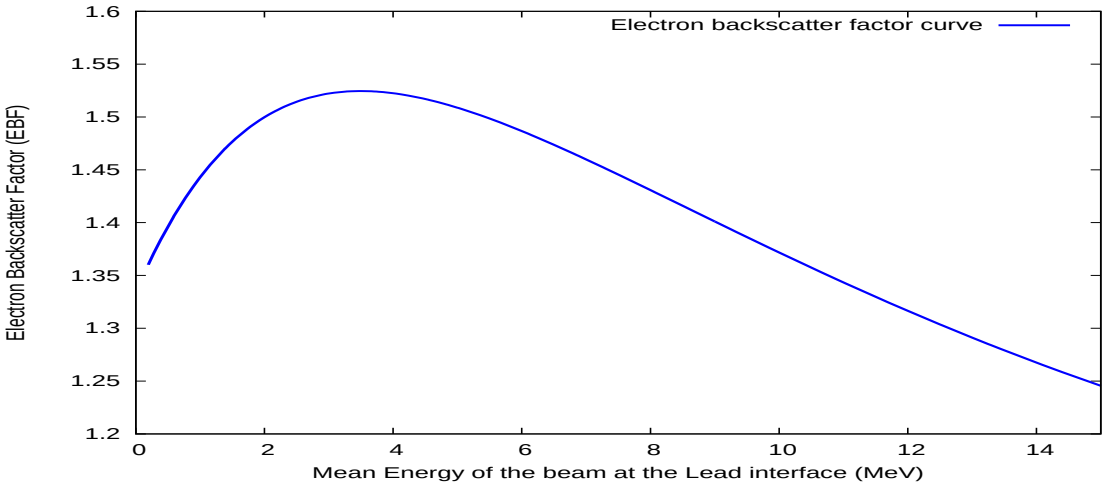

Figure 7.1: Graph of Electron Backscatter Factors derived from BEAMnrc MC simulation data. The derived equation (Equations 6.4) is a double exponential equation which agrees with the MC simulated EBF values with an average percentage difference of 1.3 % and a maximum percentage difference of 4.9 %.

The resulting curve from Figure 7.1 allows the debated behavior of the EBF value in the lower energy region to be resolved. That is, the relationship between energy and the EBF first increases with increasing energy, until a maximum is reached, and then decreases more slowly with further increases of energy.

The EBI curves from the MC simulation results confirm that, in the lower energy range, the equation for the EBI is unable to estimate values to a clinically acceptable level. The current equation overestimates the dose at these energies. A new equation was derived from the BEAMnrc MC data to estimate EBI curves which was of a similar type to the current equation. This equation showed better agreement than the current equation for all energies when compared to the BEAMnrc MC results. However, it was concluded to be more appropriate to only have a single equation

for the EBF and upstream EBI as the two equations should converge at the lead interface.

A set of equations was derived which fit this condition. This resulted in a set of equations that are able to estimate dose enhancement from electron backscatter for any local energy electron beam, at any depth shallower than the lead interface, which is shown in Equation 7.1. This equation shows better agreement in estimating the EBI than the currently used equation, but it is somewhat worse than the independently derived equation of the same type. The average Pearson's correlation between the MC and the independent equation was 0.998, whereas the new equation had an average Pearson's correlation of 0.987. Equation 7.1 can also be used to estimate depth dose curves involving lead interfaces when multiplied by the nominal PDD for the electron beam in question.

$$EB(E_m, x) = 1 + (EBF(E_m) - 1)\exp^{-k(E_m)(z-x)}, \tag{7.1}$$

where x is the depth in mm from the surface, z is the depth of the lead interface, E_m is the mean energy at the lead interface, and the value for $EBF(E_m)$ and $k(E_m)$ are given by the expressions,

$$EBF(E_m) = 1 + 0.936\exp^{-0.089E_m} - 0.602\exp^{-0.375E_m}, \tag{7.2}$$

and,

$$k(E_m) = -0.130\ln(E_m) + 0.410. \tag{7.3}$$

Figure 7.2 shows a series of upstream dose enhancement curves for different energies estimated from Equation 7.1.

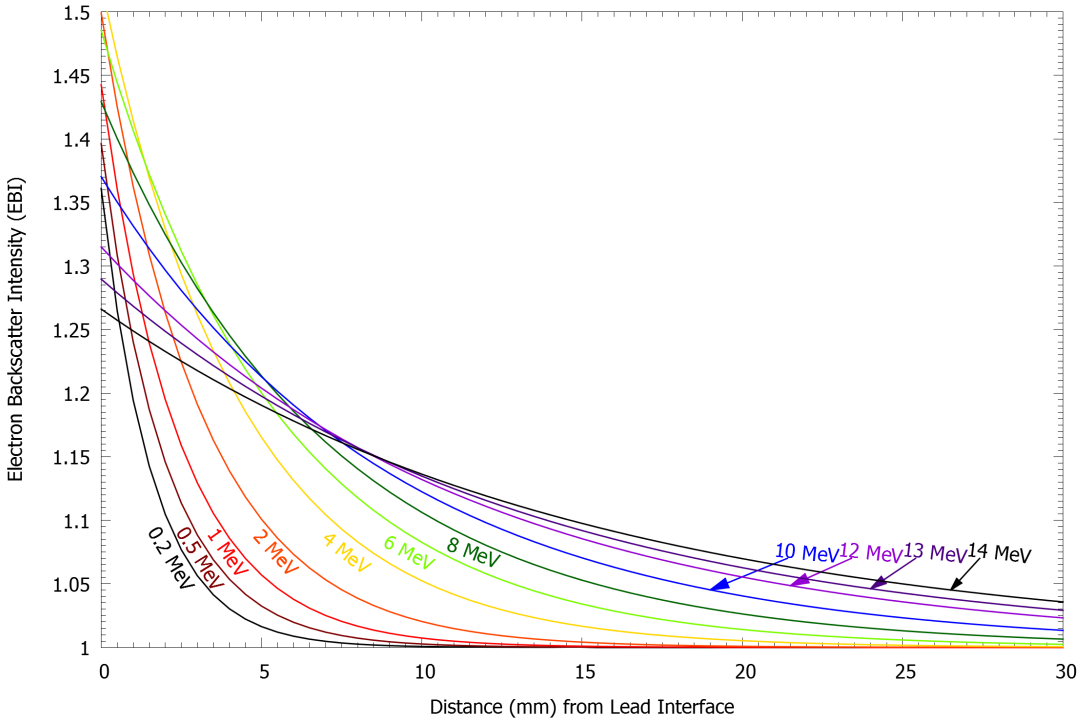

Figure 7.2: Graph of upstream Electron Backscatter (EB) verses the distance from a lead interface in mm predicted by Equation 7.1, derived from BEAMnrc MC simulations. Note: the energies displayed represent the energy at the lead interface, not the nominal energy of the electron beam.

In summary, this thesis has presented the results from a Monte Carlo investigation into dose enhancement caused by backscattered electrons from lead interfaces. The results have made it clear that the treatment planning system's algorithm, XiO's eMC, should not be relied on to predict dose around internal lead shielding. In addition, the currently used equation for estimating the EBF value is only clinically accurate in certain energy regions. As a result of this work a new equation was derived that can be used to estimate both the EBF value and upstream EBI dose over all the electron beams available locally to a clinically acceptable level.

Acknowledgements

It is with great pleasure that I am here able to acknowledge the people who assisted me throughout this thesis. First and foremost I would like to extend my gratitude to Keith Croft and Iordan Kostourkov for their guidance and valuable comments on everything from project ideas to analysis techniques. In addition, many thanks go to Dr. Juergen Meyer, Prof. Peter Metcalfe, and John Turner for providing external feedback at a time when the Physics Department was in turmoil.

I would also like to thank Midcentral District Health Board for funding my attendance to the 2012 BEAMnrc MC course, which I was fortunate enough to attend. A special thanks goes to the course lecturers, Dr. Frédéric Tessier, Dr. Ernesto Mainegra-Hing, and Blake Walters of the National Research Council of Canada and Prof. Dave Rogers of the Carleton University Physics Department.

I am also thankful to Dr. Steven Marsh, Coordinator of Medical Physics at the University of Canterbury and Gordon Laing. Although a late entry into the proceedings, their efforts in providing feedback and proof reading in a timely matter during the composition stage of this thesis are sincerely appreciated.

Thank you to my parents, Jurjen and Anneke, and to the physicists at Palmerston North: Tim O'Brien, Tania Groudeva, and again Iordan Kostourkov and Keith Croft. Their assistance and support related or unrelated throughout this project, however small or large, is greatly appreciated. Finally, I would like to thank Lily for her given support in any possible way throughout the entire process.

Bibliography

[1] "Cancer: New registrations and deaths 2009," tech. rep., Ministry of Health, 2012.

[2] B. K. Armstrong and A. Kricker, "How much melanoma is caused by sun exposure?," *Melanoma Res*, vol. 3, no. 395-401, 1993.

[3] G. B. Singh, M. Tiwari, H. S. Shukla, and M. Pandel, "Nd:YAG laser therapy of carcinoma lip (stage 1 squamous cell carcinoma): a retrospective evaluation," *Indian Journal of Otolaryngology and Head & Neck Surgery*, vol. 61, pp. 179–184, September 2009.

[4] E. Rio, E. Bardet, A. Mervoyer, B. Piot, B. Dreno, and O. Malrad, "Interstitial brachytherapy for lower lip carcinoma: Global assessment in a retrospective study of 89 cases," *Journal of the sciences and specialties of the head and neck*, vol. 35, April 2013.

[5] C. Val, J. Gebski, and G. J. Morgan, "Squamous cell carcinoma of the lip: is there a role for adjuvant radiotherapy in improving local control following incomplete or inadequate excision?," *ANZ Journal of Surgery*, vol. 73, no. 8, pp. 621–625, 2003.

[6] F. M. Khan, *The physics of radiation therapy.* Lippincott Williams & Wilkins, 3rd edition ed., 2003.

[7] K. R. Hogstrom and P. R. Almond, "Review of electron beam therapy physics," *Phys. Med. Biol.*, vol. 51, pp. 455–489, 2009.

[8] E. B. Podgorsak, *Radiation Oncology Physics: a handbook for teachers and students.* IAEA, 2nd ed., 2010.

[9] E. J. Hall, *Radio-biology for the radiologist.* Lippincott Williams & Wilkins, sixth edition ed., 2006.

[10] P. Mayles, A. Nahum, and J. C. Rosenwald, *Handbook of radiotherapy physics: theory and practice.* Taylor & Francis Group, 2007.

[11] W. P. W. Mayles, R. Lake, A. McKenzie, E. M. Macaulay, H. M. Morgan, T. J. Jordan, and S. K. . Powley, "Physics aspects of quality control in radiotherapy," Tech. Rep. 81, The institute of physics and engineering in medicine, Tadcaster Road. York, 1999.

[12] J. Seco and F. Verhaegen, *Monte Carlo Techniques in Radiation Therapy.* CRC Press, 2013.

[13] V. W. Haung, J. Seuntjens, S. Devic, and F. Verhaegen, "Experimental determination of electron source parameters for accurate monte carlo calculation of large field electron therapy," *Physics in Medicine and Biology.*, vol. 50, pp. 779–786, 2005.

[14] J. C. L. Chow and G. N. Grigorov, "Monte Carlo simulation of backscatter from lead for clinical electron beams using EGSnrc," *Medical physics*, vol. 35, no. 4, pp. 1241–1251, 2008.

[15] K. Kanaya and S. Okayama, "Penetration and energy-loss theory of electrons in solid target," *Appl. Phy.*, vol. 5, pp. 43–59, October 1971.

[16] N. A. Baily, "Electron backscattering," *Med. Phys.*, vol. 7, no. 5, pp. 514–519, 1980.

[17] P. W. Bigelow, "Back scattered electrons," April 2012.

[18] F. Krumeich, *Properties of electrons, their interactions with matter and applications in electron microscopy.*

[19] S. C. Klevenhagen, G. Lambert, and A. Arbabi, "Backscattering in electron beam therapy for energies between 3 and 35 MeV," *Phys. Med. Biol.*, vol. 27, no. 3, pp. 363–373, 1982.

[20] M. J. Berger, J. S. Coursey, M. A. Zucker, and J. J. Chang, "Stopping power and range tables for electrons, positrons, and helium ions," 2005.

[21] J. E. Saunders and V. G. Peters, "Back-scatting from metals in superficial therapy with high energy electrons," *British Journal of Radiology*, vol. 47, 467-470 1974.

[22] W. F. Gagnon and J. H. Cundiff, "Dose enhancement from backscattered radiation at tissue-metal interfaces irradiated with high energy electrons," *British journal of radiology*, vol. 53, pp. 446–451, 1980.

[23] T. Tabata and R. Ito, "Simple calculation of the electron backscatter factor," *Medical physics*, vol. 19, no. 6, pp. 1423–1427, 1991.

[24] M. M. Chang and S. B. Jiang, "Monte carlo modeling of electron beams for medical accelerators," *Physics medicine and biology*, vol. 44, pp. 157–189, 2009.

[25] J. Pérez-Calatayud, F. Ballester, M. A. Serrano, J. L. Lluch, E. Casa, and V. Carmona, "Dosimetric characteristics of backscattered electrons in lead," *Physics medicine and biology*, vol. 45, pp. 1841–1849, 2000.

[26] G. D. Lambert and S. C. Klevenhagen, "Penetration of backscattered electron in polystyrene for energies between 1 and 25 MeV," *Physics Medicine and biology*, vol. 27, no. 5, pp. 721–725, 1982.

[27] F. M. Khan, K. P. Doppke, K. R. Hogstrom, G. J. Kutcher, S. C. P. Ravinder Nath, J. A. Purdy, M. Rozendeld, and B. L. Werner, "Clinical electron beam dosimetry," *Medical Physics*, vol. 18, no. 1, pp. 3239–3280, 1991.

[28] D. W. O. Rogers, B. A. Faddegon, G. X. Ding, C. M. Ma, J. We, and T. R. Mackie, "BEAM: A Monte Carlo code to simulate radiotherapy treatment units," *Med. Phys.*, vol. 22, no. 5, pp. 503–523, 1995.

[29] E. B. Podgorsak, *Radiation physics for medical physicists*. Springer, 2nd ed. ed., 2010.

[30] "Siemens Linac: Beam path, Dimensions and materials," Tech. Rep. version 1, Siemens AG healthcare, 2011.

[31] "Siemens Primus: Basic Functional Description," Tech. Rep. version 1, Siemens AG healthcare, 2003.

[32] "TRS398: Absorbed dose determination in external beam radiotherapy," Tech. Rep. 398, International Atomic Energy Agency, Vienna, 2000.

[33] P. Bjork, T. Knoos, and P. Nilsson, "Influence of initial electron beam characteristics on monte carlo calculated absorbed dose distributions for linear accelerator electron beams," *Physics in Medicine and Biology*, vol. 47, pp. 4019–4041, 2002.

[34] D. W. O. Rogers, "Fifty years of monte carlo simulations for medical physics," *Phys. Med. Biol.*, vol. 51, pp. 287–301, 2006.

[35] M. H, Kalos, and P. A. Whitlock, *Monte Carlo Methods*. WILEY-VCH Verlag GmbH & Co. KGaA, 2004.

[36] J. F, *Monte Carlo theory and practice*. Data Handling Division, CERN, Geneva Switzerland: Cern, 1980.

[37] I. Kawrakow, E. Mainegra-Hing, D. W. O. Rogers, R. Tessier, and B. R. B. Walters, *The EGSnrc Code System: Monte Carlo Simulation of Electron and Photon Transport*. Ionizing Radiation Standards, National Research Council of Canada, 2011.

[38] D. K. Griffiths, *Introduction to elementary particles*. Weinheim:Wiley-VCH, 2 ed., 2008.

[39] P. Andreo, "Monte carlo techniques in medical radiation physics," *Phys. Med. Biol*, vol. 36, 1991.

[40] D. W. O. Rogers, B. Walters, and I. Kawrakow, *BEAMnrc User Manual*. Ionizing Radiation Standards, National Council of Canada, Ottawa, K1A Or6, 2011. http://www.irs.inms.nrc.ca/inms/irs/BEAM/beamhome.html.

[41] CMS software: The ELEKTA group, Stockholm, Sweden, *XiO training guide: Electron Monte Carlo algorithm*.

[42] D. W. O. Rogers, I. Kawrakow, and B. Walters, *DOSXYZnrc Users Manual*. Ionizing Radiation Standards, National Research Council of Canada, 2011.

[43] J. V. Dyke, R. B. Barnett, J. E. Cygler, and P. C. Shragge, "Commissioning and quality assurance of treatment planning computers," *International journal of radiation oncology biology physics*, vol. 26, no. 2, pp. 261–273, 1993.

[44] M. R. Bieda, J. A. Antolak, and K. R. Hogstrom, "The effect of scattering foil parameters on electron-beam monte carlo calculations," *Medical Physics*, vol. 28, no. 12, p. 2527, 2001.

[45] B. A. Faddegon, J. Perl, and M. Asai, "Monte carlo simulation of large electron fields," *Physics in Medicine and Biology*, vol. 53, pp. 1497–1510, 2008.

[46] P. Shokrani, M. Baradaran-Ghahfarokhi, and M. K. Zadeh, "A novel approach in electron beam radiation therapy of lips carcinoma: A monte carlo study," *Medical Physics*, vol. 40, no. 4, 2013.

[47] M. Z. A. Aziz, M. S. Salikin, A. L. Yusoff, and R. Abdullah, "Monte Carlo simulation of electron beam in 3D phantom," *World academy of Science, Engineering and Technology*, vol. 60, 2011.

[48] C. Ma and D. Rogers, *BEAMDP Users Manual*. Ionizing Radiation Standards, National Research Council of Canada, Ottawa, K1A Or6, nrcc report pirs-0509(c)rev ed., 2011.

[49] R. Moylan, T. Aland, and T. Kairn, "Dosimetric accuracy of Gafchromic EBT2 and EBT3 film for in vivo dosimetry," *Australasian Physical and Engineering Sciences in Medicine*, 2013.

[50] B. J. Gerbi, J. A. Antolak, F. C. Deibel, D. S. Followill, M. G. Higgins, M. S. Huq, D. N. Mihailidis, and E. D. Yorke, "Recommendations for clinical electron beam dosimetry: supplement to the recommendation of task group 25," *Med. Phy.*, vol. 36, no. 7, pp. 3239–3279, 2009.

[51] K. R. Hogstrom, M. D. Mills, and P. R. Almond, "Electron beam dose calculations," *Physics in Medicine and Biology*, vol. 26, p. 445, 1981.

[52] K. R. Hogstrom and P. R. Almond, "Review of electron beam therapy physics," *Physics in Medicine and Biology*, vol. 51, pp. 455–489, 2006.